Growth and electrical properties of chemical vapour deposited low dimensional sp^2 carbons

YEE YUAN TAN

Submitted for the degree of

Doctor of Philosophy

From the

University of Surrey

Advanced Technology Institute

Faculty of Engineering and Physical Sciences

University of Surrey

Guildford, Surrey GU2 7XH, United Kingdom

2012

Abstract

This thesis describes the growth of sp^2 carbon materials – namely graphene and carbon nanotube (CNT) materials using a chemical vapour deposition (CVD) process. A novel CVD process tool based on a photothermal process (PT-CVD) that differs from standard thermal CVD has been developed. This thesis reports the investigations into the properties of the deposited carbon nanomaterials and applications that exploit their electronic properties.

The first investigation is into the growth of vertically aligned MWCNT forests. Growth of CNTs at 370°C by a one-step PT-CVD method was demonstrated. The growth rate can reach ~ 1.3 μm/min, which is faster than most other reported thermal CVD methods. The use of bimetallic catalyst (Fe/Ti) and the use of rapid thermal process are the keys to this process. AFM topography studies showed that the fast top-down heating mode of the PT-CVD leads to the formation of a Fe/Ti uniform solid solution, which is believed to improve the CNT growth. These CNTs are composed of a few layer crystalline graphene sheets with a 5–6 nm diameter. Raman scattering provides supporting evidence that the as-grown CNTs are of high quality, better than some CNTs grown at higher temperatures by traditional CVD methods.

CVD growth of graphene was investigated using Cu foils as substrate, with the field-effect in the graphene subsequently demonstrated by transferring it to a back-gate bottom contact transistor arrangement using poly-4-vinyl-phenol gate dielectric as an alternative to oxide based insulators. This graphene transistor showed a simple, inexpensive fabrication method that is completely compatible to large scale fabrication

of organic devices, to demonstrate a field effect hole mobility of 37 cm^2/ Vs. Despite the mobility being lower than that found in exfoliated graphene, it demonstrates the potential of a graphene based all carbon transistor for large area electronics.

The fabrication and electrical performance of a 3 terminal graphene device is further reported. This device displayed characteristics similar to a p-type graphene FET. While past investigations of distortion and saturation in transfer characteristics of graphene FET indicated that metal-graphene interaction may be the controlling mechanism, this device operation is based on the design of transferring graphene onto a Diamond-like-carbon DLC/p-Si heterostructure with Si as the back contact and with the DLC acting as the dielectric support in contact to graphene. Thus, this provided a mechanism for the DLC/p-Si heterojunction to moderate the *I-V* characteristics of this device, resulting in a p-type only conduction process in graphene that is also saturable.

Following the work on using conventional thermal CVD (T-CVD) for graphene growth, we demonstrated the possibility of using the PT-CVD to develop a graphene growth process. It is found that the non-thermal equilibrium nature of PT-CVD process resulted in a much shorter duration in both heating up and cooling down, thus allows the reduction of the overall growth time for graphene. The choice of performing growth on Ni also allows for the alleviation of hydrogen blister damage that is commonly encountered during growth on Cu substrates. To characterize the film's electrical and optical properties, pristine PT-CVD grown graphene was used as the transparent electrode material in an organic photovoltaic devices (OPV) and is found to be comparable to that reported using pristine graphene prepared by conventional CVD.

Declaration

This thesis is submitted for the degree of Doctor of Philosophy at the University of Surrey. No part of this thesis has been or is currently being submitted for any other degrees, diploma or other qualifications.

YEE YUAN TAN

Jan 2012

Acknowledgements

I would like to express my sincere appreciation for my advisors: Prof. R. Silva, Drs J.D. Carey and J.V. Anguita for their support and guidance throughout my graduate study. I am also indebted to Dr N.G. Shang for his patience, kind advice and guidance in my studies and beyond.

I would also like to acknowledge, Drs D. Adikaari, W. Zhang, S. Henley, V. Stolojan, C. Giusca, D. Cox, G.Y. Chen and Prof. J. Shannon who have had at various points in my time in ATI, had one way or another contributed to my PhD studies.

I thank my friend and fellow student K. Jayawardena for so kindly sharing his time and effort with me in our time in ATI.

I would also like to thank the guys in NEC group and ATI at large for giving their time, space, advice and at times – equipments, throughout my stay in ATI.

To all the ATI staffs for their help and support through my studies, for which without things would not work at all.

Lastly, I would like to thank my families, and to Li Wei for all their unconditional love and for putting up with me all these while.

Publications

Journals

Y. Y. Tan, K. D. G. I. Jayawardena, A.A..D.T. Adikaari, L. W. Tan, J.V. Anguita, S. J. Henley, V. Stolojan, J. D. Carey and S. R. P. Silva, Photo-thermal chemical vapour deposition of graphene, *Carbon,* 50, (2012), 668-673 .

Y. Y. Tan, L. W. Tan, K. G. Jayawardena, J.V. Anguita, J. D. Carey and S. R. P. Silva Field effect in chemical vapour deposited graphene incorporating a polymeric gate dielectric, *Synthetic Metals*, 161, (2011), 2249-2252.

N. G. Shang, Y. Y. Tan, V. Stolojan, P. Papakonstantinou and S. R. P. Silva, High-rate low-temperature growth of vertically aligned carbon nanotubes, *Nanotechnology*, 21 (2010), 505604.

K. D. G. I. Jayawardena, Y. Y. Tan, J. Fryar, H. Shiozawa, S. R. P. Silva, S. J. Henley, G. M. Fuge, B. S. Truscott, M. N. R. Ashfold, Highly conductive nanoclustered carbon-nickel films grown by pulsed laser deposition, *Carbon*, 49, 12, (2011), 3781-3788

W. Zhang , Y. Y. Tan, C. Wu and S. R. P. Silva, Self-assembly of single walled carbon nanotubes onto cotton yarn: Towards the production of conductive yarn and ammonia sensor, *Particuology*, in press.

K. D. G. I. Jayawardena*, Y. Y. Tan*, J.V. Anguita, L. W. Tan and S. R. P. Silva, A p-type unipolar transport in graphene device via DLC/Si heterojunction effect, *submitted to Applied Physics Letter.*

M. S. Saavedra, G. D. Sims, L. N. McCartney, V. Stolojan, J. V. Anguita, Y. Y. Tan, S. L. Ogin, P. A. Smith and S.R.P. Silva, Catalysing Multiple Arm Carbon Octopi Nano-Structures, *Carbon,* in press.

Conferences

Y. Y. Tan, L. W. Tan, K. G. Jayawardena, J.V. Anguita, J. D. Carey and S. R. P. Silva, Raman spectroscopy on of graphene, *MRS 2010 spring*, San Francisco, USA, April 2010.

Y. Y. Tan, K. D. G. I Jayawardena, J.V. Anguita, and S. R. P. Silva, Growth of graphene using photo-thermal chemical vapour deposition, *Carbon 2011*, Shanghai, China, July 24-29, 2011.

Contents

CHAPTER 1

Introduction

Carbon, the sixth element in the periodic table, is found in a wide variety of materials, ranging from biological DNA to diamonds. In recent times, carbon allotropes – i.e. structures that consist only of carbon atoms, have been the subject of many scientific investigations. Among these carbon allotropes, two that have been intensely researched over the past few years are – carbon nanotubes (CNTs) and graphene/graphite. The trend in numbers of published papers on this subject has seen a phenomenal rise over the past decade (as shown in Figure 1.1).

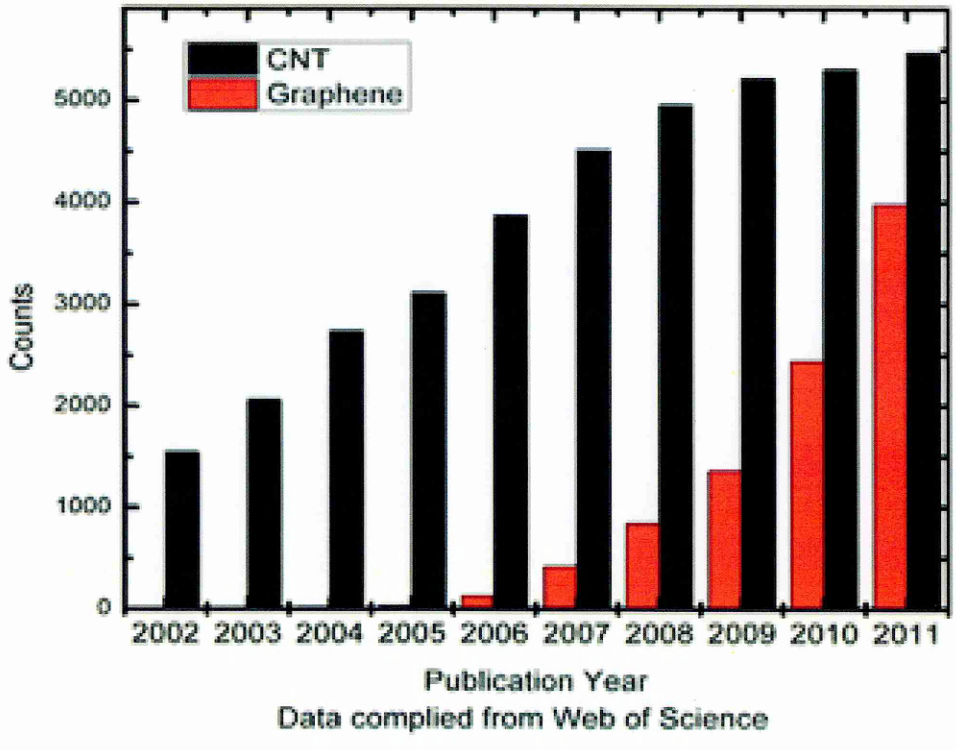

***Figure 1.1**: Trend of published literature related to CNT and graphene. Data assembled from Thomson Reuter's web of science.*

One of the appeals of sp^2 carbon in terms of an electronic material has been the high charge mobility (in the thousands of cm^2/Vs [1-2]), making it an attractive next

generation material beyond the present material of choice – silicon. Beside the potential of sp^2 carbon based transistors, sp^2 carbon allotropes also exhibit other attractive material properties. For example CNT has also been identified as a potential candidate for next generation electrical interconnects replacing copper under the ITRS roadmap [3]. Graphene is also another potential candidate for transparent conductors replacing Indium-tin-oxide (ITO) due to its high optical transparency [4]. In the area of optoelectronics, graphene has been investigated as an optical saturable absorbers [4]. Moving away from electronic applications, CNT has also been used for mixing into plastic under injection moulding process to mechanically strengthen the plastics [5]. The large surface area of these materials also makes it an ideal subject for hydrogen storage studies in the area of fuel cell research [6].

Given the large amount of interest in sp^2 carbon allotropes, this work is mainly focused on the growth of these carbon nano-materials and their electronic applications. The focus of this work is separated into CNT and graphene. Looking at the research into CNT interconnects, there are two important parameters to achieve – first is to have a CMOS compatible temperature process, and second - to have a fast turnaround or fast growth time. Currently, CNTs with electronic properties suitable for interconnects are demonstrated above the temperature of 600°C. However, this is still above the desired limit for industrial packaging, a back-end integrated circuit process of 400°C or lower. Thus the aim of this study is to achieve these two parameters in the CNT growth process using a rapid thermal process design.

In the area of graphene, as seen from Figure 1.1, compared to the more established CNTs studies, investigations into graphene is a more recent phenomenon. While much has been achieved in this short period of time and recognized in way of the Nobel prize awarded in 2010, there are still several barriers to overcome in order to introduce graphene to more industrial applications. One such potential area is in the field of organic electronics for large area device applications. Currently, most of the

demonstrations of graphene based field-effect transistor (GFET) are performed on very short channel devices as the graphene channel material is obtained through mechanical exfoliation technique on (kish) graphite – a low yield process that produces graphene of size in the order of a few micron wide. The use of a CVD based graphene growth process can overcome this shortcoming. The current reported studies in literature usually use standard thermal CVD processes. These processes tend to have a long processing turnaround time, thus limiting the through-put of graphene production.

There are two primary objectives in the studies reported here. The first aim is to investigate the performance of long channel GFET devices for large area electronics. One major advantage of a large channel GFET is the avoidance of the more expensive, complicated processes based on e-beam lithography. Investigations into the impact of different dielectrics on the performance of long channel GFETs are also explored. The second aim of this graphene study is to explore the possibility of achieving CVD growth of graphene with very short processing time yet still having comparable performance with graphene obtained with standard thermal CVD processes. Again the use of a rapid thermal process design is explored. Furthermore, given the good conductivity and optical transparency of graphene, the graphene produced via this rapid thermal process is explored by applying it to the area of organic photovoltaic devices – an area that has attracted much attention given the interest in green energy production.

This thesis is organized in the following manner. Chapter 2 is devoted to a review on the CNT and graphene in terms of its structure, properties, and preparation/growth methods. Chapter 3, a review on the photothermal CVD (PT-CVD) growth tool and the various experimental techniques are discussed, especially on the theory and usage of Raman spectroscopy for identifying sp^2 carbon nanomaterials. Chapter 4 will present the work on low temperature, fast rate growth of CNT using PT-CVD. The work on using conventional thermal CVD for growth of graphene and its application in FET devices is discussed in Chapter 5 and extended to Chapter 6 where a graphene FET

device structure using diamond like carbon (DLC) gate dielectric is discussed. This device's electrical behaviour is similar to a standard graphene FET but the underlying operating principle for this device is very different. In Chapter 7, PT-CVD is used for graphene growth and compared to conventional thermal CVD. The use of graphene as a transparent conductor for organic solar cell (OPV) is also discussed in this chapter. Finally the conclusion summarizing the work done so far is presented and future works is discussed.

CHAPTER 2

Review on Carbon Nanotube and Graphene

In this chapter, a literature review is presented on the various properties of carbon nanotubes (CNTs) and graphene. Furthermore, we also review the different techniques for growth and preparation of these carbon nanomaterials as reported in literature over the years. The synthesis techniques and conditions of nano-carbons dictates the macroscopic properties of the material and subsequently use in potential applications.

2.1 General overview of different carbon structures and properties

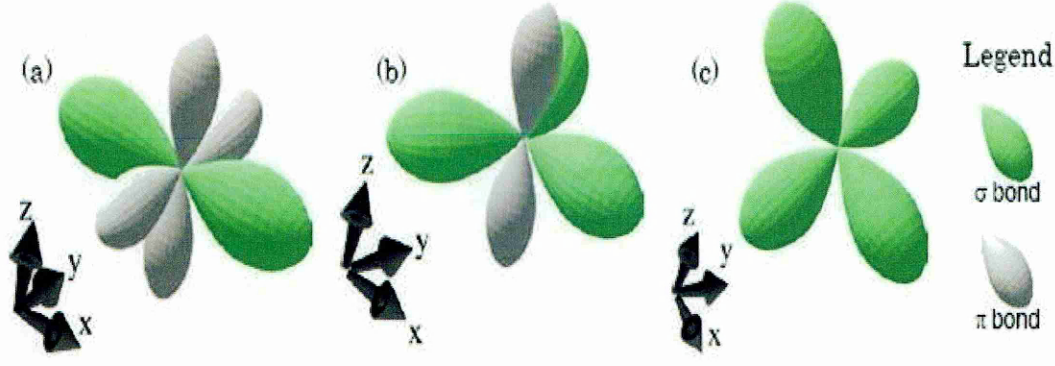

***Figure 2.1**: Schematic of (a) sp^1, (b) sp^2 and (c) sp^3 hybrid orbital. The sp^1 orbital has two σ bonds and two π bonds. The sp^2 orbital has three σ bonds and single π bonds. The sp^3 orbital has four σ bonds* [7].

Carbon can exist in many forms, with different chemical and physical properties. Individual carbon atoms have in total six electrons. In its ground state, the electrons occupy the $1s^2$, $2s^2$, and $2p^2$ orbitals, thus allowing for sharing of two 2p electrons for covalent bond formation. However, due to the small energy difference between the 2s and 2p orbitals, it is energetically favourable to mix the energy levels of the 2s and 2p orbitals to form hybrid orbitals, and thus increase the number of electrons available for bond formation. Depending on the energetics involved in the local environment of the carbon atom, a number of possible hybridisation can occur. Most commonly, these are

the sp^1, sp^2 and sp^3 hybridisations. These result in linear, trigonal-planar and tetrahedral bond configuration respectively (Figure 2.1).

***Table 2-1**: Parameters of carbon materials in different hybridisation states and with different dimensions [8].*

Dimension	*0-D*	*1-D*	*2-D*	*3-D*
	C_{60}	*CNT*	*Graphite*	*Diamond*
Hybridization	*sp^2*	*Sp^2*	*Sp^2*	*Sp^3*
Density(g/cm^3)	*1.72*	*1.2-2*	*2.26*	*3.515*
Bond length	*1.4*	*1.44*	*1.42*	*1.54*
Electronic properties	*Semiconductor, bandgap ~ 1.9eV*	*Metal or semiconductor*	*Semi-metal*	*Insulator, bandgap ~5.47eV*

Table 2.1, compiled by Saito *et al.* [8], shows some of the physical parameters for these materials composed of carbon isomers in different hybridisation states, and also, with different dimensions. Figure 2.2 shows the four respective structures of these carbon allotropes.

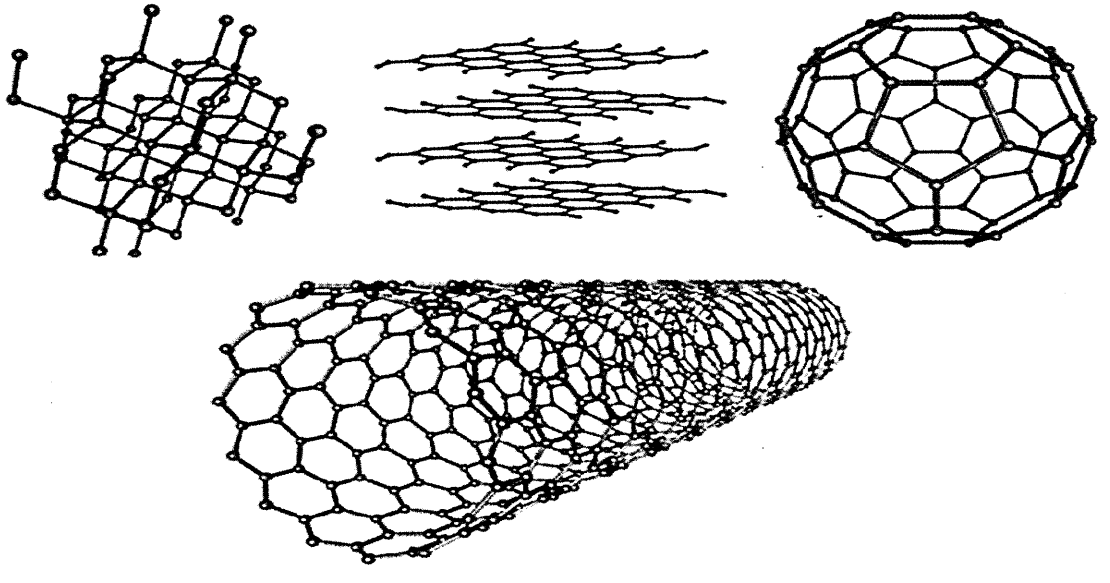

***Figure 2.2**: Schematics of (top-left) diamond, (top-centre) graphite or multi-layer graphene and (top-right) C_{60} respectively, The bottom shows a single wall CNT schematic [9].*

Diamond (3-D carbon formation) was first mined in India over 4000 years ago, but the modern diamond era only began in 1866, when huge diamond deposits were discovered in Kimberley, South Africa, creating a rush among European prospectors [10]. Table 2.2 shows diamond's physical properties.

***Table 2.2**: Some of the outstanding properties of diamond [10]*

extreme mechanical hardness (ca. 90 GPa) and wear resistance
highest bulk modulus (1.2×10^{12} Nm^{-2})
room temperature thermal conductivity ($2 \times 10^{3} Wm^{-1}K^{-1}$)
thermal expansion coefficient at room temperature very low ($1x\ 10^{-6}K$)
Broad optical transparency from the deep ultraviolet to the far infrared
highest sound propagation velocity (17.5 kms^{-1})
very good electrical insulator (room temperature resistivity is ca. 10^{13} Ω cm)
Diamond can be doped, becoming a semiconductor with a wide bad gap of 5.1 eV
very resistant to chemical corrosion

Graphite (2-D carbon formation) is also another well-known form of pure carbon. It is built from hexagonal planes of carbon atoms. In an ideal graphite, these planes are stacked on top of one another as shown below.

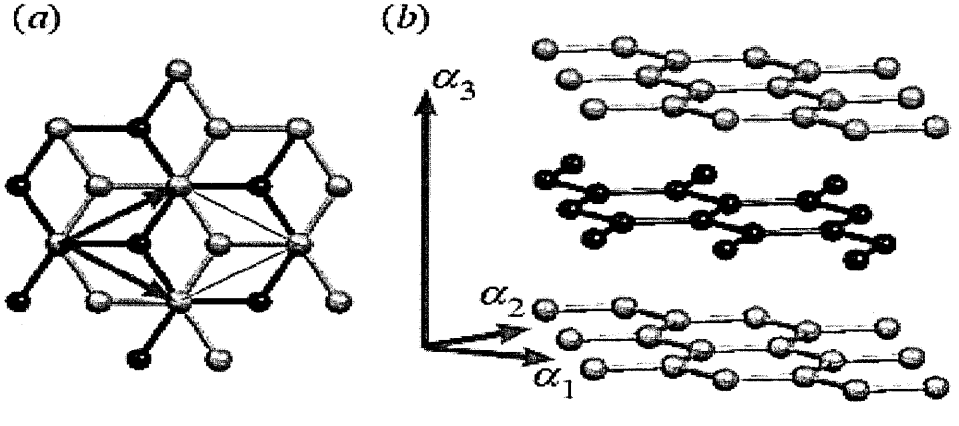

***Figure 2.3**: Graphite lattice in (a) top and (b) side view. α_1, α_2 and α_3 span the unit cell of graphite [11].*

At present it is believed that macroscopic single crystals of graphite most likely do not occur in nature. Highly oriented pyrolytic graphite (HOPG) is artificially grown graphite with an almost perfect alignment perpendicular to the carbon planes, along with the in-plane directions. HOPG can be regarded as consisting of multiple layers of graphene – a monolayer graphitic sheet.

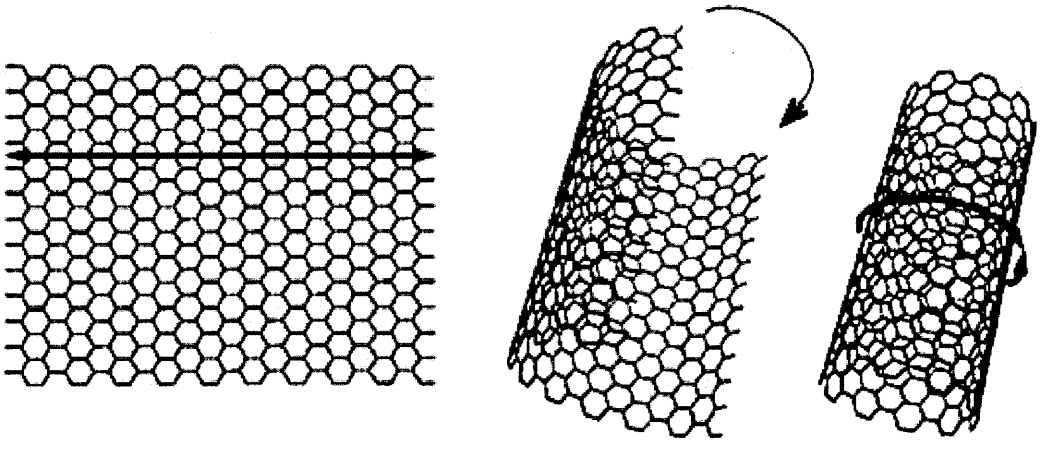

***Figure 2.4**: Rolling up of a graphene sheet into a SWCNT (from left to right) [12-13].*

If one graphene sheet is roll up as shown above, a single-walled carbon nanotube (SWCNT) is obtained. If more than one sheet is rolled together into a concentric roll, a multi-walled carbon nanotube (MWCNT) is formed. Depending on the chirality, SWCNTs can be metallic or semiconducting. Many electronics applications of SWCNTs, such as p-n junctions [14], molecular circuit interconnects [15], non-volatile memory elements [16], and single electron transistors (SETs) [17] have been reported in the literature.

2.2 Basic structure and atomic arrangement Carbon Nanotube

The electronic band structure of SWCNTs depend on the manner a graphene layer is rolled to form the nanotube. A chiral vector ($C=na_1+ma_2$) can be defined in terms of

unit vectors $\mathbf{a}_1$ and $\mathbf{a}_2$ of the graphene lattice helped to describe the different routes towards rolling graphene for obtaining CNT with different chiralities.

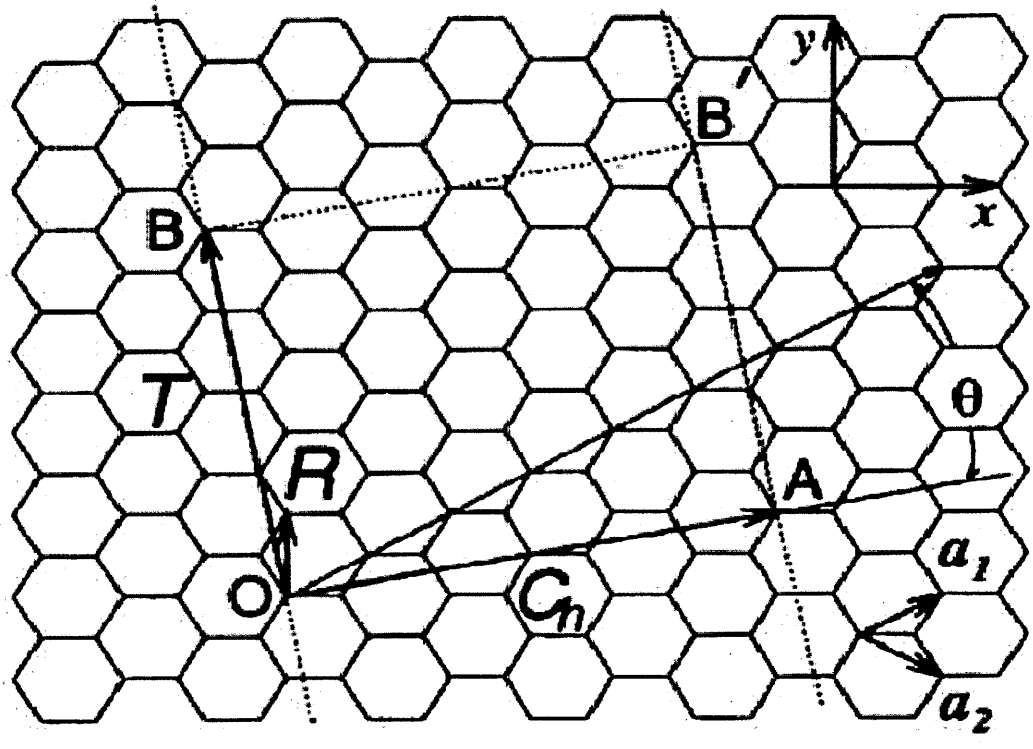

***Figure 2.5**: Relationship between a graphene sheet with SWCNT. Note the various definitions like chiral vector, nanotube axis T, symmetry vector R, and graphene unit cell vectors [8].*

Following the explanation presented in [8], imagine first that a virtual circumference which passes through a carbon atom is drawn. If the nanotube was cut perpendicular to this circumference through the middle of the atom and laid commensurate with a graphene sheet, the circumference would then appear as a vector, called the chiral vector C_h in Figure 2-5. The ends of the chiral vector must lie on atoms of the same graphene sub-lattice. This allows the chiral vector to be expressed in terms of the graphene primitive vectors as below:

$$\vec{C}_h = n\vec{a}_1 + m\vec{a}_2 \qquad [2.1]$$

where n is positive integer and $|m| \leq n$.

Figure 2-6 shows three types of SWCNTs: (a) armchair SWCNTs with indexes (*n*, *n*), (b) zigzag SWCNTs with indexes (*n*,0) and (c) chiral SWCNTs with indexes (*n*, *m*) other than the previous two specifically symmetric indexes.

Chirality (i.e. wrapping of the graphene) determines the electronic properties of the nanotube [18]. SWCNTs where (n, m) is divisible by 3, are metallic with zero bandgap. In all other cases, the SWCNTs are semiconducting, with a bandgap that depends on the diameter [19]

$$E_g = \frac{2\gamma_o a_{c-c}}{d_t} \qquad [2.2]$$

where γ_o is the C-C tight bonding overlap energy (~ 2.7 to 3eV), a_{c-c} is the nearest neighbour C-C distance (0.142 nm) and d_t is the diameter of the tube.

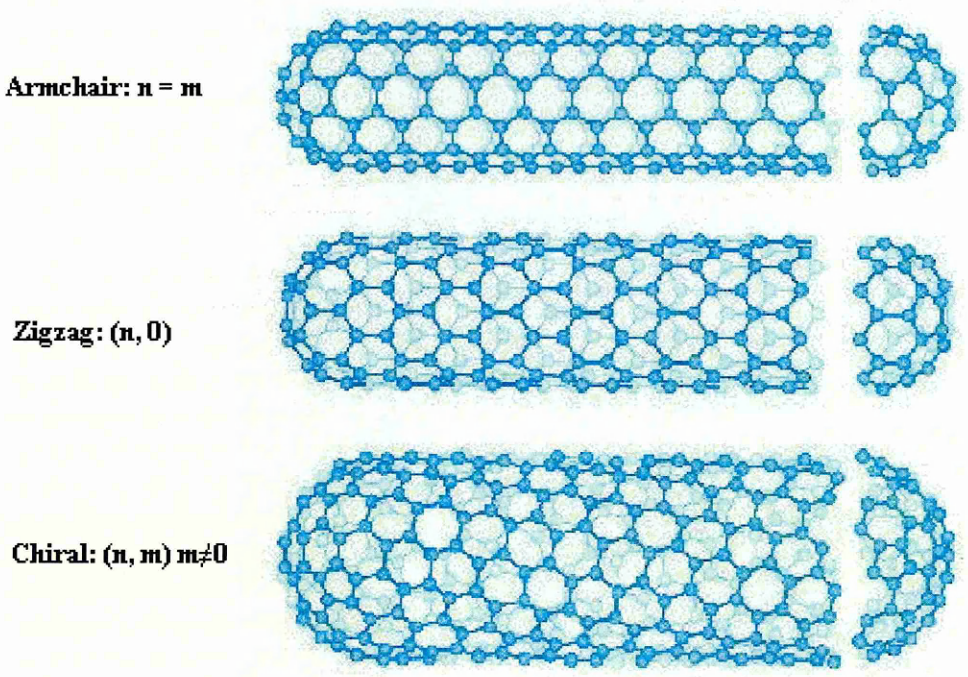

***Figure 2.6**: Chiralities of SWCNTs can be classified into three main groups - armchair (where n=m index), zigzag (which is semiconductor) and those that have non zero m index chirality (http://www6.ufrgs.br/lacer/gmn/nanotuboseng.htm)*

Multiwalled carbon nanotubes (MWCNTs) can exhibit a number of structural formations, for example, bamboo type, depending on the structures observed towards the ends of the tubes, as shown below (Figure 2.7).

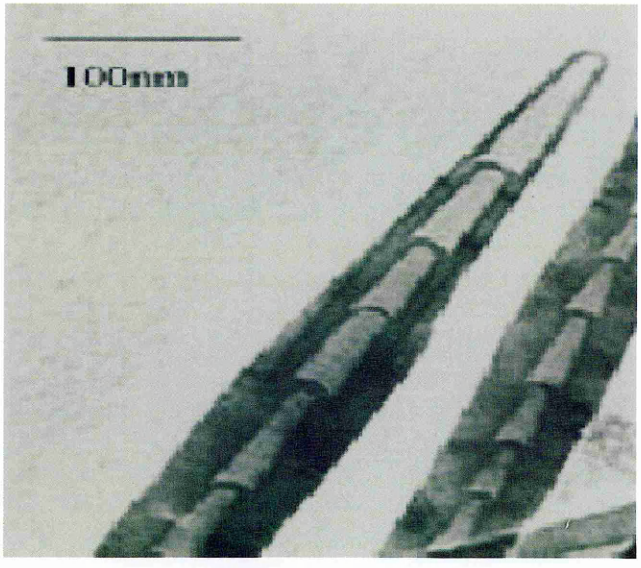

***Figure 2.7**: Transmission electron microscopy (TEM) image of a bamboo type MWCNT – seemingly like connecting tubes back to back [20].*

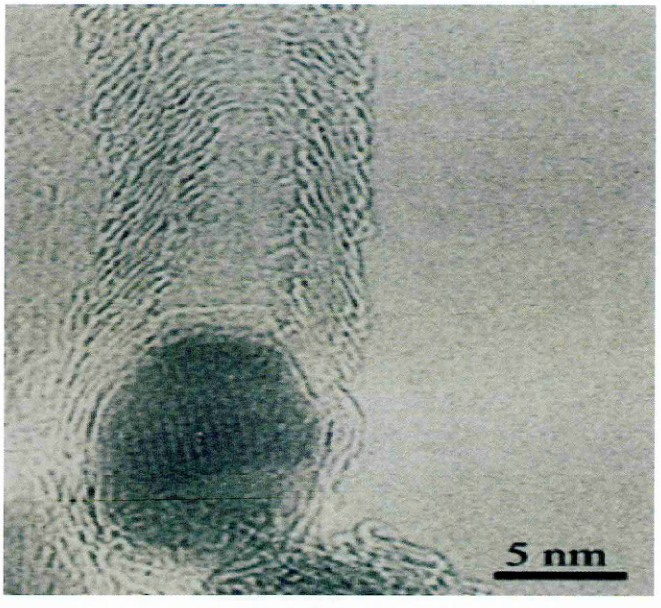

***Figure 2.8**: HRTEM image of the herringbone structure in CNFs with an ellipsoid catalyst located at its tip [21].*

Bamboo type MWCNTs are metallic in nature. This type of growth creates pockets within the nanotube that is similar to that of bamboo shoots. Another type of 1-D carbon nanostructures are carbon nanofibres (CNFs). These exhibit a 'herringbone' arrangement of the graphitic planes in Figure 2.8. In many cases, the literature does not distinguished CNTs from CNF's, and both types are referred to as MWCNTs [22].

2.3 Carbon Nanotube: Growth apparatus and preparations

At present, the more commonly used techniques for production of CNTs can be divided into three main classes:

- Laser ablation
- Arc-discharge
- Chemical Vapour Deposition - CVD

2.3.1 Arc discharge method

The carbon arc discharge method, initially used for producing C_{60} fullerenes [8], is one of the simplest methods to produce CNTs, as it comprises a relatively simple experimental setup. Iijima and co-workers [9] first reported an arc discharge method with a cathode containing metal catalysts (cobalt, iron or nickel) mixed with graphite powder, resulted in the deposits containing CNTs.

Seen in the following schematic of the arc-discharge system, CNTs are created through arc-vaporisation of a carbon rod placed end to end, and separated by approximately 1 mm, in an enclosure that is often filled with an inert gas at low pressure. The product of arc discharge requires further grinding and purification to separate the CNTs from the carbon soot and residual catalytic metals present in the product.

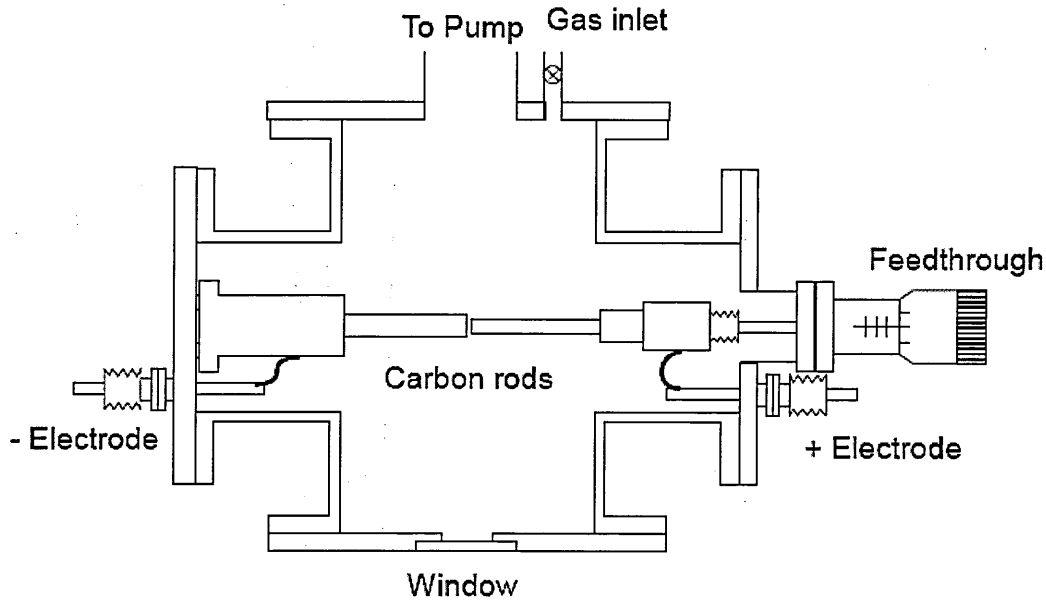

***Figure 2.9**: Schematic of the arc discharge system. The graphite rods are set facing each other. An arc is generated through them for CNT growth [8].*

2.3.2 Laser ablation

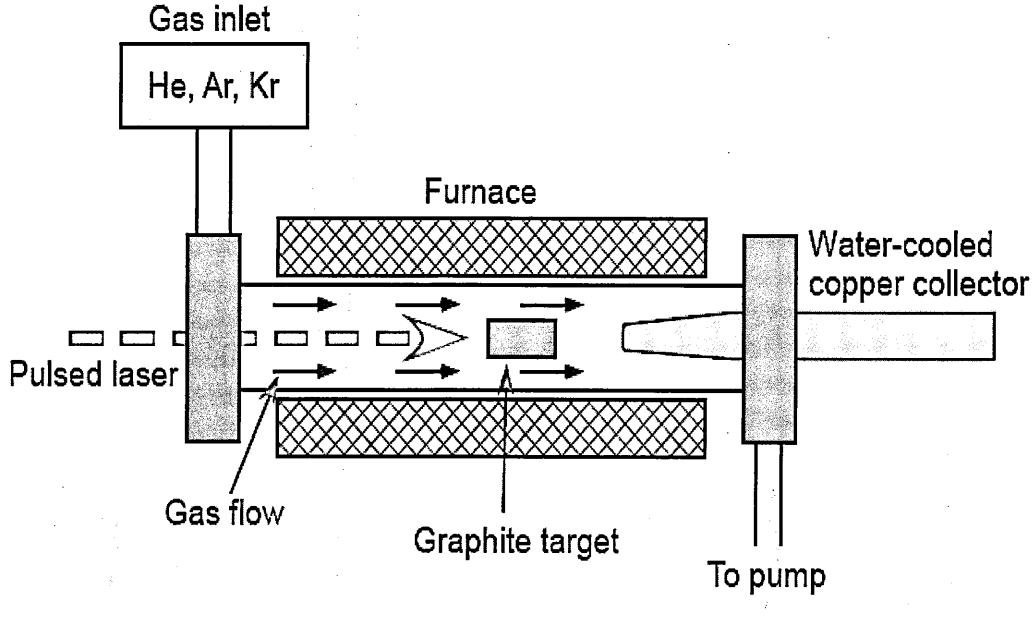

***Figure 2.10**: Schematic of a laser ablation set-up for CNT production. The laser incidents on the target (e.g. mixed composite of graphite and nickel/cobalt) and CNT is collected at the copper collector. The furnace is ~ 1200°C [7-8].*

Smalley et al. were among the earliest to demonstrate the growth of CNTs using laser ablation [23]. As shown in the schematic (Figure 2.10), CNT synthesis is typically carried out in a horizontal tube with a flow of inert gas at a controlled pressure. The flow tube is heated to high temperature, around 1200°C by a furnace. Laser pulses enter the tube and strike a target (inside the tube as shown), consisting of a mixture of graphite and a metal catalyst such as Co or Ni. As a result, CNTs condense from the laser plume and are deposited on a collector outside the furnace zone. Recently, Rummeli et al. [24] have demonstrated CNT growth in their investigations using a laser ablation experimental process with the furnace at room temperature instead of the high temperature as before.

2.3.3 Catalytic CVD methods

The catalytic CVD method is of special importance because the equipment is compatible with current semiconductor technology (albeit for the higher process temperature requirement), and it can be easily scaled-up for production [25]. This method offers a potential for integrating with current processes in the fields of electronics and optoelectronics as CVD processes are also commonly used in the industries for processes like thermal oxidation. Furthermore, CVD processes can allow large area growth on pre-patterned catalysts supported on substrates [26].

The synthesis of CNTs by CVD requires the presence of a carbon feedstock. Commonly used carbon gas sources include methane, acetylene and carbon monoxide, alcohol and even carbon clusters like C_{60} in the vapour phase. In an example of a reported thermal CNT (T-CVD) growth [27], Fe_2O_3 catalyst was prepared by impregnating fumed alumina nanoparticles with a methanol solution containing $Fe(NO_3)_3.9H_2O$. After impregnation, the methanol solution was removed and the material heated at 150°C and a resulting Fe_2O_3/alumina catalyst was obtained. CH_4 fluxes were then passed through the quartz tube as the furnace was heated to 1000°C. A

schematic illustrating the idea of such a thermal CVD system is shown in Figure 2.11(top).

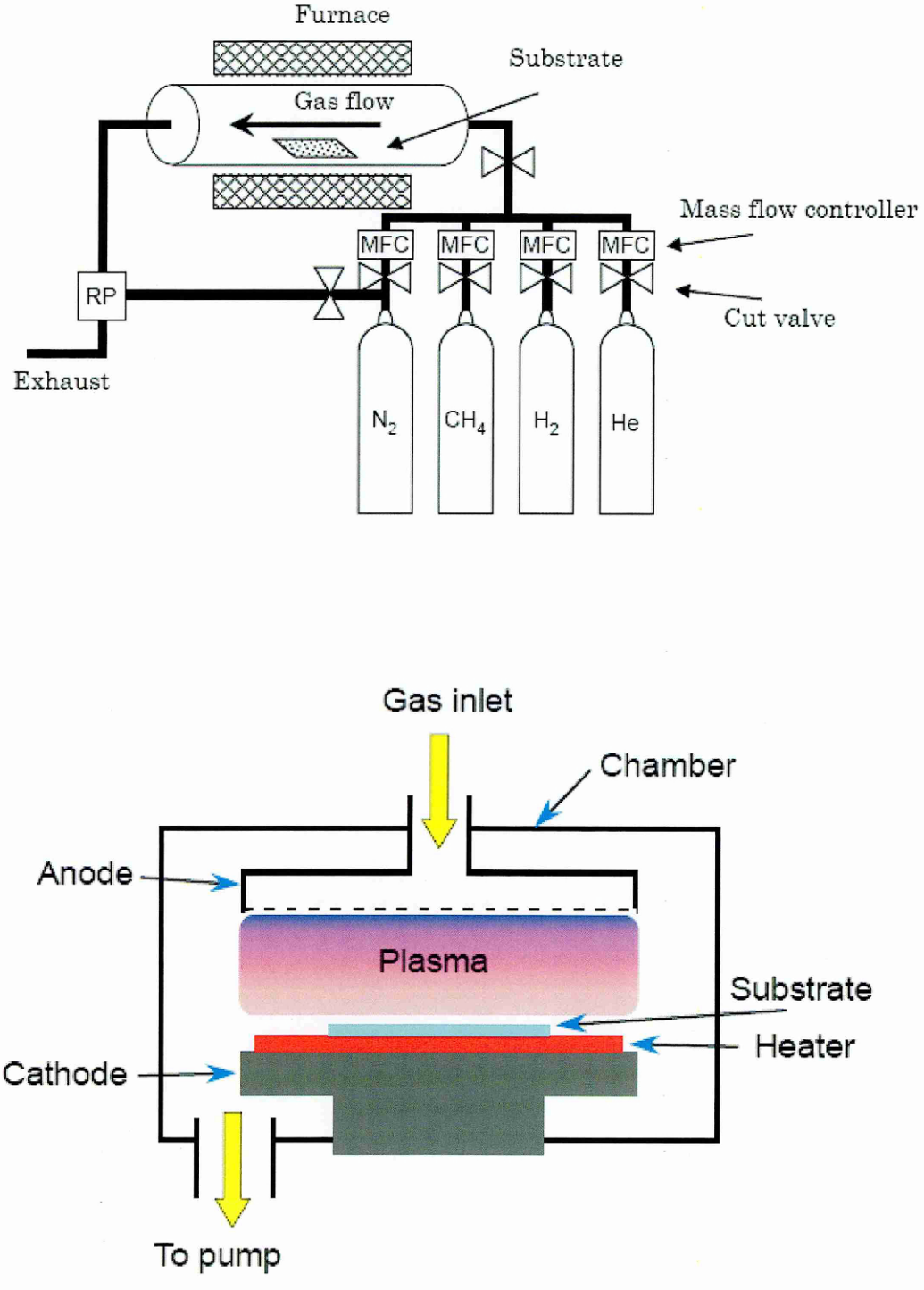

Figure 2.11: *(top) Schematic of a thermal CVD setup for CNT growth and (bottom) schematic of a plasma enhanced CVD [7].*

Besides using thermal energy in CVD, it is also possible for an additional plasma energy source (DC, RF or Microwave) to be introduced to create different conditions for the growth process design (shown in Figure 2.11(bottom)). This process is known as plasma-enhanced CVD (PECVD). It is important to note that despite the similarity shared by TCVD and PECVD, the chemistry between the two is quite distinct. In one reported finding, at 900°C, TCVD has only methane but a PECVD with 20% CH_4 in H_2, will contain higher stable hydrocarbons like acetylene and other radicals [28]. It has been proposed that lower (<500°C) temperature growth may be attributed to the presence of these species [25]. Furthermore, the application of plasma has also been demonstrated to be crucial in promoting either horizontally aligned [29] or CNT growth with bending angles dependent on the direction of the applied electric field [30].

A third configuration of the CVD process uses laser as the thermal energy source in-place (or complement in some cases) of the furnace. In typical applications, the laser is directed on the catalyst (which is pre-deposited on a substrate) with hydrocarbon gas passing over the surface to initiate the CVD process. The use of laser CVD (LCVD) is of potential technological importance, compared to the standard thermal CVD processes (T-CVD) because it has the potential to create patterns by selective exposure of substrates to this pin-point energy source in comparison to a standard thermal CVD which heats up the entire sample. Some laser sources reported in literature are continuous laser sources using Ar-Ion, CO_2 or Nd-YAG [31].

2.4 CNT Growth Model for CVD processes

In this thesis, we will concentrate on growth models that seek to explain the catalytic nature of the carbon filament growth process since the growth process investigated are generally CVD in nature. One such theory [32] described a model based on the interaction between catalyst and gaseous carbon resulting in CNT growth.

There are two types of growth models – tip growth model which is so named as the catalyst is on the tip of the CNT, and base growth model which is where the catalyst is at the base of the CNT as shown below. Base growth is also sometimes referred to as root or extrusion growth.

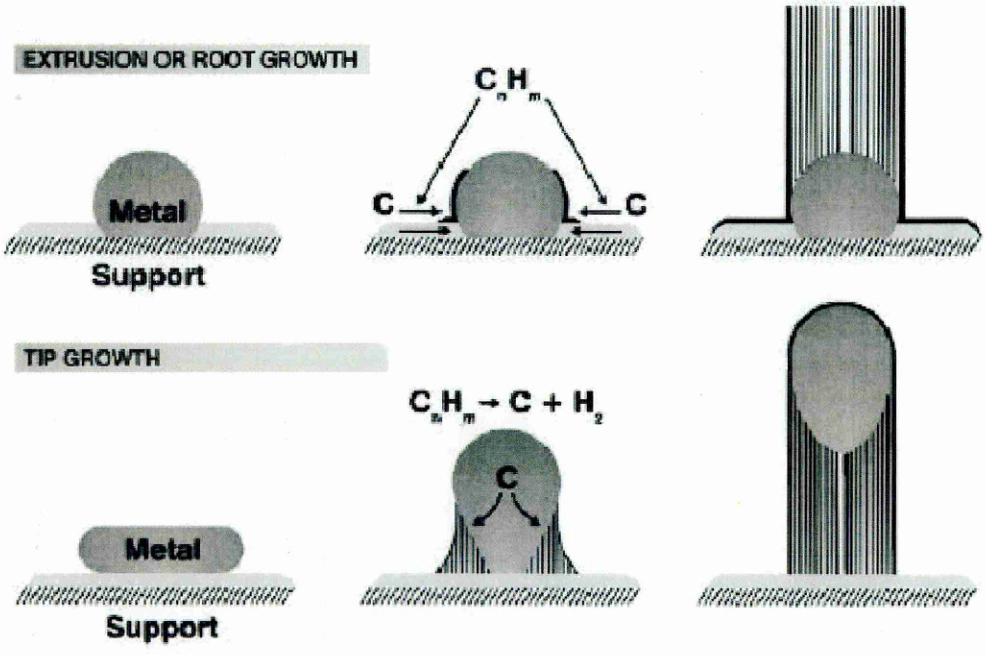

***Figure 2.12**: Illustrations of Base Growth (top) and Tip Growth (bottom) Mechanisms. Depending on the catalyst and its substrate interaction, one of the mechanisms would take place. In the top half of the panel, a layer is thought to form at the surface and lifted upwards to relief the built-up strain energy. For the bottom half of the panel, carbon species is thought to diffuse into the catalyst and lift the catalyst up [33].*

Using thermodynamic studies of CNT/CNF growth via catalytic CVD system, Baker and co-workers proposed that the following steps happen in carbon filament growth: (1) adsorption and decomposition of hydrocarbon feedstock over the surface of the catalyst with the main driving forces of growth thought to be temperature and concentration gradients. This leads to (2) dissolution and diffusion of carbon species through the catalysts, (3) precipitation of carbon on the opposite surface of the catalysts to finally form a nanofibre/nanotube like structure. Depending on the interactions between the catalyst and its substrate support, tip growth or base growth would occur.

The growth of carbon filament stops when the catalysts are covered by a carbon formation on the surface of the catalysts which prevents further decomposition of the carbon source.

Since then, there has been much experimental and theoretical work done on refining and quantifying the model. One area of investigation is the state of the catalyst and the behaviour of the carbon species during a CVD process. It is thought that the diffusion of the carbon species at the surface of the catalyst will depend on its phase. Bulk melting temperature of commonly used catalysts like Fe is ~ 1530°C, and Cobalt melts at ~ 1495°C while most reported CVD's operating temperature are within 1000°C, implying a solid phase.

However nanoparticle sized Fe, due to its large surface energy resulted from a high surface to volume ratio will affect its physical properties among other parameters, thus leading to the possibility that the Fe nanoparticle is in liquid phase. Based on this possibility, a vapour liquid solid mechanism (VLS) can take place in which the carbon species dissolved and diffuse through the particles to form CNT/CNF structures [34]. The rate limiting step in the growth is thought to be carbon diffusion through the catalyst. In the case of using Ni catalysts with C_2H_2, the activation energy is similar to that of bulk diffusion through the catalyst [32, 35].

Recent investigation into tip growth has shown new insights. Using a time resolved atomic resolution in-situ TEM (shown in Figure 2.13), Helveg and co-workers [36] studied methane decomposition over Ni on $MgAl_2O_4$. They found that as CNT forms, the Ni particle undergoes shape change, displaying a liquid like particle behaviour. Surface diffusion of carbon over the Ni preceded the CNT growth. Stolojan and co-workers [37] proposed that surface diffusion mechanism is the main driver of CNT growth under the CVD process. The creation of metal-carbide compound (Ni in this case for the paper) most likely will enhance this effect as carbon is prevented from

further diffusion into the catalyst. However the possibility of bulk diffusion phenomena is not excluded.

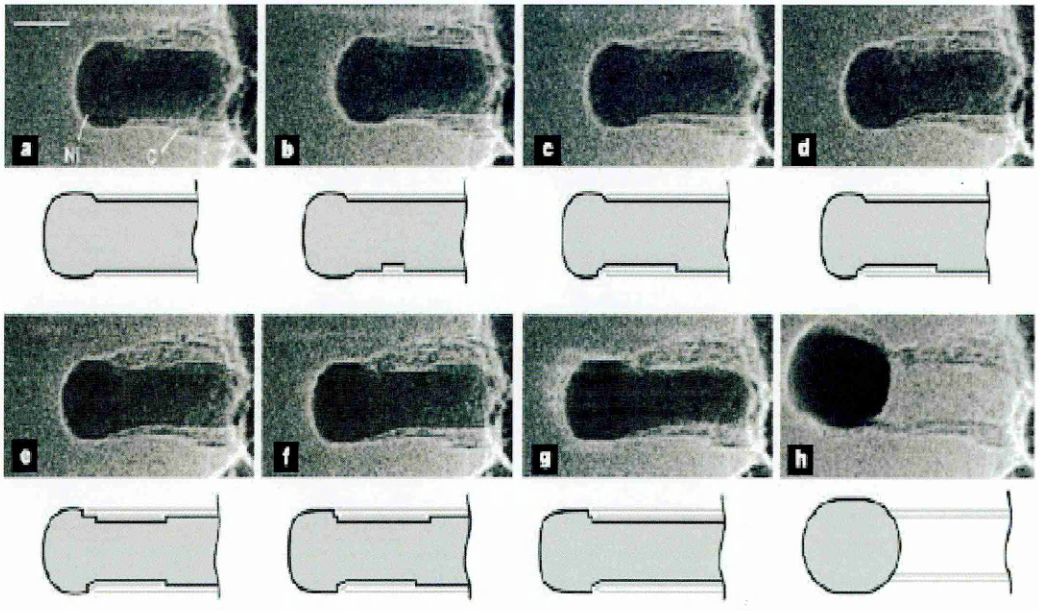

Figure 2.13: *TEM sequencing images of a carbon nanotube growing with surface diffusions. Growth of CNT was observed to have initiated at step edges of catalyst particles [36].*

For base growth model, the Yarmulke mechanism is proposed [38] in which growth is driven by surface energy. As carbon species deposit on the catalyst, graphene is formed on the surface with edges bonded to the catalyst. It is proposed that total surface energy is decreased as graphite's basal planes have low surface energy. The graphene is lifted upwards from the energy that is generated by relaxation of the strain energy built up in the graphene. Base growth process tended to be observed in SWCNT, and it is thought that with the catalysts stuck to the substrate, generally it would be more difficult to find these nano-particles in TEM imaging. Shown in Figure 2.14 is a collection of TEM images that showed various CNT samples that exhibited the base-growth phenomena [39].

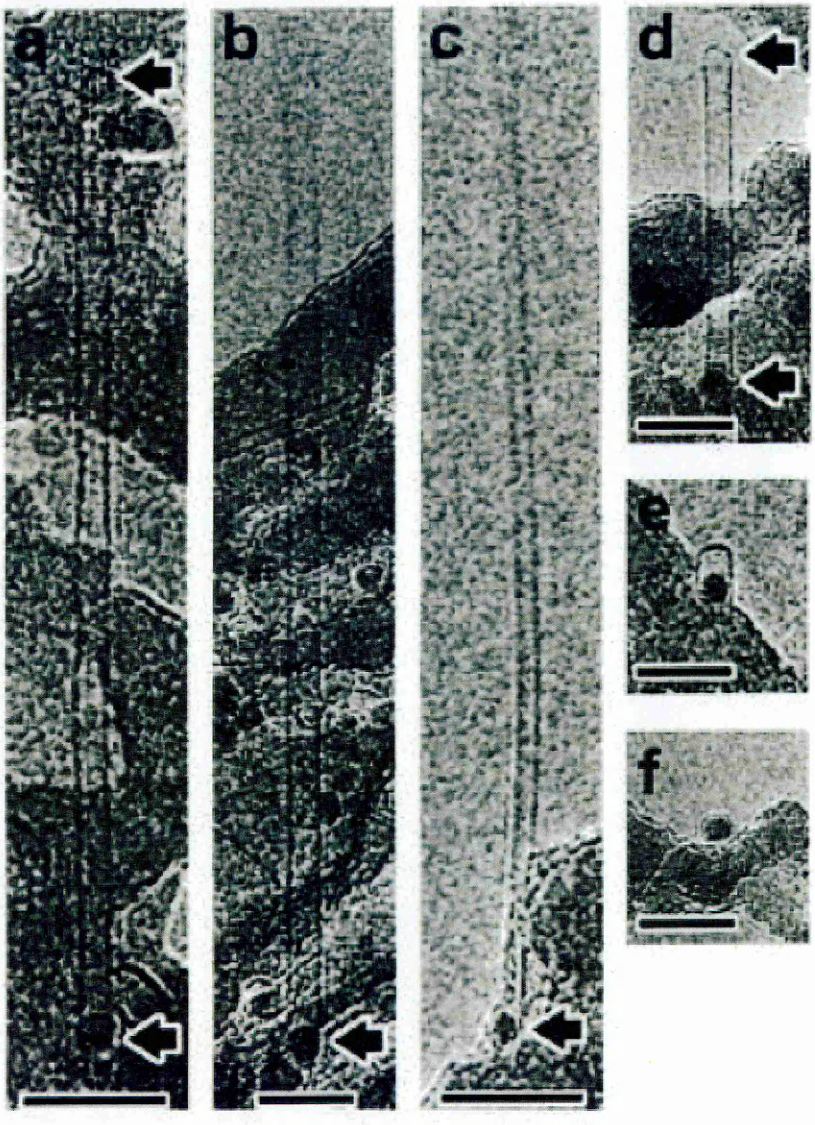

Figure 2.14: *Collections of TEM images (a to f) showing various CNT growths with the discrete nano-particles/catalysts (which were residing on a membrane) at the bottom of the carbon nanotubes. The bar scale is 10 nm [39].*

2.5 Catalyst preparation for CNT growth under CVD

Given the importance of catalysts' role in the growth of CNT under CVD, an exceedingly large variety of preparation methods have been reported in the literature. In this section, we segregated the various preparation methods into three main categories.

Regardless of the preparation methods used, the aim is to be able to control the resultant nanoparticles' size distribution as there is a correlation between size and CNT's diameter [38]. Also of importance is the chemical composition of the resultant nanoparticles after preparation. For example, a bimetallic alloy like Mo-Co seems to result more favourably towards SWCNT growth than they would be as individual catalysts [40].

2.5.1 Floating catalyst approach

In this method, a stream of catalyst particles is constantly injected into the gas mixture/feedstock. Metallocene is a very popular form of catalysts employed in this technique, two commonly used metallocenes are ferreocene and nicklocene [41].

2.5.2 Solution based catalyst approach

Spin-coating/drop-casting or immersion into a solution containing the necessary catalyst for CNT growth is also another popular method reported in literature. An example of such a procedure [42] is to submerge a 500nm SiO_2/Si wafer into a freshly mixed aqueous hydroxylamine and $FeCl_3$ – ($FeCl_3.6H_2O$ + $NH_2OH.HCl$ + double distilled water) leading to spontaneous deposition of Fe nanoparticles on the wafer.

2.5.3 Physical deposition approach

Metal can be deposited using evaporation or sputtering onto a substrate. The metal, deposited at room temperature, will generally be an amorphous and smooth film on the surface of the substrate. Upon thermal annealing, an 'equilibrium' shape may be reached. Based on surface energies, this 'equilibrium' shape can be classified into Volmer–Weber growth [43] for non-wetting (I) and wetting (II), and layer-growth (III).

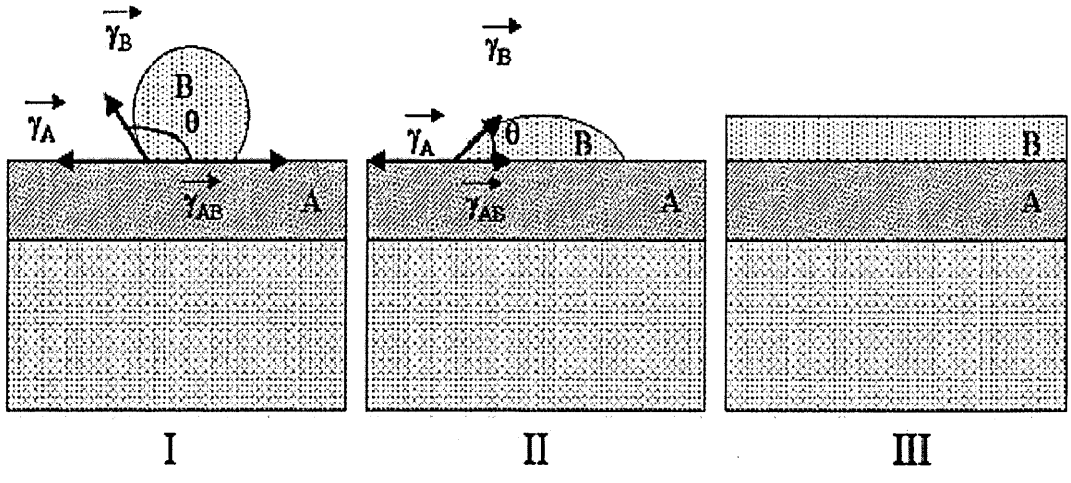

***Figure 2.15**: Volmer–Weber growth for non-wetting (I) and wetting (II), and layer-growth (III). Young's equation describes the contact shape: $\gamma_A = \gamma_{AB} + \gamma_B \cos\theta$ where γ is the corresponding interfacial energy. For CNT growth using CVD system, dewetting of catalyst is desired [43].*

Deposition of a thick catalyst film tends to result in large diameter particles. Higher temperatures and longer annealing times will also produce larger-size particles. One explanation is that the higher annealing temperature imparts higher energy to the particles. Therefore, these particles are allowed to move more aggressively to meet other particles and subsequently recombine to a larger size particle. Longer annealing time period results also produce similar output because it increases the chances for particles to meet each other as they can travel longer distances on the substrates during annealing. Thus by optimizing the thermal annealing time period and temperature, the size of the metallic catalysts can be controlled directly.

Besides the above considerations, interaction between the deposited metal catalysts and its supporting substrate can also affect the growth and yield of CNTs [40]. For example, Homma et al. observed the formation of iron silicide by annealing iron catalysts on silicon wafers in a methane atmosphere [44].

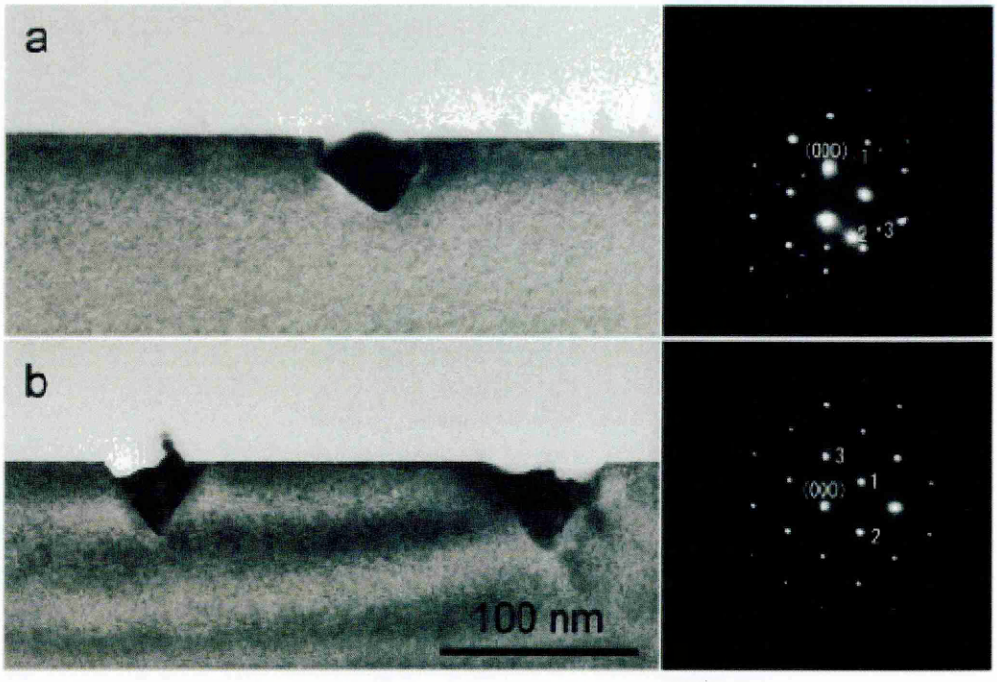

Figure 2.16: *TEM image of catalyst after annealed with methane with the corresponding silicide diffraction patterns. (a) shows Fe nanoparticles after annealing at 1000 ºC and (b) shows Co nanoparticles after annealing at 950° C [44].*

On a substrate such as silicon wafer, the use of an interlayer such as aluminum, aluminum oxide and silicon oxide can minimize such reactions between the catalyst metals and the silicon wafer [40]. Furthermore, the introduction of such an interlayer usually resulted in smaller catalyst particles size which can be attributed to chemical or physical interaction s between the catalyst and interlayer. Physical interactions - van der Waals electrostatic force and surface roughness help to reduce the thermally driven diffusion of metal particles on the support surface. Under chemical interactions, negative charges migrate into the metal catalyst from the substrate, which in turns enhances its catalytic activity by strengthening back donation of electron density into anti-bonding orbitals of the absorbate [45]. The result of this electron sharing between catalyst and absorbate will weaken the bonding within the absorbate and resulted in its dissociation. All these resulted in the catalyst particle size being stabilized during the growth process. In the work reported in this thesis, the preparation of the metal catalysts for CNT growth was performed using the physical deposition method.

2.6 Graphene – properties and structure

In this section, a literature review on the current status of graphene and its relationship to graphite is presented. As mentioned before, graphene is a hexagonal monolayer of carbon atoms which when rolled up will result in 1-D SWCNT. This monolayer sheet of carbon can also be wrapped into 0-D fullerenes. Theoretical studies of graphene dated as early as 50 years back [46-47]. The band structure of graphite exhibited linear *E-k* relation for low energies near the six corners of the 2-D hexagonal Brillouin zone[2, 46].

2.6.1 Charge transport in graphene and its electronic devices

The earliest demonstration of graphene based electronic device was a back-gate field effect (FET) transistor [48], and was subsequently widely used to investigate the electronic properties of graphene due to the relative ease of the fabrication [49-50]. The appeal of fabricating graphene into a FET structure is that it allows the charge transport properties to be determined via electrical measurements while subjected to various effects like electric or magnetic fields. Since then graphene FET has moved from the domain of condensed physics into electronic device community as it is seen to have the potential to replace silicon based FET [51]. The most conveniently fabricated FET structure uses Si as the back gate for gate voltage sweeping, SiO_2 as the gate dielectric, and with the graphene, obtained via the 'scrotch tape' technique, as the channel material.

One of the most widely investigated properties of graphene is its high charge transport mobility [52]. The conductivity of graphene was found to be carrier-density dependent, which implied it could be tuned via an electric field gating (i.e. applying a voltage to the gate) through the SiO_2 layer [48-49]. Subsequent reports showed that the choice of different dielectric layers as well as the choice of top or bottom gate FET configuration can also strongly influence the charge mobility of graphene [53-54]. A general feature

of the transport characteristic of graphene, shown in figure below, shows that the conductivity is in principle symmetrical, ambipolar and linear in carrier density [49]. At higher applied gate voltage, the conductivity is often found to be slightly sublinear in carrier density for high mobility samples [55].

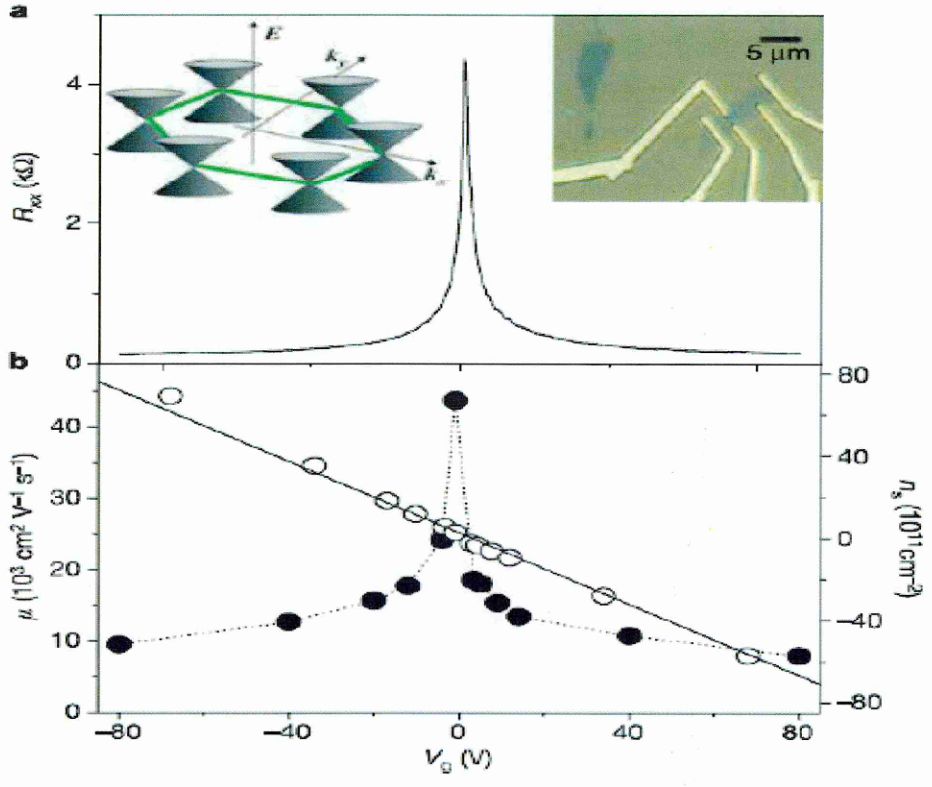

Figure 2.17: *Conductivity of graphene as shows above dependence on the applied back gate voltage. The FET device was fabricated on a heavily doped silicon substrate with a thin layer of silicon dioxide as the gate dielectric [50].*

One salient feature as observed from the above mentioned FET experiments indicated that at low carrier density, the conductivity of graphene does not go to zero at the transition between electron and hole conduction. Instead a range of minimum values were reported. In some of the published data, this minimum conductivity was reported to be very close, $\approx 4\frac{e^2}{h}$ [49, 56], which was deemed to be the universal value for massless Dirac fermions. Others reported a wider range of the distribution of the minimum conductivity [55] as seen in Figure 2.18.

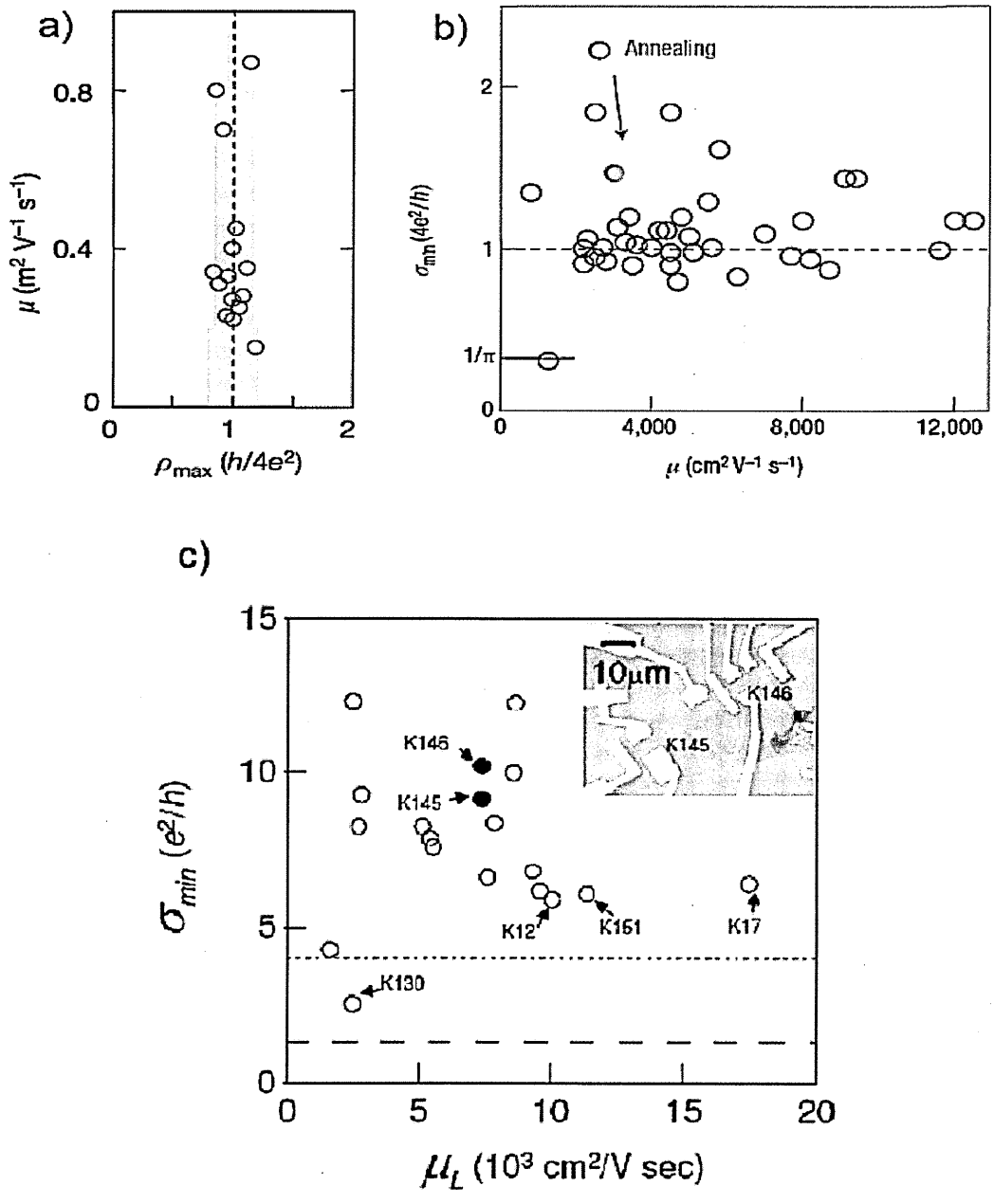

Figure 2.18: *The "universal" minimum conductivity (or maximum resistivity) as reported, (a) the figure is from [49] and (b) the figure is from [56], c) a range of minimum conductivity reported from [57].*

It is found that charge transport mobility and graphene's minimum conductance are influenced by factors like charge impurities [52, 58-59], vacancy defects [60], corrugation of the graphene sheet [61] and phonon scattering [62-63]. Chen et al. reasoned that individually, each factor k will contribute to a minimum conductance, σ_k.

Thus summing these contributing factors will give the final overall minimum conductance, σ_T [55].

While the investigations into the existence of a limit in the minimum conductivity of graphene under vanishing charge carrier density continues [2, 56], there has been a marked increase in number of reports that are more application orientated. In these reports, various graphene electronic devices were investigated. They ranged from high frequency range graphene transistors [53, 64], using the ambipolar transport behaviour of graphene to create novel frequency multipliers [65], polarity controlled logic inverter [66] to a single logic device that accepts multiple inputs [67].

Besides graphene's excellent conductivity, it was also observed that a free standing graphene will have a good optical transparency. The optical transmittance of a free standing graphene can be estimated by applying Fresnel equation and assuming that the optical conductance as shown below [4]:

$$T = (1+\frac{\pi\alpha}{2})^{-2} \qquad [2.3]$$
$$= 1-\pi\alpha$$
$$= 6\times10^{-5}$$
$$where\ G_o = \frac{e^2}{4\hbar}\ and\ \alpha = \frac{e^2}{4\pi\varepsilon c\hbar} = \frac{G_o}{\pi c \varepsilon_o}$$

Note c is speed of light, ε_o is permitivity of free space

Note that here G_o is defined as the universal optical conductance [68]. This implies a theoretical estimate of 2.3% absorption over the visible spectrum. Thus this combination of good transparency and good conductivity has led graphene to be a potential candidate to replace current transparent conductor like Indium tin oxide (ITO) [4, 69]. Furthermore, given the flexible yet robust nature of the graphene film [70] may also provide another alternative in the field of flexible displays.

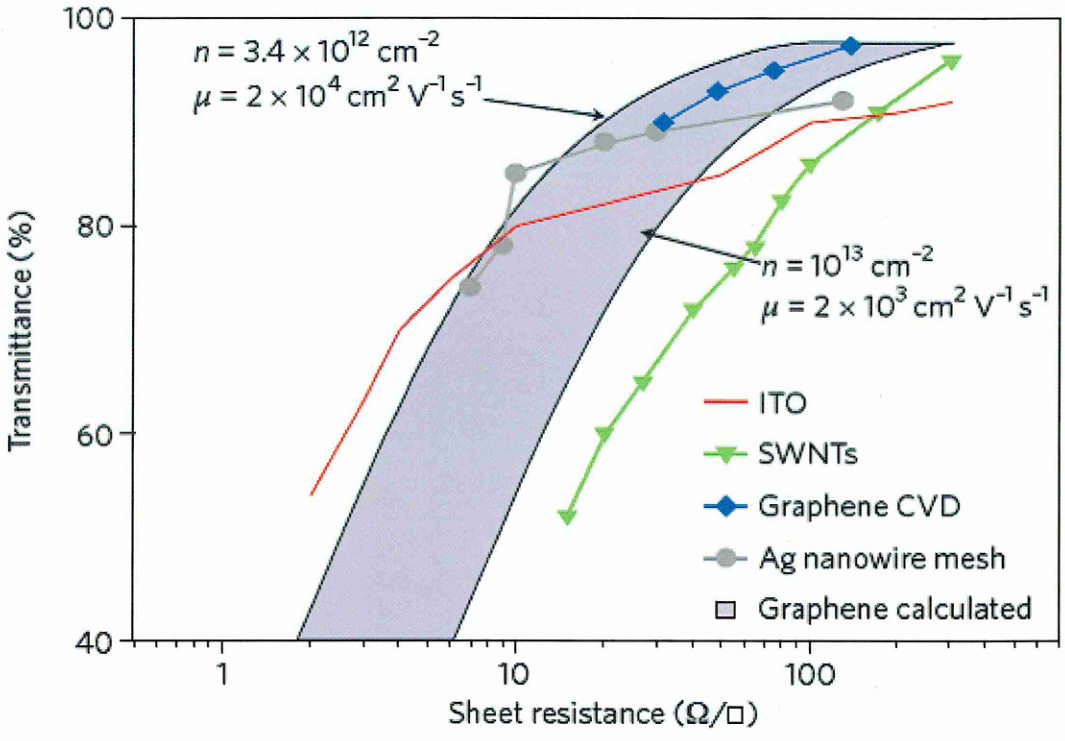

Figure 2.19: *Optical transmittance versus sheet resistance for different transparent conductors as shown in the legend. The shaded area enclosed by limiting lines for graphene calculated using various n and μ values in equation 2.4 below. X-axis represents the sheet resistance (ohms per square). From [4].*

Figure 2.19 [4] above summarised the current status of graphene as a transparent conductor in comparison to other competitive technologies like ITO, Ag wire mesh and percolation network of single wall CNT film. Bonaccorso et al., [4] proposed that a relationship (equation 2.4) between optical transmittance (T) and sheet resistance (R_s) may act as a basic ideal guideline for the trade-off between the two above parameters:

$$T = (1 + \frac{1}{\varepsilon_o c} \frac{1}{2R_s} \frac{G_o}{n\mu e}) \qquad [2.4]$$

where c is speed of light,

n is charge density in graphene

μ is charge mobility in graphene

Note that when n, charge density, is zero, nμe is equated to the fundamental limit G_o as defined in equation 2.3, which sets the minimum optical conductance possible in graphene [4, 68].

From equation 2.4, an ideal intrinsic sheet resistance of graphene may be approximated ~ 6 kΩ/□, with an optical transmittance of ~ 97%. Thus this implies that graphene is only superior to ITO in terms of transmittance, not sheet resistance. However by chemically doping graphene intentionally, Bae and co-workers [71] reported 20 Ω/□ with an optical transmittance of 90%. Thus it seems that chemically doping graphene is one major route to improve sheet resistance while keeping the optical transmittance at the optimal.

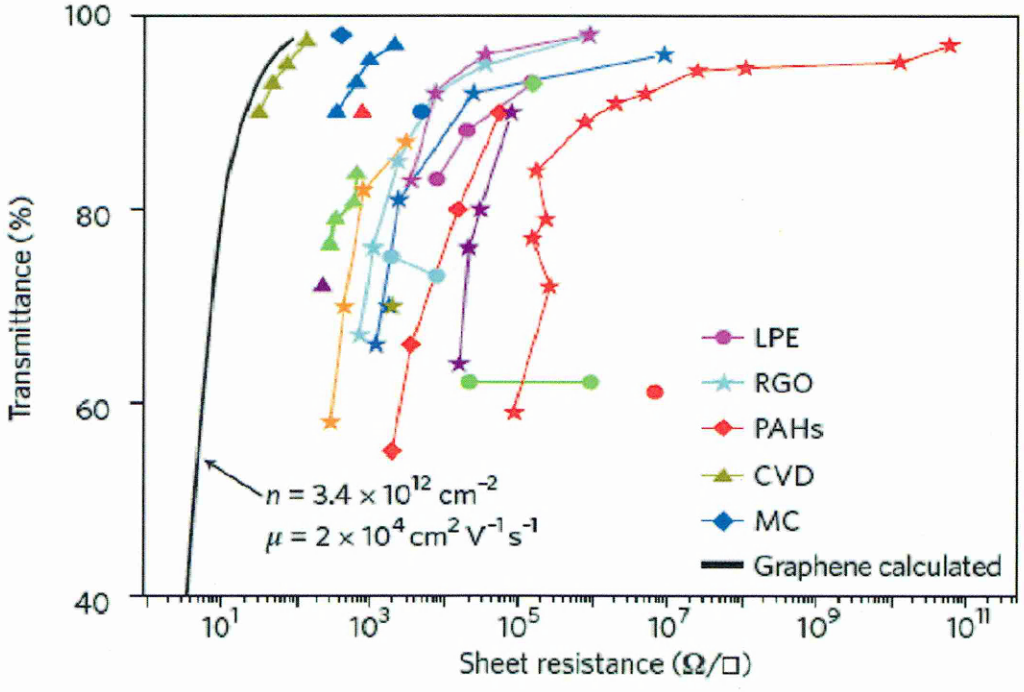

Figure 2.20: *Summary of graphene's optical transmittance versus sheet resistance as reported in literature. The results were grouped accordingly how the graphene films were prepared. The legend 'graphene calculated' refers to the calculated values using equation 2.2 with the stated n and μ values. Legend: RGO - reduced graphene oxide, MC – mechanical cleavage, PAH - polyaromatic hydrocarbons, CVD – chemical vapour deposition and LPE - liquid-phase exfoliation of pristine graphene. Figure is obtained from [4].*

Figure 2.20 [4] above summarised the current status of graphene's transittance versus sheet resistance as reported in the literature. As seen, at present CVD prepared graphene film has a better reported performance than other methods

Following the above discussion on the electronic and optical properties of graphene, the next section will discussed the various preparation methods reported in literature for graphene at length, with relevant discussions on the different models which postulate the formation of graphene under different conditions.

2.6.2 Current status of graphene FETs

A FET basically consists of a gate (which is separated from the channel by a barrier), a channel region and the connecting source/drain electrodes (Figure 2.21a). The basic idea of operation is to control the channel conductivity, and thus the drain current, by a voltage, VGS, applied between the gate and source.

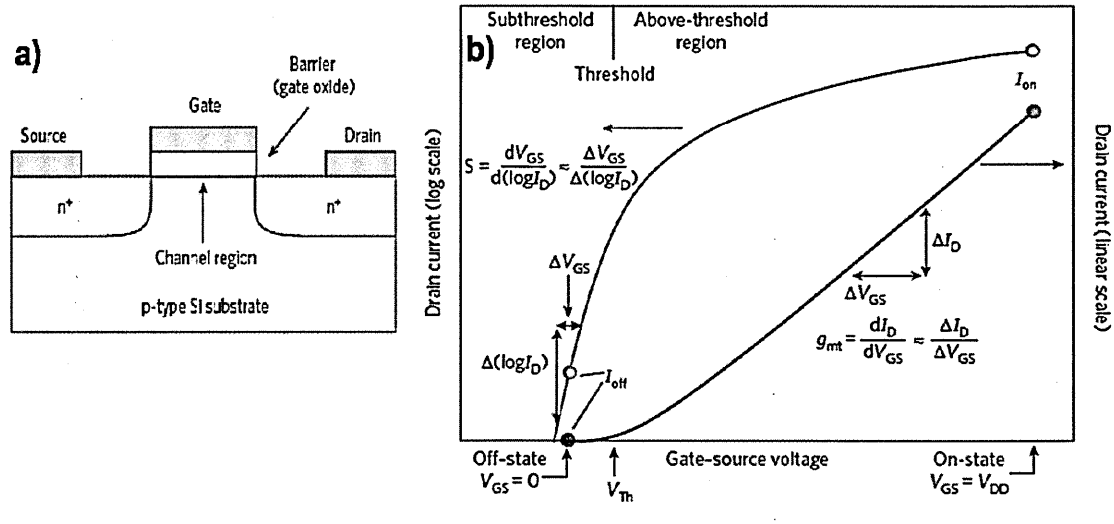

Figure 2.21: a) *standard FET design using a Si MOSFET as illustration. A conducting channel is formed when the voltage applied between the source and gate electrodes exceeds a threshold voltage. Channel length is defined by the length of the gate electrode.* ***b)*** *FET transfer characteristics showing drain current (I_D) (on a logarithmic scale on the left and a linear scale on the right) versus the gate–source voltage, V_{GS}. The transistor is switched ON when V_{GS} is equal to the maximum voltage supplied to the device, V_{DD}. Above threshold, the relationship between the change in drain current for a given change in V_{GS} is called the transconductance. Figures from [72].*

To improve the response of FETs, short gates and fast channel materials are often used. However short gate suffers from degraded electrostatics and other problems (i.e. short channel short channel effects) [73]. Scaling theory predicts that a FET with a thin barrier and a thin gate-controlled region will be robust down to very short gate lengths [74]. Thus channels that are one atomic layer thick represent the limit of this scaling which is why graphene is so attractive.

As mentioned earlier, graphene is a semi-metal or semiconductor with zero bandgap. This has often been cited as a major factor in the poor ON-OFF ratio (i.e. the current flow cannot be switched-off) of standard FET design using a single layer graphene [75-77]. The highest ON-OFF reported in GFET is ~ 100 [78], a few order of magnitude smaller than Si CMOS FETs. This meant that the usefulness of using graphene in a standard FET design for digital applications may be limited unless a bandgap can be created that is > 0.5 eV at room temperature [51]. While a bandgap in graphene has been demonstrated through the use of bilayer ABA stacked graphene [79] and graphene nanoribbon (GNR) [80], these devices posed serious challenges [51] in terms of nano-fabrications of GNRs and relatively small bandgap for bilayer GFET (~ 0.2 eV). It should be noted that alternative strategies to the opening of a bandgap in graphene had also been reported in the literature, and will be discussed in the following chapters.

Beyond the exploring of GFET in digital logic applications, the research on graphene transistors has also moved into the area of RF devices. In RF devices, it has been argued that the high speed and low noise are more important than the turning-off of the FET [51, 81].

Two important factors in a RF device are the cut-off frequency f_T which is defined as the frequency at which the device current gain drops to unity, and the maximum frequency of oscillation f_{max} as the frequency which the power gain becomes unity [82]. The recent progress in GFETs, as measured by f_T, against other semiconductor devices, is shown below (Figure 2.22a).

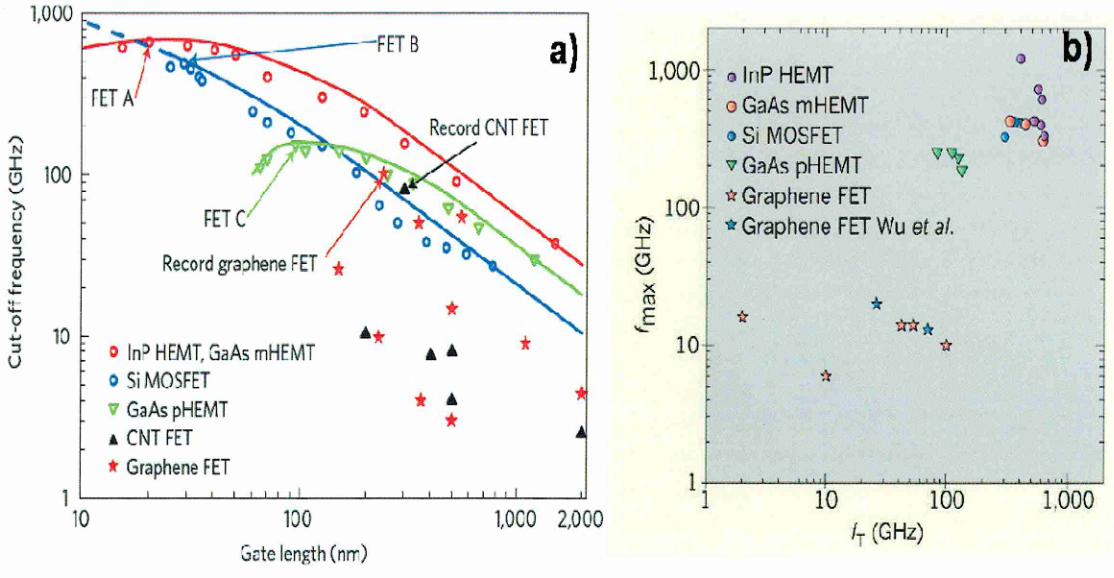

Figure 2.22: a) *comparing cut-off frequencies for different FETs. Cut-off frequency versus gate length for graphene MOSFETs, nanotube FETs and three types of radiofrequency FET; the symbols are experimental data points and the lines are a guide to the eye for type A (InP HEMT and GaAs mHEMT), B (Si MOSFET) and C (GaAs pHEMT) devices (as indicated). The FET A with the highest cut-off frequency (660 GHz) is a GaAs metamorphic HEMT (mHEMT) with a 20-nm gate. The FET B with the highest cut-off frequency (485 GHz) is a Si MOSFET with a 29-nm gate. The FET C with the highest cut-off frequency (152 GHz) is a GaAs pseudomorphic HEMT (pHEMT) with a 100-nm gate. The fastest nanotube device (CNT-FET) has f_T = 80 GHz and L = 300 nm, and the fastest reported graphene MOSFET has f_T = 100 GHz and L = 240 nm. Figure from [51];* ***b)*** *Comparison of reported RF GFET against other semiconductor RF FETs in terms of the maximum frequency of oscillation as a function of cut-off frequency. Figure from [83].*

Figure 2.22b showed the research progress in RF GFETs in the past few years. Currently, the fastest reported GFET has the cut-off frequency of 170 GHz with 90 nm channel length [84]. For perspective, cut-off frequency of around 600 GHz has been reported in GaAs metamorphic high electron mobility transistor with a 20 nm gate and in InP based high electron mobility transistor [51, 83].

Despite the progress in RF GFETs, they are still outperformed by InP and GaAs mHEMTs. While GFETs show quite high cut-off frequencies, when one examined the other important parameter - maximum frequency of oscillation (fmax), GFET is often lower much lower. For example, GFET [83] reported to having f_T of 155 GHz, but f_{max} ~ 10 GHz, a much smaller value. Since f_{max} basically indicates the transmitted power

(I^2R) possible in a RF FET device [82], unless there is improvement in *both* f_T and f_{max}, GFET will not have an advantage over current RF semiconductor devices made from GaAs and InP.

2.7 Graphene: growth and preparation methods

At present, the following four routes are the most commonly found methods for production of graphene:

- Graphene by mechanical exfoliation
- Graphene by chemical methods
- Graphene by sublimation of SiC
- Graphene by expitaxial growth on metal

2.7.1 Graphene by mechanical exfoliation

Geim and co-workers first reported the production of graphene via the mechanical exfoliation[49]. Since in a material like graphite where the out-of-plane (perpendicular) force is weaker (i.e. van der Waals bonding) compared to the in-plane atomic bonding, it is possible to cleave the graphene sheets along the in plane direction. This simple 'scrotch-tape' idea has evolved into is illustrated in the following diagram (as shown in Figure 2.23). First a piece of graphite is placed onto a wafer tape (green in colour as shown in diagram), followed by laying another piece of tape onto graphite and cleaving it. A few iterations of these actions will produce a thin graphite piece on one of the tapes, which in turn will be pressed and rubbed thoroughly onto a SiO_2 wafer. The end result is that a single or few layer of graphene will have adhered onto the SiO_2 surface.

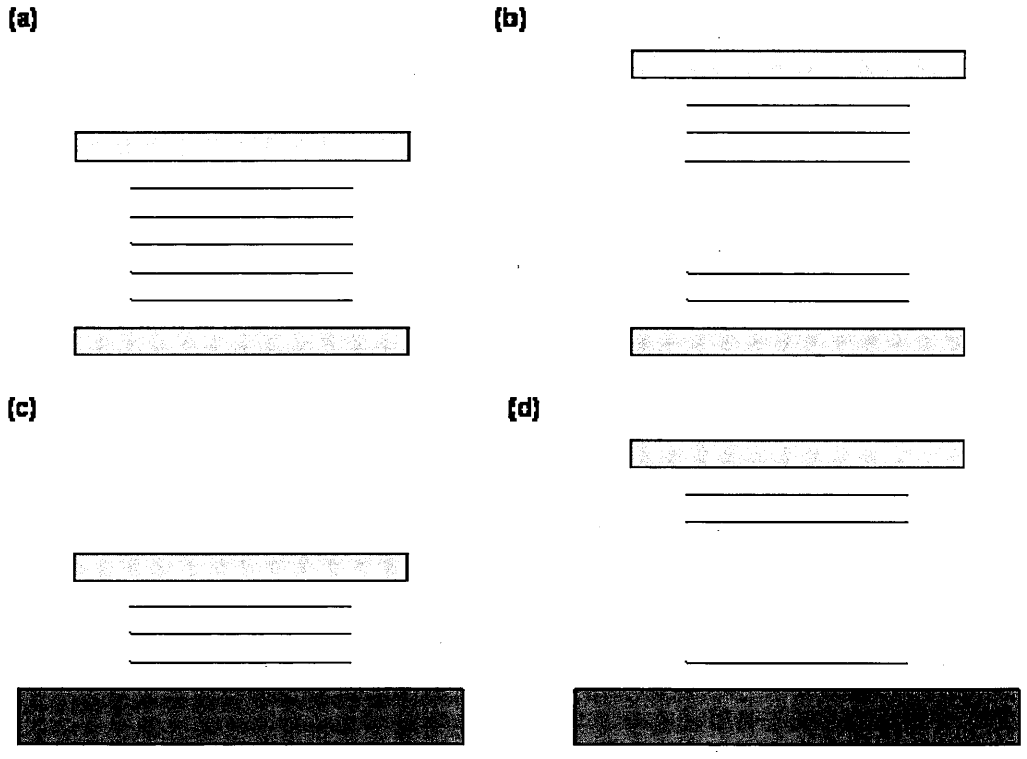

***Figure 2.23**: Steps (a) to (d) in mechanical exfoliation of single and few layer of graphene from graphite using wafer tapes for cleaving and transferring the graphene onto a SiO_2 wafer (shown in blue colour) by pressing and rubbing actions. Green represents graphite and blue represents the targeted substrate.*

While the above method is sufficient for scientific investigation, it is far from ideal for scaling up to higher production volume. To date, there have been reports in literature on investigations into adapting the above method to industrial scale production. One such method is the transfer printing idea [85] by using a SiO_2 mould or stamp to press onto a graphite substrate (HOPG) and then re-stamping the mould to deposit the graphitic layer(s), which has stuck to the mould's face, onto a pre-selected substrate target. Alternatively, instead of using a SiO_2 as a stamping mould, HOPG can be moulded into a stamp by using patterning it into a stamp itself using conventional lithography [86]. To improve adhesion of graphene onto the substrate target, one reported technique is to pre-treat the surface by oxygen plasma [85].

It is also possible to use electrostatic forces to assist in the cleaving of graphene. The diagram below shows the concept. The electrostatic force applied between the HOPG

stamp and the SiO_2 substrate target affects only the bottom most graphitic layer(s) due to the short screening length in graphite [87]. This in turns permits only a small number of layers to be exfoliated. Figure 2.24 shows the schematic of applying a voltage bias to achieve the electrostatic force for mechanical exfoliation graphene preparation.

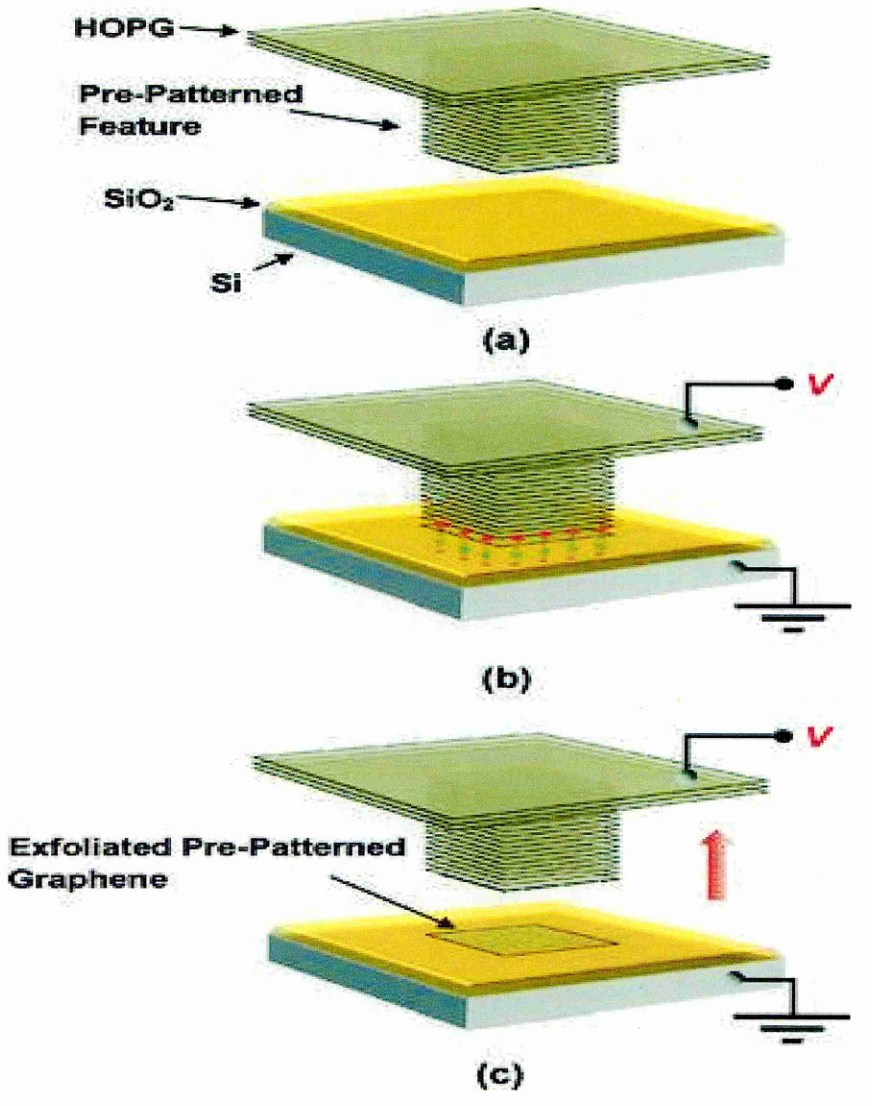

***Figure 2.24**: Procedures of electrostatic assisted cleaving of graphite to form graphene. In step (b), a voltage is applied while in contact and when separated in (c), a single or few graphene layer resulted being cleaved onto the substrate's surface[87].*

2.7.2 Graphene by chemical methods

It has been known that graphite oxide (GO) can be produced by Hummers method [88] and other variations of this concept [89]. Thus with these techniques, graphene can be

obtained from further subsequent chemical processing. Essentially, graphite is oxidized by strong acids, oxidants like sulphuric acid (H_2SO_4), potassium permanganate ($KMnO_4$), sodium nitrate ($NaNO_3$) to produce GO. After this, GO is exfoliated using sonication to create stable aqueous dispersions of individual sheets. GO structure is shown below:

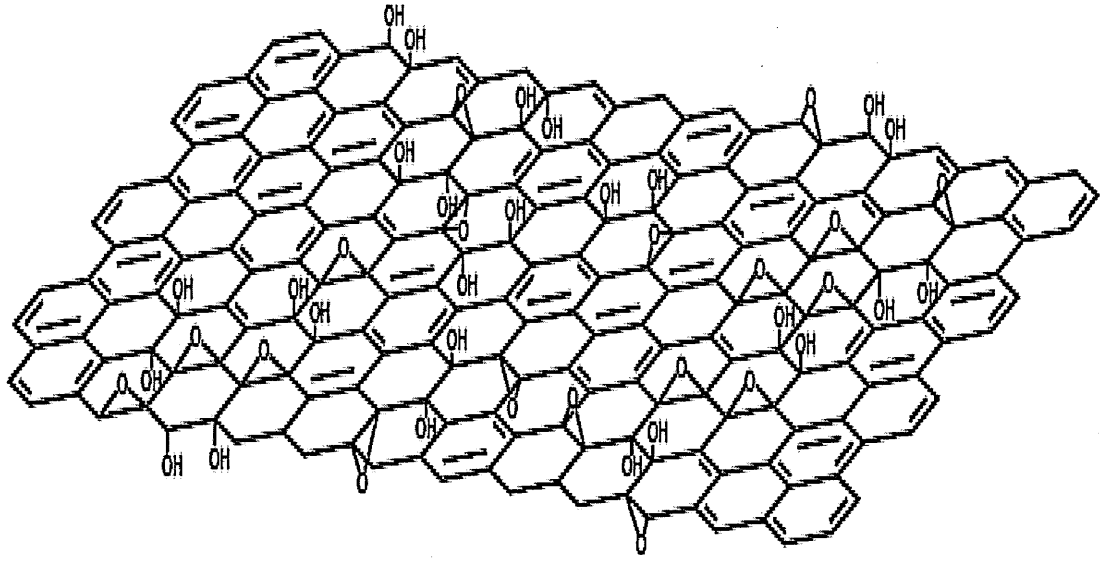

***Figure 2.25**: Schematic showing the structure of GO which shows hydroxyl OH and epoxide group C-O-C [89].*

A significant number of carbon is bonded to various group like hydroxyl (OH), epoxide groups (C-O-C) and C=O groups after the graphite undergone oxidation. As a result of oxidation, GO is insulating and will need further processing to obtain back the chemical structure of graphene. To achieve this, GO may be reduced to graphene using chemical reductants like hydrazine (N_2H_4), dimethylhdyrazine ($C_2H_8N_2$), hydroquinone ($C_6H_4(OH)_2$), and sodium borohydride ($NaBH_4$) [89]. It should be noted that reduction by hydrazine for example may not completely restore GO back to the chemical structure of pristine graphene [89]. This is shown when the GO is examined before and after chemical reduction under C1s X-ray Photoelectron spectroscopy (XPS).

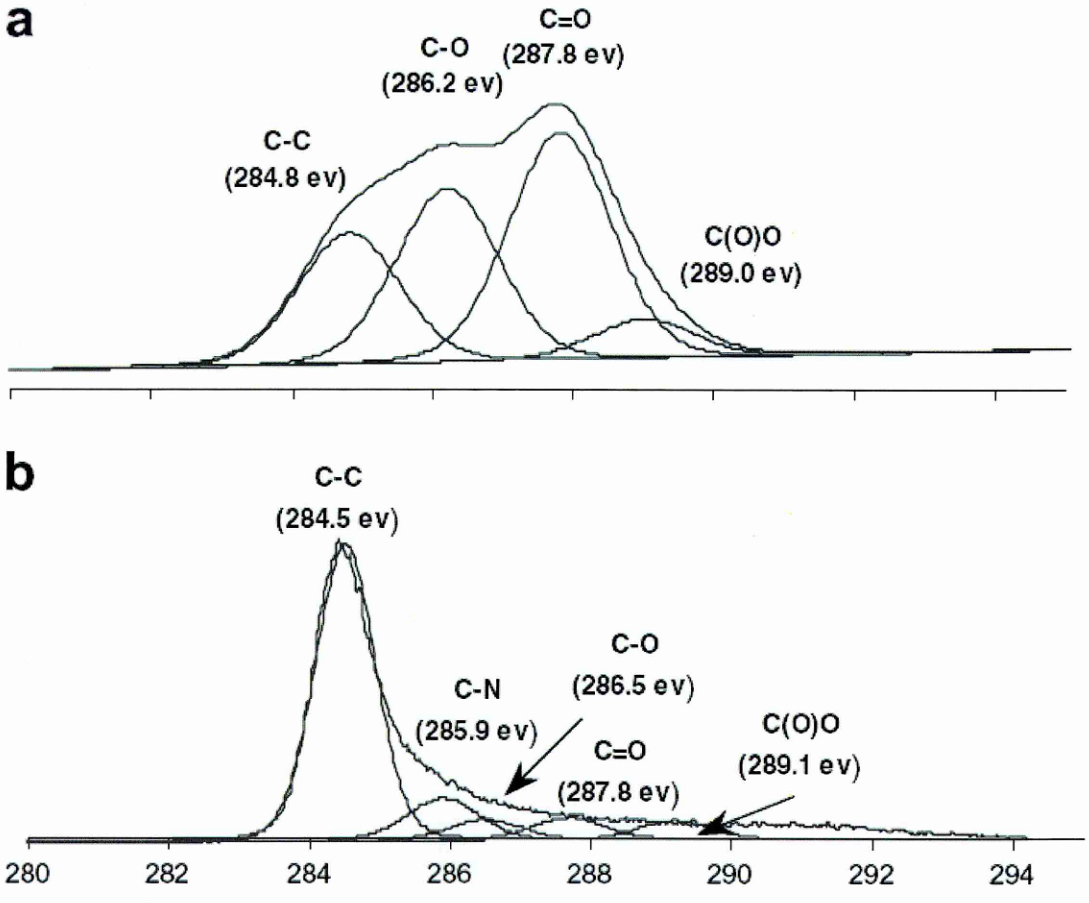

***Figure 2.26**: C1s XPS of GO before (a) and after (b) reduction by hydrazine hydrate for 24hrs at 100 °C [90].*

The C1s XPS spectrum of GO indicated oxidation in the material with four components that correspond to carbon atoms in different functional groups: the non-oxygenated ring C (284.8 eV), the C in C–O bonds (286.2 eV), the carbonyl C (C=O, 287.8 eV), and the carboxylate carbon (O–C=O, 289.0 eV) [90]. Although the C1s XPS spectra of the GO after reduction also exhibited similar oxygen functionalities as before, the peak intensities of these components were smaller than before reduction. This may be an indication of 'de-oxygenation' by the hydrazine reduction. The added component at 285.9 eV corresponding to the C in the C=N bonds of hydrazones [90]. Non chemical reduction of GO by means of thermal annealing has also been explored [90].

2.7.3 Graphene by sublimation of SiC

In this method, silicon carbide (SiC) is heated to high temperatures (>1100°C) to reduce it to graphene [91]. This process produces a sample size that is dependent upon the size of the SiC substrate used. Graphene on silicon carbide can be patterned using standard microelectronics methods, thus creating the possibility for large scale integrated electronics on SiC epitaxial graphene [92].

Two most commonly reported SiC used for graphene growth is 4H-SiC and 6H-SiC. The Ramsdell notation is such that 4H refers to a hexagonal (H) lattice in which the stacking sequence of SiC bilayers is repeated every 4 layers. Similar principle applies for 6H-SiC structure. The figure below illustrates the structures of 4H and 6H SiC respectively:

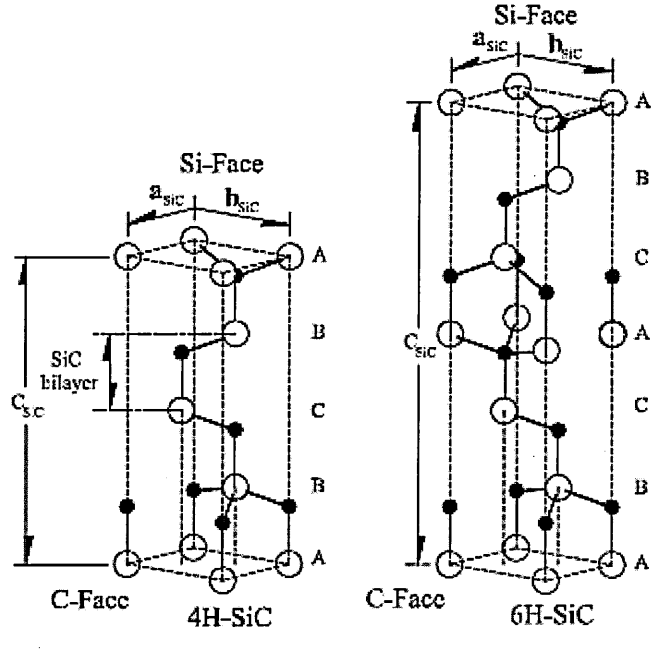

***Figure 2.27**: 4H (left) and 6H (right) SiC structure respectively. Open circles are Si and dark circles are C atoms [93].*

Since termination of SiC can either be C (C-face) or Si (Si-face) terminated, there is a reported difference between the graphene grown using SiC of different terminations in terms of kinetics, surface roughness and stacking order of the as grown graphene.

Compare to C-face SiC, Si-face SiC tends to produce graphene layers that is less influenced by process time and temperature, which incidentally is also lower. The as grown graphene from C-face tends to have a lower surface roughness than that produced from Si-face SiC as measured by AFM and furthermore can have a longer terrace (1 ~ 2 micron) as well [93].

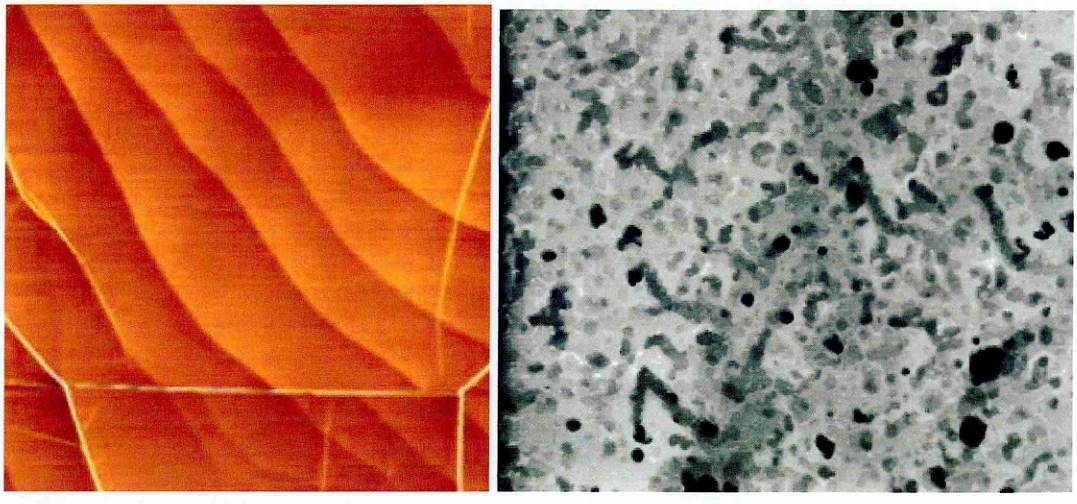

***Figure 2.28**: AFM images of UHV grown graphene using different SiC terminations: C-face (left) and Si-face (right). Note that colour scales are arbitrarily set. From [93].*

2.7.4 Graphene by expitaxial growth on metal

Since 1960s, there have been reports on investigations into graphitic growth that typically involved decomposition of hydrocarbon over various transition and precious metals. Some of the metals used are Ir(111) [94], Ru(0001) [95], Pt(111) [96], Ni(111) [97], and tungsten carbide [98]. Growth of graphene using CVD can be achieved with carbon dissolution-segregaton-precipitation which is a process whereby hydrocarbon pyrolysis over metallic catalysts (although non metallic materials like porcelain [99] had also been reported), followed by desolution of carbon into the metallic catalysts and finally precipitation of graphitic films upon cooling [100-101]. The other proposed mechanism is via direct deposition accomplished via using a metallic substrate with negligible carbon solubility at the CVD process temperature. Investigations of graphene growth using rutherium illustrated the possibility of exploring these two methods.

Loginova and co-workers used low temperature (500 – 700°C) to avoid carbon diffusion into rutherium during evaporation of carbon source for graphene growth [102] while Sutter and co-workers promoted graphene formation on rutherium via carbon dissolution and segregation of carbon at higher temperature (850 – 1150°C) [95].

Besides the above mentioned UHV based CVD for graphene growth, there is also interests in alternatives like an atmospheric and low pressure (~ 10^{-3} Torr) based CVD for graphene growth as UHV process is considerably more expensive. Among these, the most widely reported metal used is Ni [103-105] and more recently the use of copper as catalyst [106-107].

To further the understanding on graphene formation on metals, the carbon segregation process model, developed to account for graphene formation on nickel catalyst and in general for metals with high carbon solubility, is examined below.

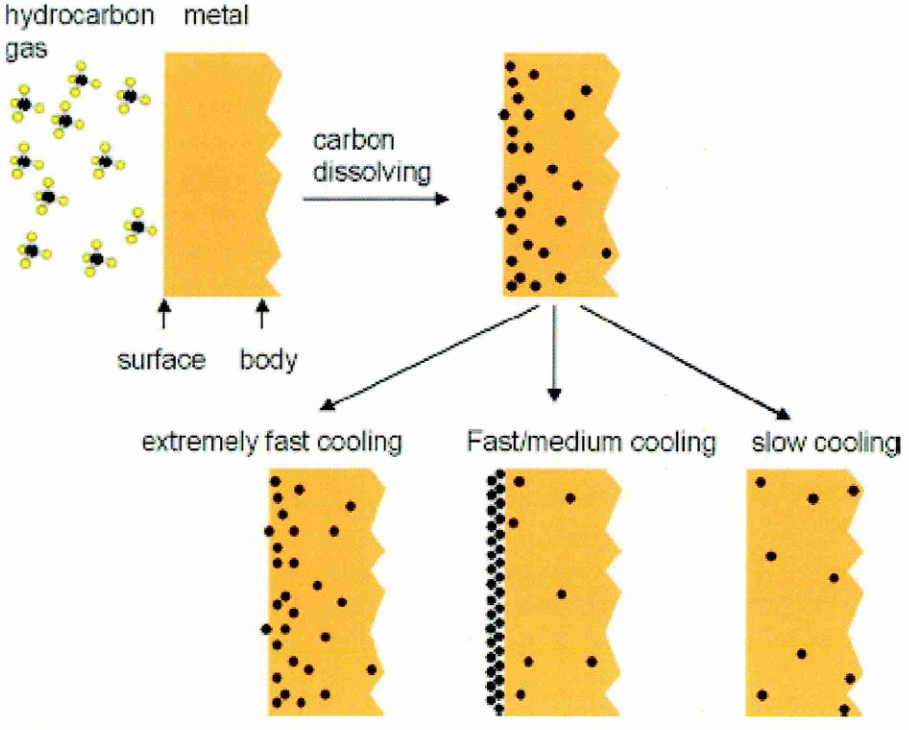

***Figure 2.29**: Carbon segregation at metal surfaces. Different cooling rate results in different surface carbon formation [103]*

The mechanism for graphene formation via carbon segregation (Fig 2.29) follows the following steps. It is thought the hydrocarbon molecules first decompose at the Ni surface and henceforth carbon atoms diffuse into the metal. Conceptually, the concentration of carbon would decrease exponentially from the surface into the bulk. Thus by keeping this step to a short time, the aim is to keep the carbon concentration low. Next carbon segregation would occur as samples cool down. Cooling rate is an important parameter to consider in this process.

Different cooling rates lead to different segregation behaviours. Extremely fast cooling tends to result in a quenching effect in which the solute atoms lose the mobility before they can diffuse while under extremely slow cooling rate, carbon will have enough time to diffuse into the bulk, so there will not be enough carbon segregated at the surface. Thus a compromising medium cooling rate(s) will allow just sufficient amount of carbon to segregate at the surface.

In contrast to graphene formation on Ni, there is a significant difference in the growth process when Cu, a low carbon solubility metal, is used. In a recent development, Li *et al.* compared the differences between graphene growth mechanisms on Ni and Cu using low pressure CVD (LPCVD) process at 1000 ^{o}C [108]. Using carbon isotopes ^{13}C and ^{14}C (in black dots, while ^{12}C is in red dots - illustrated in the Fig 2.27) they observed the following behaviour. For Ni based graphene CVD, the isotopes distribution seems to be randomly distributed while in Cu based graphene CVD, the isotopes are found mostly at the peripherals. What this implies is that under formation of graphene in Cu, there is minimum absorption into bulk thus the first arriving carbon form-up sequentially.

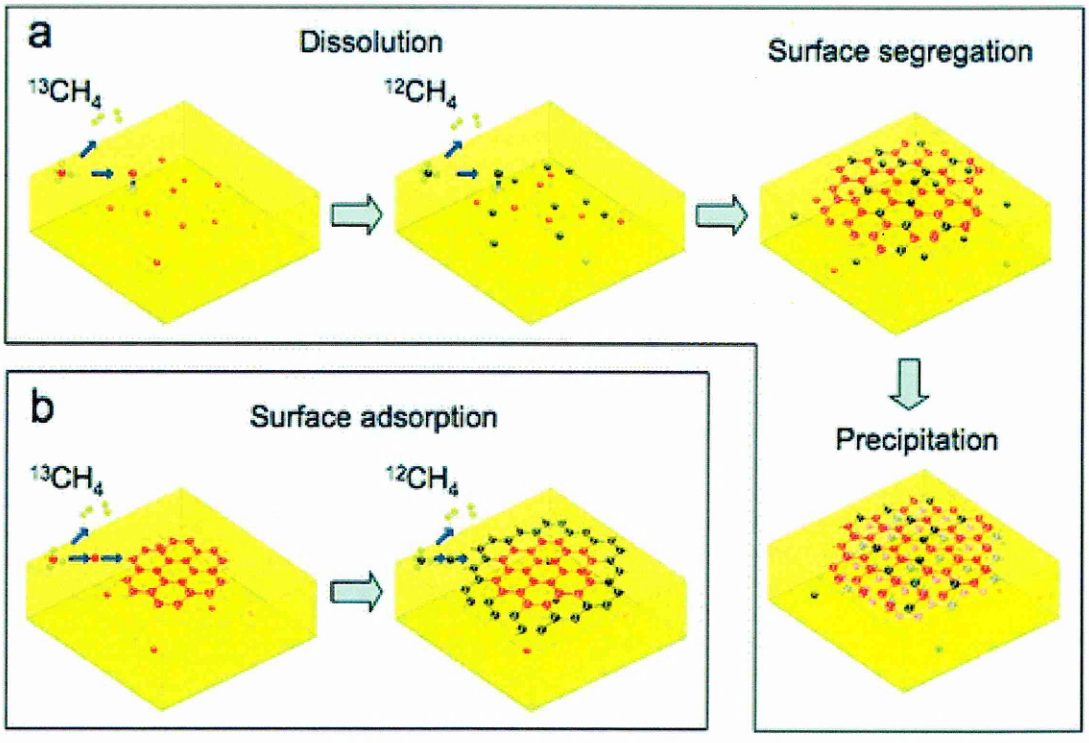

***Figure 2.30**: Schematic diagrams of the possible distribution of C isotopes in graphene films based on different growth mechanisms. (a) Formation on Ni surface - graphene with randomly mixed isotopes resulting from surface segregation and/or precipitation indicating that carbon absorption and re-precipitated to the surface upon cooling, (b) Formation on Cu - Graphene with separated isotopes resulting from surface adsorption. Note the order in this formation which implies a 'first-in first form' formation and also minimum absorption into the bulk of the film [108]*

They proposed that graphene formation on Cu is based on surface adsorption and is self limiting, which is different from growth of graphene on Ni which is based on the carbon segregation process. They further proposed that the self limiting arises due to the lack of strong catalytic and carbon solubility effect in Cu (unlike Ni) to promote decomposition and further growth after the initial layer of graphene is deposited.

Further evidence in the difference between Ni and Cu based growth process comes from observing one of the parameters in graphene formation which is cooling rate. According to Li and co-workers cooling rate is not a major factor when using Cu as the underlying metal for growth [106], unlike in Ni where single layer graphene was found mostly under a medium (~ 10^{o}C/min) cooling rate [103]. Reina and co-workers also reported 'the right cooling rate' will produce single/few layer graphene [109].

2.8 Conclusion

In this chapter, separate reviews on various preparation methods for CNT and graphene were discussed. Emphases were especially placed on chemical vapour deposition methods for producing both CNT and graphene. It is interesting to note that in principle, by changing the size of the metal catalyst from nanoparticle size to a thin-film sheet, the carbon atoms can be formed into graphene instead of CNTs. Besides looking at the growth process, electronic and optical properties of graphene and its application to different devices were also discussed. In the next chapter, various experimental techniques used throughout the studies reported in this thesis are introduced and analyzed.

CHAPTER 3

Experimental methods and techniques

This chapter describes a series of experimental methods and tools used throughout the studies reported in this work. They are the photothermal based CVD (PT-CVD) growth tool, and the various analytical tools used for characterizing carbon nanotubes and graphene. Furthermore a basic overview of an organic solar cell and its characterization method is also described.

3.1 Photothermal CVD growth tool (PT-CVD)

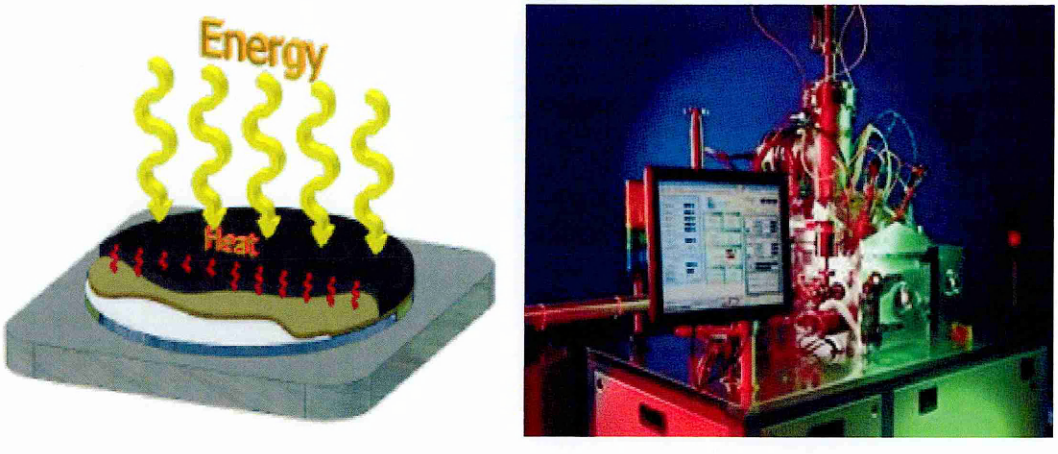

***Figure 3.1**: (Left) Cartoon illustrating the concept behind the design of the Surrey NanoSystem growth tool. The substrate (silver) sits on a liquid-cooled substrate support. The substrate coating (black and brown) reflects the infrared radiation energy delivered from the top and also acts as a thermal barrier between the growth front and the underlying substrate [110]. (Right) Actual implementation of the concept. (Courtesy of Surrey NanoSystem Co.)*

Surrey NanoSystem, a spin-off company from the University of Surrey, has developed a commercial prototype low pressure plasma enhanced chemical vapour deposition tool which employs optical heating as the energy source (i.e. photothermal process) instead

of the conventional substrate heater design. The concept of this design is illustrated in Figure 3.1.

The basic aim behind the design of this tool is to enable the development of low temperature growth process for carbon nanomaterials that is essentially CMOS compatible. The key to this design is the exposure of a pre-deposited layer(s) of growth catalyst(s) to a combination of top side heating with bottom side cooling [110]. Thermal heating energy is introduced through the use of an infrared (IR) heating source from tungsten halogen bulbs, mounted to the top side of the substrate. The usage of IR heating allows the rapid introduction and ramp-up of thermal energy to the catalyst(s) on the substrate, while simultaneously a cooling fluid (e.g. cold, fast flowing water) flows through the chuck that is supporting the growth catalyst(s).

It was also found that an addition of a thermal barrier layer (TBL) [111] on the substrate's surface can greatly enhance the surface temperature profile while still keeping the underlying Si wafer below 400°C. This TBL has two purposes: 1) to reflect IR energy away from the substrate back onto the catalyst and 2) act as a physical thermal barrier between the growing carbon nanomaterial (in this investigation - CNTs was grown) and the underlying Si substrate [110].

Finally, the primary measurement of temperature is via an optical pyrometer. This pyrometer (BASF Exactus model) is pre-calibrated against the freezing point of Al. Thermal radiation from the IR source irradiating onto the wafer is fed into the optical pyrometer via a YAG light pipe situated under the wafer. The system also caters for secondary connection of a conventional thermal couple (TC) as an additional thermal sensor, however due to the rapid thermal heating it will be necessary to have a small body (i.e. small heat capacity) TC to ensure accuracy.

3.2 Thermal CVD growth tool (T-CVD)

Figure 3.2 (Top) shows a schematic of the furnace and the actual equipment (Figure 3.2 bottom). Three types of gases - methane, hydrogen and helium are available to selectively injection into the furnace. Figure 3.2 (b) shows a schematic image of a cross-sectional view of the furnace. The quartz tube has a 3 inch diameter and is 1 m long. The maximum operating temperature is at 1200°C. The gases are introduced through the right hand side metal pipe and flow into the quartz tube with the exhausts passing out the other end. Metal plates are placed in the quartz tube near the flanges to reflect the heat toward the middle of the quartz tube. The reflections result in the reduction of the heat distribution at the middle of quartz tube and also avoid the heating up of the flanges which include o-rings.

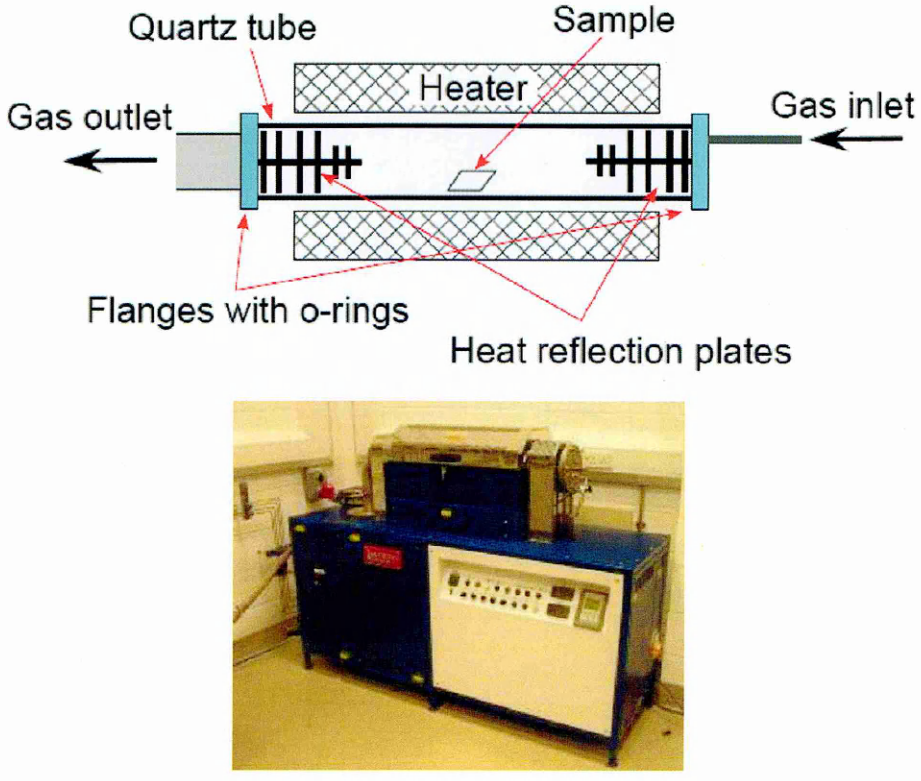

Figure 3.2: *(Top) Cross-sectional diagram of a T-CVD furnace used in this study [7] and (bottom) photograph of the equipment. The metal plates in the schematic are placed near the both ends of quatz tube to reduce a distribution of heat at the middle of the quartz tube and to avoid the excess heating up of flange which possibly results in degreations of o-rings in the franges.*

3.3 Raman spectroscopic characterisation of carbons

Raman spectroscopy is a technique commonly used to study vibrational and rotational modes in crystals by making use of the scattering effect on the incident monochromatic light illuminating the crystals. In a solid sample, this scattering occurs due to the interaction with vibrational modes of the crystalline structure. This interaction resulted in frequency shift of the scattered light. Using classical physics, the relationship between the polarizations of the crystal due to the local electric field created from the incident light is shown below [112]:

$$P = \alpha E \qquad [3.1]$$

where P is the polarization vector describing the displacement between positive and negative charges, E is applied electric field of the general form: $E = E_o \sin\omega_o t$, and α is the polarizability tensor of the atom in the crystal sample.

Assuming that the polarizability tensor is modulated by crystal vibration, thus α can be further expanded into the following equation 3.2:

$$\alpha = \alpha_o + \alpha_1 \sin\omega_q t \qquad [3.2]$$

where ω_q is defined as frequency of the atomic vibration coupled to the incoming light.

Thus, the resulting equation is:

$$P = E_o(\alpha_o \sin\omega_o t + \frac{1}{2}\alpha_1 \cos(\omega_o - \omega_q)t - \frac{1}{2}\alpha_1 \cos(\omega_o + \omega_q)t) \qquad [3.3]$$

Equation 3.3 shows that light can be scattered both elastically (first term) and inelastically by a downshift (second term) and an upshift (third term) in frequency. A downshift in frequency is referred to as the Stokes Raman shift while an upshift is the

anti-Stokes Raman shift. The Stokes process refers to the emission of a phonon and the anti-Stokes process to the absorption of a phonon in the scattering process [112].

Furthermore, both energy and momentum conservation must be considered in the Raman process:

$$E_s = E_i + E_q \text{ and } k_s = k_i + k_q$$

where E and k are the energy and momentum, respectively, of the incident (i) and scattered (s) light and the lattice vibration or phonon mode (q) involved.

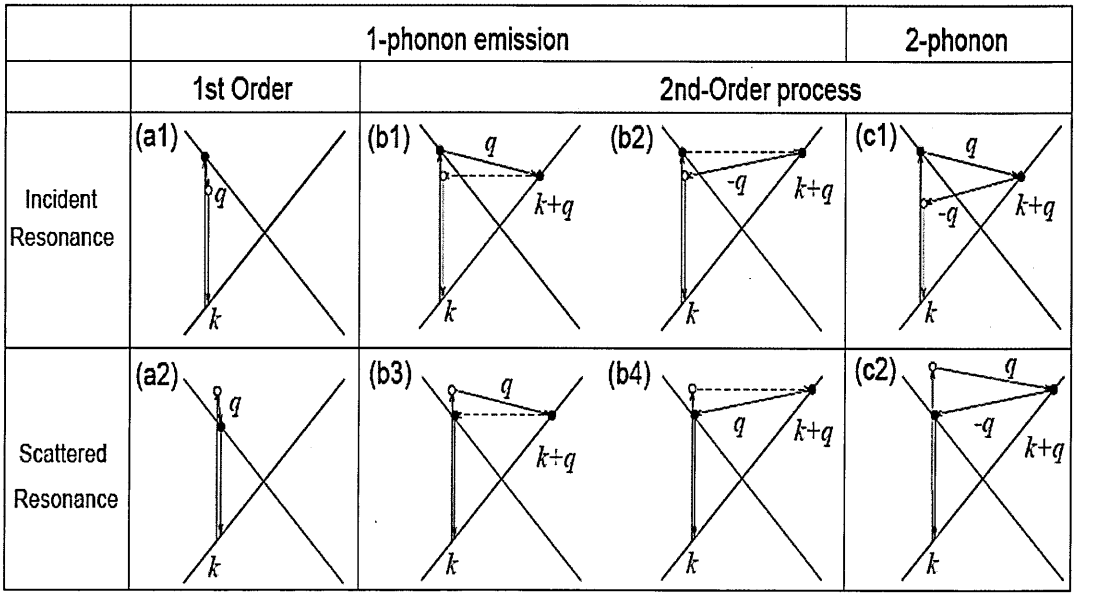

***Figure 3.3**: Classification of first and second order Raman process in a momentum (q) vs energy (k) diagram for both incident and scattered resonance. Incident and scattering resonance are explained in the following text. Note that for the more complex second order Raman process, there are two distinct cases: 1) one phonon process involved one elastic scattering and 2) two phonons with equal magnitude but opposite direction [113-114].*

At this point, it is important to bear in mind that carbon nano-materials are low dimensional systems, thus the existence of discrete transition energies for electrons enhances the scattered Raman signal since these transitions increase the probability of the electron-phonon interactions. The process whereby the energy of the incident and

scattered light coincide with an electronic transition in the material is known as resonance Raman process.

Figure 3.3 shows the *E-k* diagram of zero bandgap carbon nano-material. As seen, the incident resonance refers to a process via the following steps: 1) an incident laser energy that excites an electron from a lower to higher electronic state, 2) the electron subsequently loses energy and with an accompanying phonon emission, the electron then occupies a virtual electronic state, 3) finally the electron recombines with its initial state with an accompanying photon emission. Thus the phonon energy can be inferred from the difference between incident and scattered photons from the whole process.

For the case of scattered resonance, the main difference lies in that the incident laser energy excites the electron to a virtual state first, loses energy to occupy a lower electronic state with a phonon emission as before, finally recombining to emit a photon. All the above descriptions are for the Stokes process. Similar behaviours can be described for an anti-Stokes process. For the first and second orders of the Raman processes illustrated in the above figure, they refer to the one and two scattering events respectively. For first order event, the momentum of the vibration mode is approximately closed to zero, and in a second order Raman process the vibration modes with non-zero momentum can be probed [113].

Not every molecular vibration can be studied with Raman spectroscopy. In order for Raman scattering to take place the molecule has to be affected by a vibrational mode in such a way, that its polarizability is changed [112]. In this way the outgoing photons reflect the modification of the molecule's optical response by a vibration. The Raman active vibrational mode is mechanically deforming a molecule, varying the distances between the atoms, constantly modulating the polarizability with the frequency of the given molecule's vibration.

The system that was used throughout this thesis is a Micro-Raman spectroscope (Ranshaw Micro-Raman) consisting of a laser focused onto a small spot of the sample in the order of a few micrometers, using an optical microscope. The scattered light is then collected by the microscope's objective lens and deflected to a spectrometer. The Raman spectra are recorded in backscattering configuration.

3.3.1 Raman spectroscopy of Carbon Nanotube

There are several peaks which are interesting for the analysis of carbon nanotubes. The first is the "G band" around 1582 cm^{-1} (whereas G means graphite) [12, 114]. The Raman G mode is considered as a first order Raman process, visually this mode arises due to atomic vibration as shown in Figure 3.4. As a comparison to other graphitic materials, Figure 3.5 below detailed the various forms of Raman G mode/band and their corresponding carbon structures.

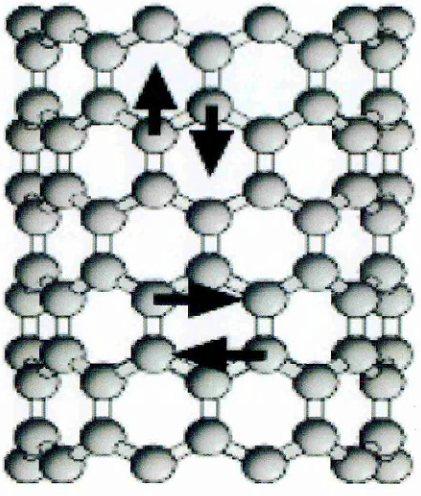

***Figure 3.4**: Schematic of two atomic vibrations giving rise to G modes/band in SWCNT. Note that circumferential displacements gives rise to G^+ mode while G^- mode is due to the curvature of the CNT which softens the vibration in the circumferential direction [12, 115].*

As seen in Figure 3.4 the G band of MWCNT is quite indistinguishable from that in HOPG graphite. For the case of SWCNT, the G mode in SWCNTs gives rise to multi-peak features, where up to six Raman peaks can be observed [12]. However, a simple

analysis can be carried out considering just the two most intense peaks: Firstly, G+, for atomic displacements along the tube axis as shown in Figure 3.5, and secondly, G–, for atomic displacement along the circumferential direction as shown in Figure 3.4 [115].

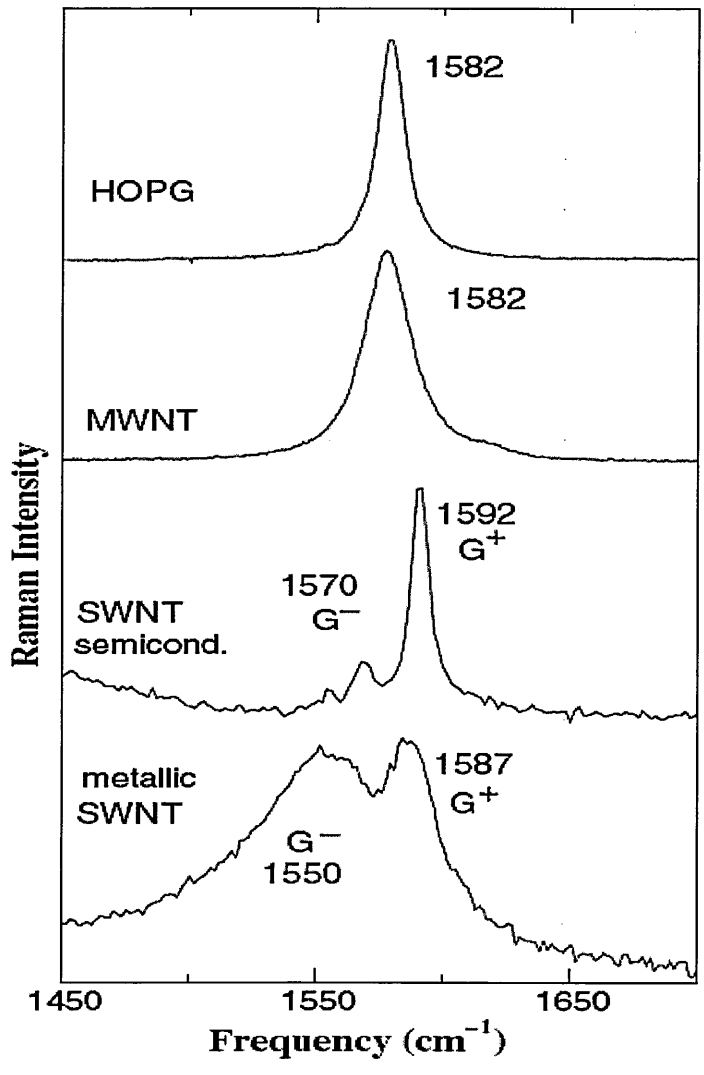

***Figure 3.5**: G bands for various carbon materials. For SWCNT, G has two main modes G^+ and G^- due to the atomic vibrations shown previously [12, 115].*

The second Raman mode is the D-band which is considered to be a one-phonon second-order Raman process that involves one phonon scattering and one elastic scattering with a defect. Thus this mode is forbidden in perfectly ordered graphite and becomes only active in presence of disorder. The Raman D band exhibits laser

wavelength dependent and it will also shift upward with increasing laser excitation energy.

One of the interests in studying disorder mode under Raman spectroscopy is for defect characterization in CNT [12, 114]. There are two distinctions between D mode in graphite and D mode in CNT are: 1) the D band's frequency is lower in CNT than that of graphite, and 2) it is usual to observe the Raman spectra from SWNT samples to be composed of both a broader peak and a sharper peak, the broad feature coming from amorphous carbon while the sharper feature coming from the CNTs [116].

It is possible to define a ratio of the D to G-band which is inversely related to the crystallite size of graphite [117-119]. Maultzsch and co-workers [120] studied the ratio of D/G for MWCNT as a function of doping level (boron doping in MWCNT for study of defect concentration control). The results indicated that as the doping level increases, the D/G ratio also increased. Antunes and co-workers further investigated the sensitivity of the ratio as a function of laser excitation wavelengths [121]. They found that under IR Raman excitation, the ratio displayed much higher sensitivity to the presence of structural defects in various carbon materials like CNT, CNF and graphite. It should be noted that beside the use of D/G ratio as an indication of defects, another Raman mode has a similar effect. This mode – D' mode (~1618 cm^{-1} which is on the right shoulder of G peak) is typical of defective graphite-like materials [12, 114].

The last Raman mode of interest (usually in the range: 120 $cm^{-1} < \omega_{RBM} < 250\ cm^{-1}$), Radial Breathing Mode (RBM), is very useful for characterizing a SWCNT's diameter through the relationship:

$$\omega_{RBM} = \frac{A}{d_t} + B \qquad [3.4]$$

where A and B are empirically determined, d_t is the diameter of the tube.

The atomic vibration that resulted for a RBM mode is showed in the following figure.

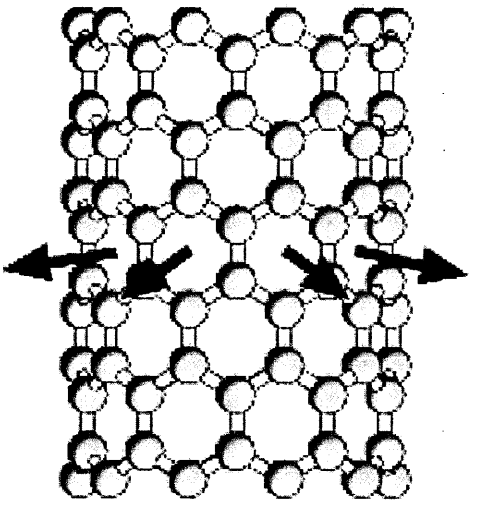

***Figure 3.6**: Atomic vibration for Raman's RBM mode in SWCNT [12, 115]*

For MWCNT, the Raman RBM from large diameter is usually too weak to be observed.

3.3.2 Raman spectroscopy of graphene

At present besides Raman spectroscopy, there are other methods (e.g. Scanning Tunneling microscopy ~ STM, Electron diffraction ~ ED) for identifying graphene as reported in the literature. However, Raman's attractiveness as a characterization tool for carbon nano-material in general and graphene in specific lies in that it is non-destructive, fast, with good resolution and gives the structural information [122].

Besides sharing the common Raman mode G and D with CNT and graphite as mentioned earlier, there is the existence of a 2D or G' mode – a two-phonon, second order Raman process, which like D mode also displays frequency dependence on laser energy [113]. It has been proposed that this Raman 2D mode is a useful tool for identifying the layer counts in graphene prepared as previously discussed. In comparison, tools like AFM which has been used to identify one to a few layer thick

graphene, has lower throughput and the apparent measured thickness of 0.5 ~ 1 nm is thicker than expected from interlayer graphite spacing [49]. Others like optical microscope imaging have also been used to identify graphene on SiO_2. It was found that thickness of SiO_2 strongly influenced the visibility of graphene [123], thus a 5% change in thickness (from 300 nm to 315 nm variation) will significantly lower the visibility of graphene [124].

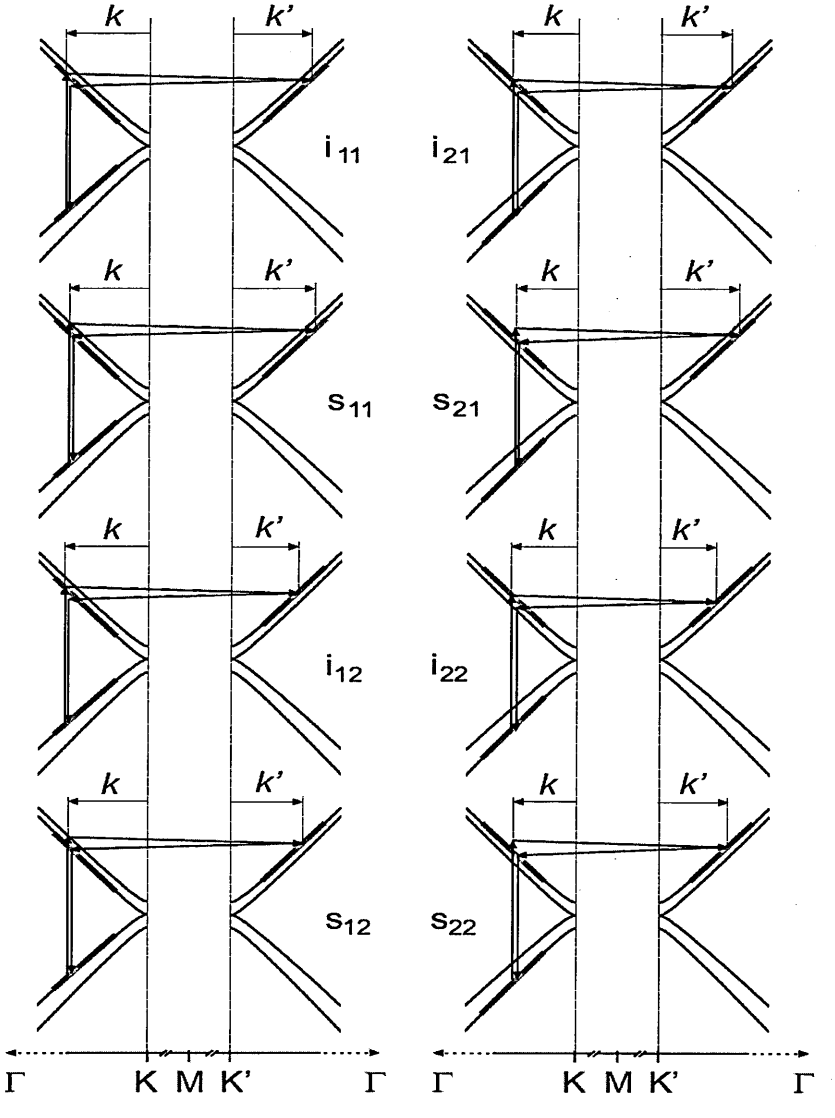

***Figure 3.7**: Two-phonon double resonance processes in a bilayer graphene, where s=scattered resonance, i=incidence resonance. A total of eight processes are possible under this model with four pairs of the eight cases being degenerate. Usually the Raman 2D can be fitted to four peak components [125-126].*

Following on from the work on using Raman spectroscopy for other carbon materials like CNTs, C_{60} and graphite, Ferrari and co-workers in a series of reports highlighted the Raman signature of single and few layer graphene (prepared via mechanical exfoliation) using Raman spectroscopy [122, 127]. To show how Raman spectroscopy can be used for identifying graphene layers, the Raman spectra for a bilayer graphene is considered in the following. Figure 3.7 illustrates the Raman spectra of an ABA stacked bilayer graphene with the underlying processes that give rise to this spectrum. As seen, there are two photons, second order resonance led to eight distinct processes which can be mathematically curve-fitted using four distinct Lorentzian peaks.

It was further observed that the Raman 2D peak will change in shape, width and position for increasing layer counts [128]. The figure below shows the evolution of the 2D peak with increasing layers.

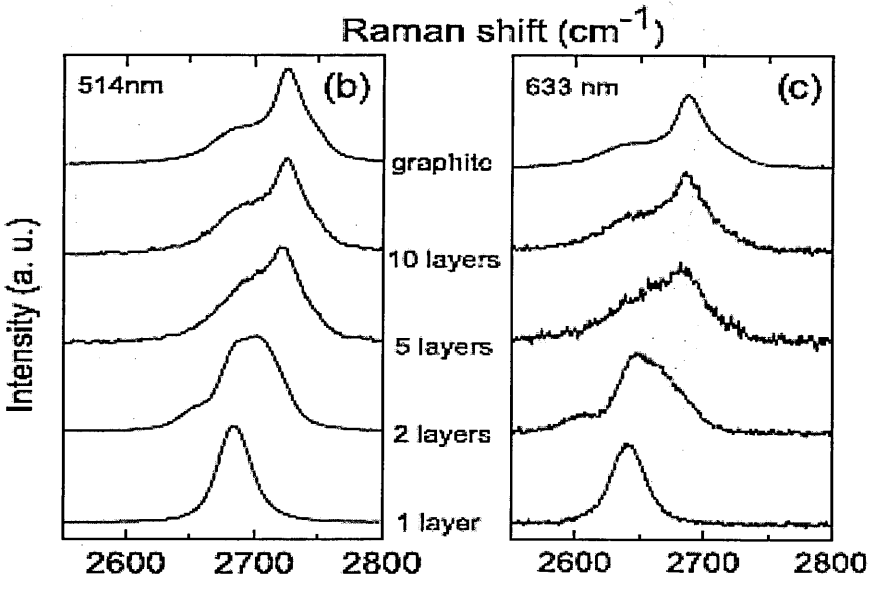

***Figure 3.8**: Evolution of 2D peak for grapheme at two different laser wavelengths. Note the dispersion effect in the profiles due to different excitation wavelengths [128].*

Raman 2D mode is also observed in graphite and CNTs as a second order Raman scattering effect[129]. However instead of one sharp peak in graphene, the graphite's 2D peak consists of two components $2D_1$ and $2D_2$ [128-129].

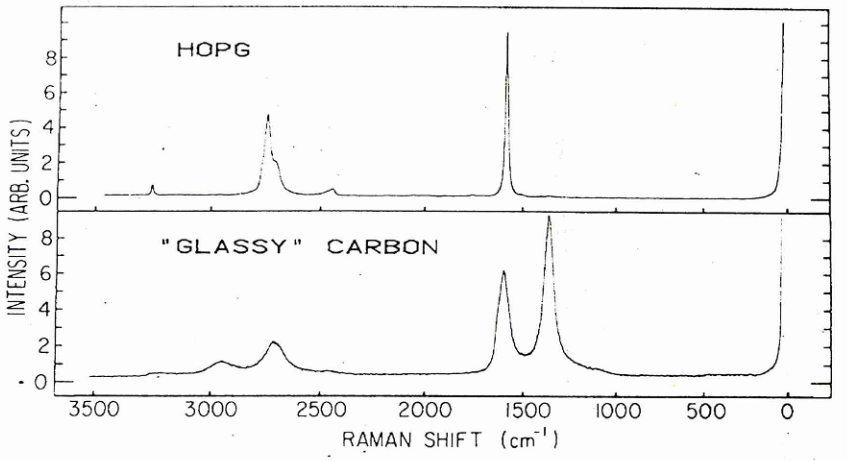

***Figure 3.9**: First and second order Raman spectra of HOPG and glassy carbon [129].*

The presence of excess charges (doping) on the graphene will also result in variation of the various peaks' position and intensity under Raman spectroscopy. Excess charges maybe caused by process residuals, leftover resist, adsorbates and substrate interactions [130]. Variation of the 2D/G ratio can vary from 5 times (for low doping) to just 1 for high doping despite having the same layer count [131]. Edge effects of graphene also contribute significantly to the Raman spectrum of graphene in general.

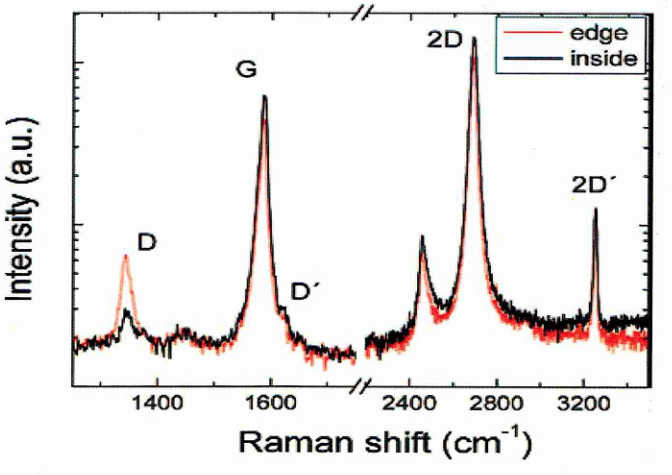

***Figure 3.10**: Graphene's edge effects on Raman spectrum at 514 nm. Note the visible D mode at the graphene's edge which would be absent at the centre [127].*

The above figure shows that D is more significant at the edge of a graphene layer. Furthermore at the edge, the D band's intensity is strongly influenced by the angle

between excitation laser's incident polarization and the edge, maximum at parallel and minimum at perpendicular. As a side note in the figure above at 2460 cm^{-1}, the Raman peak is $G+A_{2u}$, while 1450 cm^{-1} is due to silicon substrate [132].

One of the reported differences between Raman spectrum obtained from few layer graphene obtained via exfoliated method and CVD grown graphene is that the Raman 2D peak of some of the CVD grown few layer graphene exhibits a single Lorentzian peak but with a wider FWHM (up to ~ 70 cm^{-1}). In contrast, reported Raman 2D peak can be fitted with four Lorentzian curves for exfoliated bilayer graphene [104]. This may implies that CVD grown few-layers graphene may exhibit characteristics similar to turbostratic graphene resulting from the absence of long term order in the c axis as compared to HOPG's ordered AB stacking.

3.4 Transmission Electron Microscopy

A transmission electron Microscope (TEM) is a microscope that uses electron beam to illuminate a sample/speciman of interest instead of an optical light source. It primarily composed of an electron source, several condenser/objective/projector lenses and detectors. Simplified schematic of the TEM is shown in Figure 3.11. Unlike the more commonly found scanning electron microscope (SEM) which analyses signals reflected from specimens through secondary and backscattered electrons, TEM analyses electrons transmitted through the specimen, such as diffracted electrons. This also meant TEM can provide electron diffraction (ED) patterns of the speciman's lattice structure.

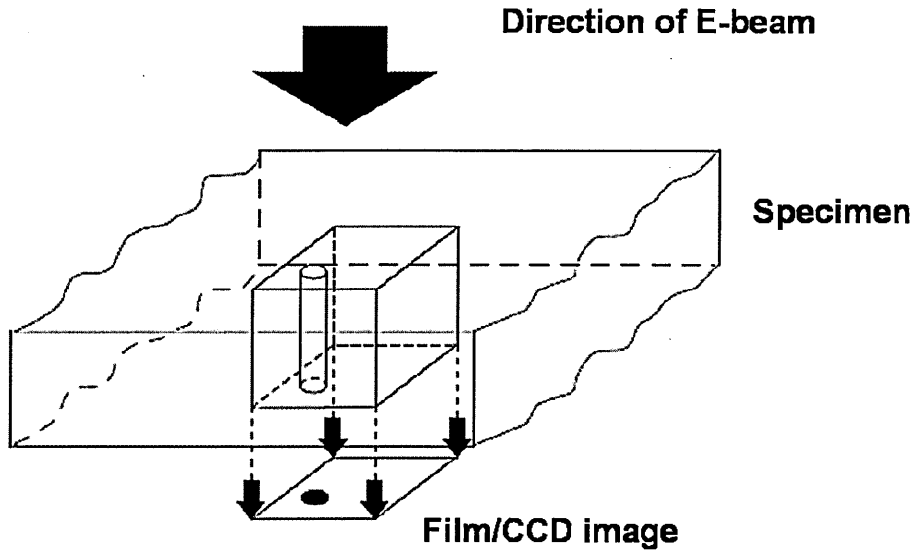

Figure 3.11: *Schematic showing the idea of TEM. An electron beam illuminates from the top of a specimen, travels through it and the image (formed from the electron exiting the sample) is subsequently collected on a film/CCD below the sample [7].*

From the schematic one salient point to note is that the thickness of specimens has to be very small in order to obtain a good signal and clear images. Another important difference is that the acceleration energy of electron gun is much higher (~ 200 kV) than that of a SEM, this resulted in an increased in spatial resolution.

Given that the most notable characteristic of TEM is its high resolution. This parameter is very attractive given that the tool can provide a visual image of nanometer size sample. Thus TEM naturally becomes a key analysis technique for identifying information on the carbon nano-material grown throughout this work. For example, TEM can provide information like the crystalline structure of CNTs, number of walls or layers of CNT or graphene, and CNT diameters. The trade-off is that the observation area is limited to a very tiny area of the specimen, typically a few tens to a few hundreds of nm area. Thus the information obtained by TEM for a specimen is localized. In this project, there is a choice of either using the Philips CM200 or Hitachi HD2300.

3.5 Thermal evaporation

In this thesis, the metallic electrodes and organic materials for the various electronic devices studied are fabricated using evaporation technique through a shadow mask. Deposition was performed in a modified Edwards multi-crucible evaporator (shown below) or using a in-house customised thermal evaporator, both at a base pressure less than 4×10^{-6} mbar.

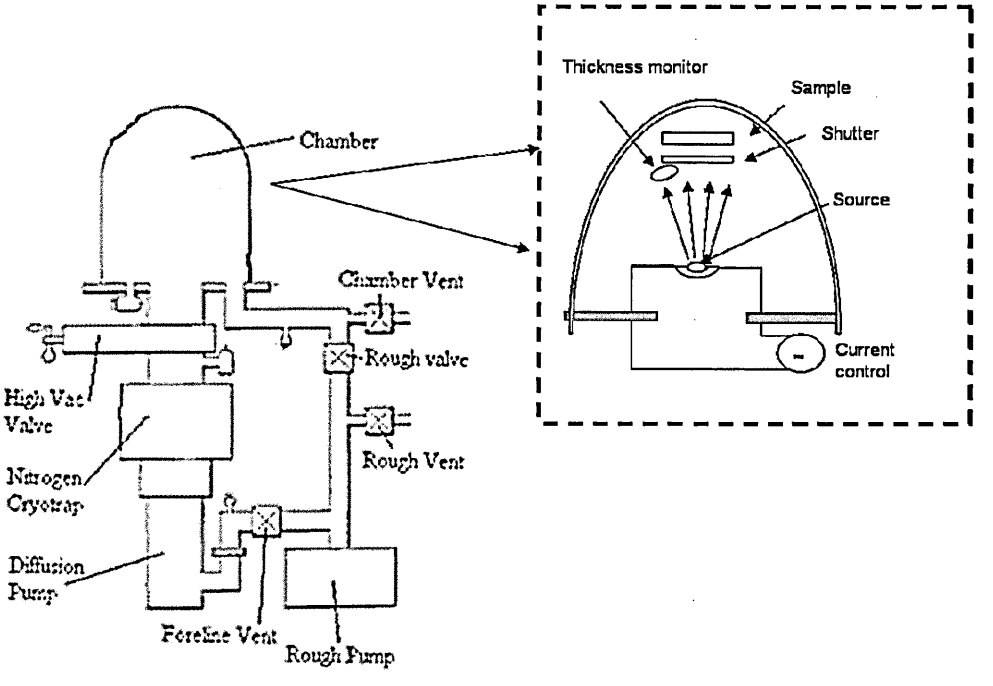

Figure 3.12: *Schematic diagrams of the modified Edwards thermal evaporation system.*

To measure the thickness of evaporated thin films accurately, a quartz crystal microbalance (QCM) is used. The tooling factor of the monitor was calculated and adjusted in order to minimize the thickness difference between the thickness measured by the quartz sensor and the actual thickness deposited on the substrate. The correct Tooling Factor is calculated by

$$\text{Tooling Factor} = Tooling_{APPROX} \times \frac{Thickness_{ACTUAL}}{Thickness_{QCM}}$$

The tooling factor for films was found by using a shadow mask to cover part of the metal film during the evaporation. The thickness of the film was verified by measuring the thickness of evaporated films using AFM or a Dektak IIA profilometer and compared with the thickness measured by the QCM to calculate the Tooling Factor.

3.6 Conclusion

In this chapter, the CVD growth tools which are used for the experimental works reported in this thesis are examined. One CVD distinct tool - Surrey NanoSystem uses IR heating for fast delivery of thermal energy that allows the prospect of implementing a fast growth process. Two popular analytical techniques TEM and (resonance) Raman spectroscopy are discussed. The Raman method is especially examined in details given the fact that the Raman technique provides a fast and non-destructive method for examining the quality of the as grown carbon microstructures.

CHAPTER 4

Low temperature growth of Carbon Nanotubes

From the literature review, one can find a wide variety of growth processes for CNT growth. From the view point of technology integration with the current CMOS roadmap, there still exists a need for low temperature, high growth rate CNT processes. In this section, a low-temperature growth of vertically aligned carbon nanotubes (CNTs) with high growth rates is investigated using the photo-thermal chemical vapour deposition (PT-CVD) technique with a Ti/Fe bilayer film as the catalyst. The bulk growth temperature of the substrate is as low as 370°C and the growth rate is up to 1.3 μm/min. This is about eight times faster than the values reported using the traditional thermal CVD methods. The as-grown CNTs were observed to be made of highly crystalline 5–6 graphene shells with an approximately 10 nm outer diameter and a 5–6 nm inner diameter. The low-temperature rapid growth of CNTs is likely due to a combination of the top-down heating mode of PT-CVD and the use of a Ti/Fe bimetallic solid solution catalyst.

4.1 Introduction

High temperature is generally thought to be a requirement for growing CNT with minimum or no defects [133]. Among the possible reasons believed to prevent low temperature CNT growth is that catalysts cannot be restructured and activated under these conditions. Another reason is that the reactive species cannot be dissociated and reacted with catalysts at such low substrate temperatures based on a traditional bottom-up heating approach. In additional, the traditional understanding of CNT growth mechanism model did not explain satisfactory the circumstances that can lead to a low temperature CNT growth process.

This is illustrated in the bulk volume diffusion growth proposed by Baker et al. [32] which describes temperature and concentration gradients driving the carbon diffusion through the volume of the catalysts. In comparison, recent studies indicated that diffusion of carbon over the surface of the catalysts requires a lower energy, well within the lower CNT growth temperatures reported [36-37]. It is possible that both processes can co-exist, depending on a number of factors, like methods of delivering energy (plasma at different frequencies, thermal or combination of these) to the catalysts which in turn is affected by the particular choice of CVD processes. The size of the catalysts or the use of alloyed catalysts, known to have lower melting temperature, also affects the growth temperature.

There is however a desire to drive towards a lower temperature CNT growth process. One of the impetuses comes from the ITRS roadmap. CNT, with its good electronic charge transport property, has been proposed as a possible replacement for Cu interconnects in nanoelectronics, as Cu nanoscale wirings fail to meet the predicted current density demands imposed in large scale integration circuits of the future [134-135]. However, present CMOS devices are fabricated with back-end-of-line processes at temperatures below 400°C, which is a challenge for growing high-quality CNTs by chemical vapour deposition (CVD).

To date, several routes have been attempted to lower the CNT growth temperature: -

1) Using various carbon feedstocks with lower dissociation temperature and high reaction activity with catalysts [136];

2) Controlling the hydrocarbon concentration in the system. Considering that with more carbon arriving at the surface of the catalysts, a faster thermodynamically driven diffusion rate will be needed to prevent suppress any amorphous growth that may compete with CNT formation. This is confirmed by the observation that increasing

hydrocarbon feedstock while keeping other factors unchanged led to more amorphous carbon quantity [137]. However, this also implies a slower growth rate;

3) Exploring a wide range of catalysts, such as bimetallic nanoparticles and oxide with low melting points [24, 134, 138];

4) Use of a small flow rate of undiluted hydrocarbon feedstock which translate to a low growth processing pressure ($< 10^{-2}$ mbar) [139], which is much lower than our reported operating pressure of 2 Torr (see paragraph on experiments in this section).

5) Introducing plasma energy (DC, RF, Microwave) during deposition with the scope of increasing the dissociation and ionization of feed gases and concomitantly decreasing the activation energy of the CNT growth [111, 140]. However, plasma based methods tend to introduce structural defects in CNTs due to ion bombardment, leading to the formation of lower-quality carbon nanofibers [137]. Furthermore, it is also reported that plasma methods do not favour the growth of both high-quality single-wall CNTs and ultralong multi-wall CNTs, perhaps due to plasma poisoning of catalysts and etching of CNTs [141];

6) Gas phase preheating or catalyst pre-treatment (e.g. use of NH_3) while still using the traditional thermal CVD methods [139, 142]. However, the present growth rate of CNTs by thermal CVD is quite low and insufficient for practical applications of CNTs, The use a highly toxic gas like NH_3 also meant a need for greater safety precautions.

Beyond the above mentioned methods, another novel concept is through the use of a layer beneath the catalysts which can act as a thermal barrier. This concept is illustrated in the following diagram (Figure 4.1). Chen et al. [111] reported that a low temperature CNT growth ($< 400^{\circ}C$) using a similar thin-film structure with DC plasma (500V) as the only thermal energy delivered in the PECVD. Ti was chosen as it has a low thermal

conductivity among metals and also the use of DC plasma restricted the choice on insulating materials.

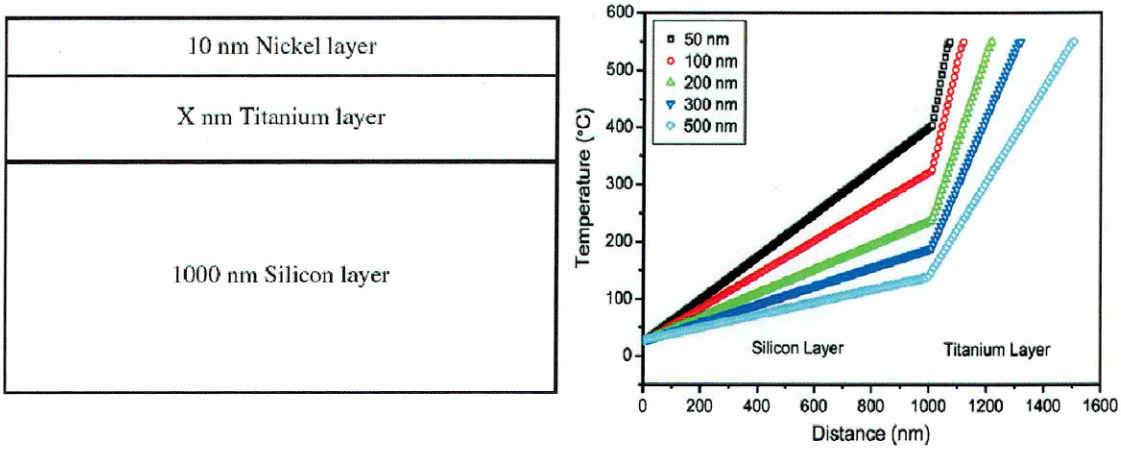

Figure 4.1: *(Left) Ni is intended to be the catalysts for CNT growth while Ti (variable thickness x) acts as the thermal barrier. As seen on (Right), simulation of the thermal profile in the structure shows a much higher temperature at the Ti layer compared to its underlying Si substrate [111].*

Tuning the thickness of the thermal barrier layer led to a significantly different thermal profile in the structure. As a consequence of the above design, it was possible for the underlying Si substrate to remain much cooler, thus for processes like CMOS fabrication which demands a low processing temperature, such a structural design would be advantageous. Based on the above insights, the PT-CVD would be the next natural technological progression. Through the use of an IR optical source in place of a DC plasma for top down energy delivery would remove some of the earlier mentioned concerns like CNT structural damages due to ion bombardment by plasma, and a greater materials choice [143].

This section documents the low-temperature rapid growth of vertically aligned CNTs by the photo-thermal CVD (PT-CVD) method using a highly active Ti/Fe alloy catalyst. The structure of as-grown CNTs is studied by using scanning electron microscopy (SEM), transmission electron microscopy (TEM) and Raman scattering. The rapid growth mechanism of CNTs is discussed briefly.

4.2 Experiments

The catalyst consisted of 1 nm Fe and 0.5 nm Ti that was sequentially deposited on 50 nm SiO_2 by Ar magnetron sputtering. CNT growth was performed using the Surrey NanoSystem's photothermal CVD (PT-CVD) as discussed previously in Chapter 3. The sample was loaded into the growth chamber under ambient atmosphere. After pumping down to its base pressure, a mixture gas of 100 sccm H_2 and 6 sccm C_2H_2 was introduced into the chamber at a working pressure of 2 Torr. Previously reported work indicated that amorphous carbon content becomes significant when hydrocarbon concentration exceeds 6% [110-111]. The IR lamp array was switched on immediately to start the CNT growth for 15 min. The substrate temperate was continuously monitored by an optical pyrometer embedded in the sample holder, and a thermocouple located on the surface of the substrates. After deposition, the lamp array was switched off and the sample was cooled in the ambient of H_2.

4.3 Results and discussion

Figure 4.1(a) and (b) show a top-view and cross-sectional SEM images of the CNT sample grown at the substrate temperature of about 370°C. The surface is uneven with the appearance of some cross protruding lines, which are not horizontal CNTs bundles but the tips of vertically aligned CNTs due to different CNT heights as confirmed by higher magnification SEM inspections (Fig. 4.1b and c). The CNT growth in our PT-CVD seems to follow a tip growth model [37] and the growth temperature is relatively low as no surface melting induced flattening of the metal catalysts appears to occur on the substrate. The length of CNTs is ~ 20 μm and the growth rate is estimated as 1.3 μm/min. This value is about 8–25 times larger than that of traditional thermal CVD (0.05–0.16 μm/min) at the substrate temperature range of 350–475°C [139, 142].

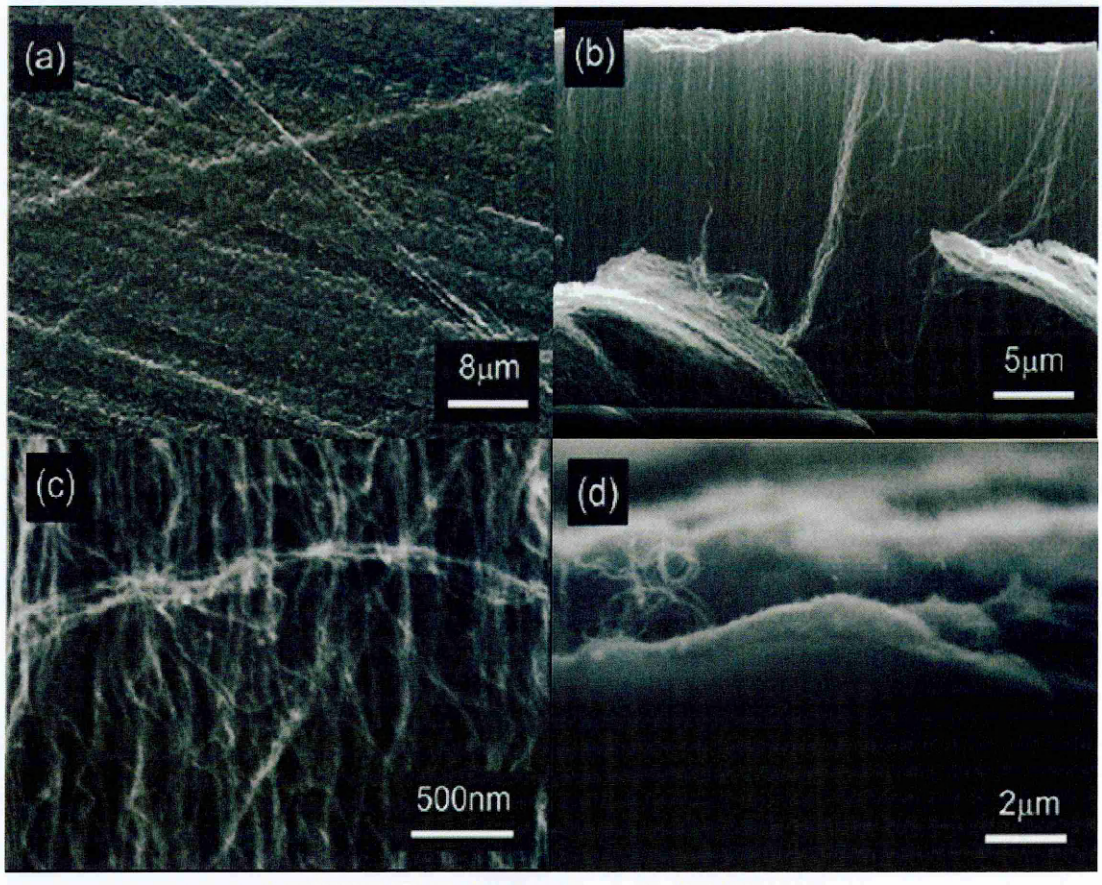

Figure 4.1: *Top-view (a) and cross-sectional (b) SEM images of vertically aligned CNTs; (c) is the magnified SEM of (b) and (d) back-scattering electron image*

The as-grown CNTs via PT-CVD are in the form of a forest with vertically aligned bundles with respect to the substrate. They are clean with no carbon particles and residual catalysts found among the CNT forest as shown in Fig. 4.1c. This was further confirmed by scanning back-scattering electron imaging technique, which is more sensitive to heavy metal catalysts than to the lighter element carbon [144]. The few bright spots related to the metal catalysts are found in the back-scattered electron image on both the tip and side areas of CNTs. This reveals the catalysts are tiny and uniform, implying the catalysts may have retained high activity during the growth process.

Figure 4.2(a) shows a TEM image of the sample, which is prepared by ultra-sonicating in methanol and then sieved onto a holey carbon grid. The sample is very clean and contains few contaminant particles. It only consists of tangled long CNTs with uniform diameter. The electron diffraction pattern in the inset is matched well with that of

polycrystalline hexagonal graphite, revealing that the as-grown CNTs are highly graphitized.

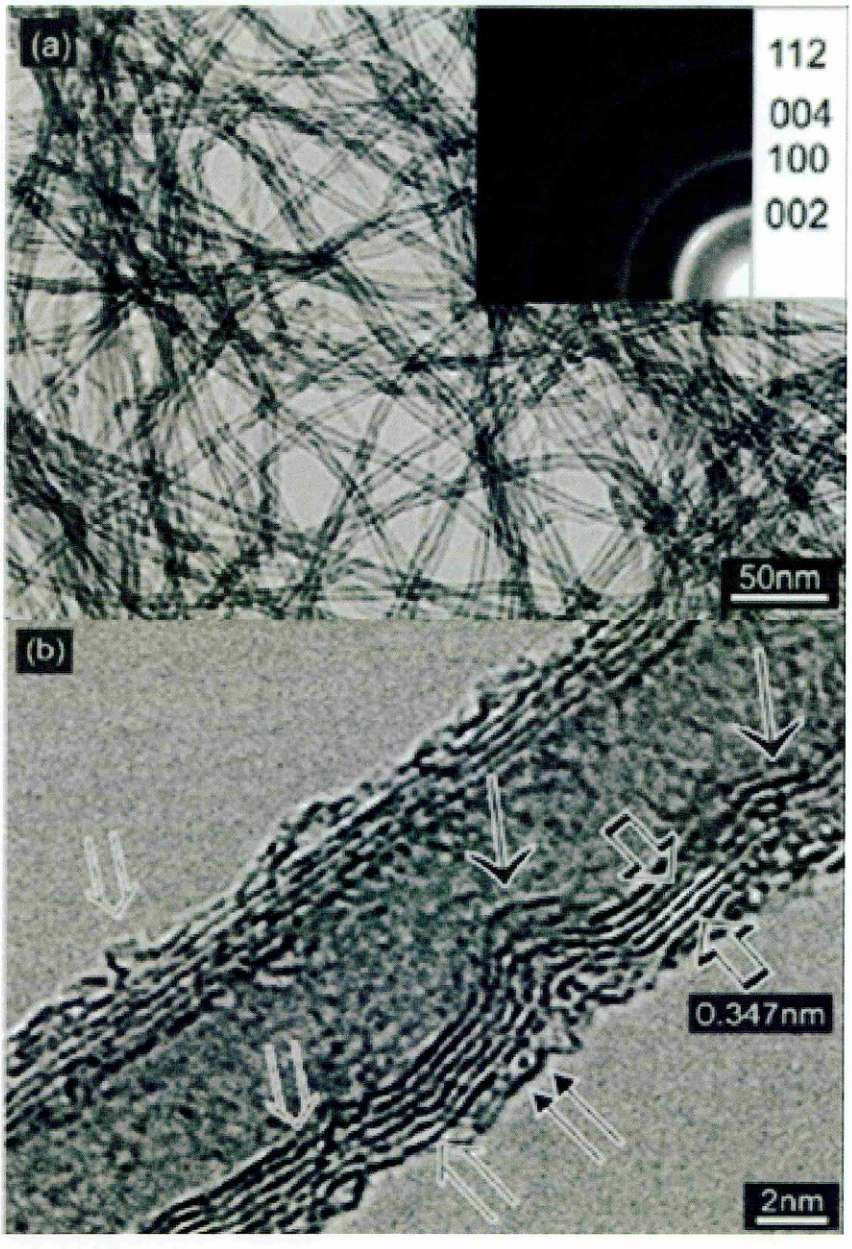

Figure 4.2: *(a) and (b) Low-magnification and high-resolution TEM images of CNTs. (Inset) is the electron diffraction pattern*

Figure 4.2(b) is a typical high resolution TEM image of an as-grown CNT. The CNT has a 5−6 nm hollow interior and about 10 nm outside diameter. It is clearly made of 5−6 graphene shells, which have a typical graphite (0002) spacing of 0.347 nm. The constituent graphene layer is essentially crystalline but contains various structural

defects, which are similar to those of found in CNTs growth by other methods at low temperatures [134, 142]. For example, there are some broken graphene layers, forming some steps and kinks along both the inner and outer walls of CNTs (pointed out by a double-line arrow). There are also some rippled graphene layers formed in the inner side of CNT walls (identified by an arrow) because the stress in the wall cannot be released at low temperatures. These structural defects destroy the periodicity of graphene shells and make both the inner and outer walls defective and rougher compared to high-temperature grown or annealed CNTs, whose walls are commonly made of clean, straight, ordered, and highly crystalline graphene layers [145].

Figure 4.3(a) shows the Raman spectra at room temperature excited by multiple wavelength lasers of 2.81eV (442 nm), 2.41eV (514 nm), 1.96eV (633 nm), and 1.58 eV (782 nm) in the range of 500–3000 cm^{-1}. Their profiles are very similar as those of CNTs grown by both thermal and plasma enhanced CVD at substrate temperatures of 400–550°C [144, 146]. The spectra mainly consist of: Raman D band at 1307 – 1358 cm^{-1}, Raman G band at 1571 – 1594 cm^{-1} and a Raman 2D band at 2597 – 2717 cm^{-1}, and finally a possibly D' shoulder at 1600–1620 cm^{-1}.

The intensity of D band increased with the excitation energy, while the intensity of 2D (or G') band decreased. Due to the double resonance effect [147], the frequencies of both D and 2D bands are up-shifted with the excitation energy shown in Fig. 4.3(b). They have an energy dispersive coefficient of 40.7 and 98.2 cm^{-1}/eV, respectively, both smaller than the majority of reported values on graphite and single-wall CNTs. In terms of the nature of the D band from the structural defects in graphene based materials, the ratio (I_D/I_G) of integrated intensities of the D to G bands usually has been considered as a fingerprint for the evaluation of the crystal quality of graphene based materials.

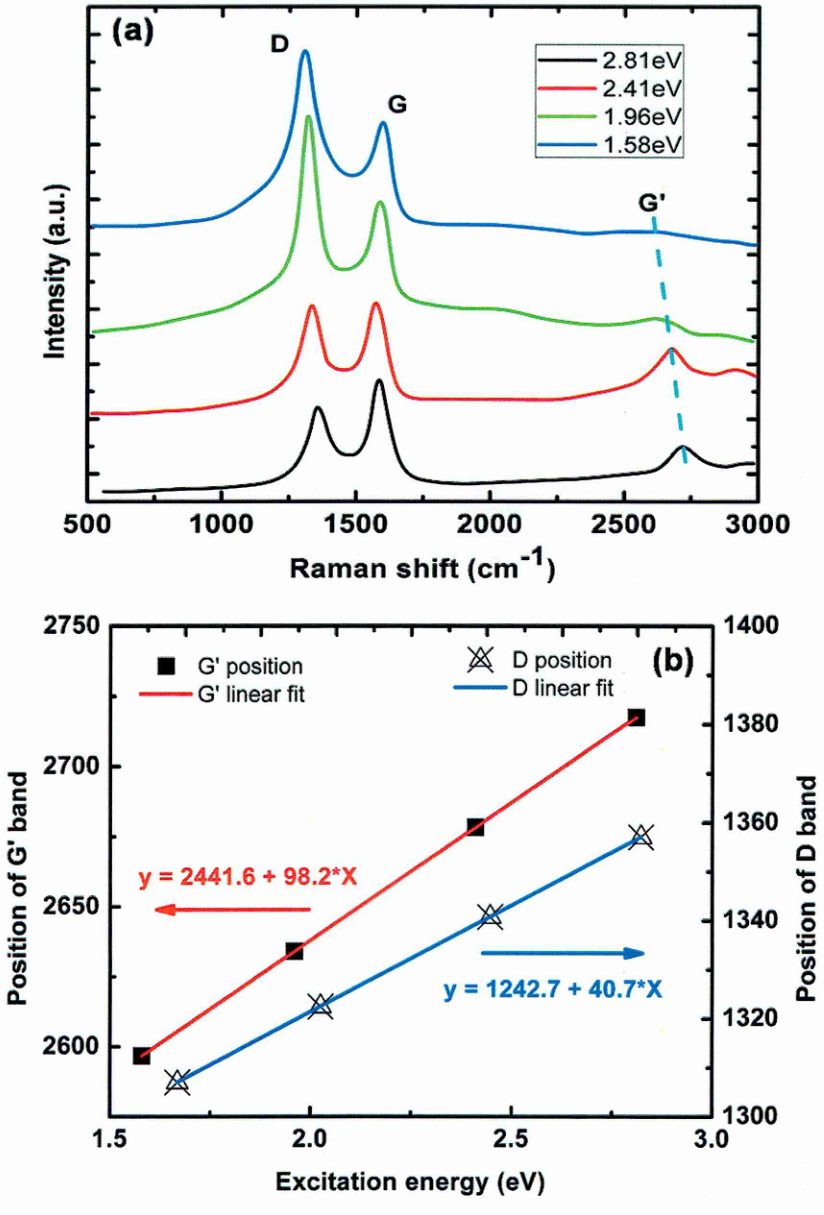

Figure 4.3 *(a) Raman spectra of CNTs with excitation by various wavelength lasers and (b) the energy dispersion of peak positions of D and 2D or G' bands*

The I_D/I_G ratios of D to G bands for four kinds of laser excitations of 442, 514, 633 and 782 nm are 0.8, 1.3, 2.0 and 3.0−6.5, respectively. The ratio increased with the excitation energy, a trend also observed in other graphitic materials [148-149]. A broad peak related to amorphous carbon at about 1500 cm^{-1} is observed to have been activated by the 782 nm laser and thus significantly influences the intensity of the G band. Thus, to accurately evaluate graphene based materials, the comparison of both the D band

intensity and the D to G band ratio for different samples should be based on identical laser excitation. Here, the ratio (I_D/I_G = 1.3) for the 514 nm excitation from the samples is less than that (I_D/I_G = 3.4) of CNTs deposited by radio frequency plasma CVD at a substrate temperature of 500 °C [146], and less than that (I_D/I_G = 2.1–2.6) of CNTs grown by thermal CVD at the substrate temperature of 400–550°C [144]. This shows that the CNTs grown by PT-CVD are of higher quality with only some structural defects.

Similar to hot filament CVD[150], PT-CVD is a top-down method. It has the advantages of directly transferring thermal energy to the catalyst, heating only the substrate surface, while preventing possible impurities from due to filament poisoning which is presented in hot filament CVD. Different from traditional furnace based thermal CVD, PT-CVD offers a fast heating mode to the required temperature within seconds, enables the catalytic metal film to be nanostructured by preventing metals from been alloyed, diffused, coarsened and so on. In this study, PT-CVD is purely a thermal process without the interference of plasmas. This precludes the negative effects of ion-bombardment induced poisoning of catalysts and etching of CNTs, which commonly occurs in plasma based CVD.

Theoretical calculations and experimental studies have reported that dual metal catalysts have higher activities compared to single metals. One of the dual metals could enhance the nucleation of CNTs and the other could essentially increase the CNT growth[151]. They usually have a lower melting point and specifically benefit low-temperature growth of CNTs by lowering the activation energy due to the 'synergistic effects' of the bimetals [138]. Fe/Ti binary catalysts have been used to catalytically grow CNTs. However, they demonstrate different activities for the CNT growth, which are critically dependant on the deposition method [151-152]. In the traditional thermal CVD, Fe/Ti catalysts are completely inactive because Ti has a high solubility in Fe leading to the formation of a large particle. In contrast, Fe/Ti can catalytically grow

mm-long CNTs by grid-inserted plasma CVD. It is worth noting that at the substrate temperature of 400°C, the growth rate is only around 0.1 μm/min, 13 times smaller than values recorded in this study. Here, in the PT-CVD system, Fe/Ti bilayer thin films absorb incident light-energy, inter-diffuse and rapidly form a solid solution, which can be evidenced by annealing the sample in a H_2 ambient.

Figure 4.4 shows AFM topographic images of an as-sputtered Fe/Ti bilayer film and that H_2 annealed film at 370 °C for 3 min, which have a roughness of 0.71±0.16 nm and 0.49±0.09 nm, respectively.

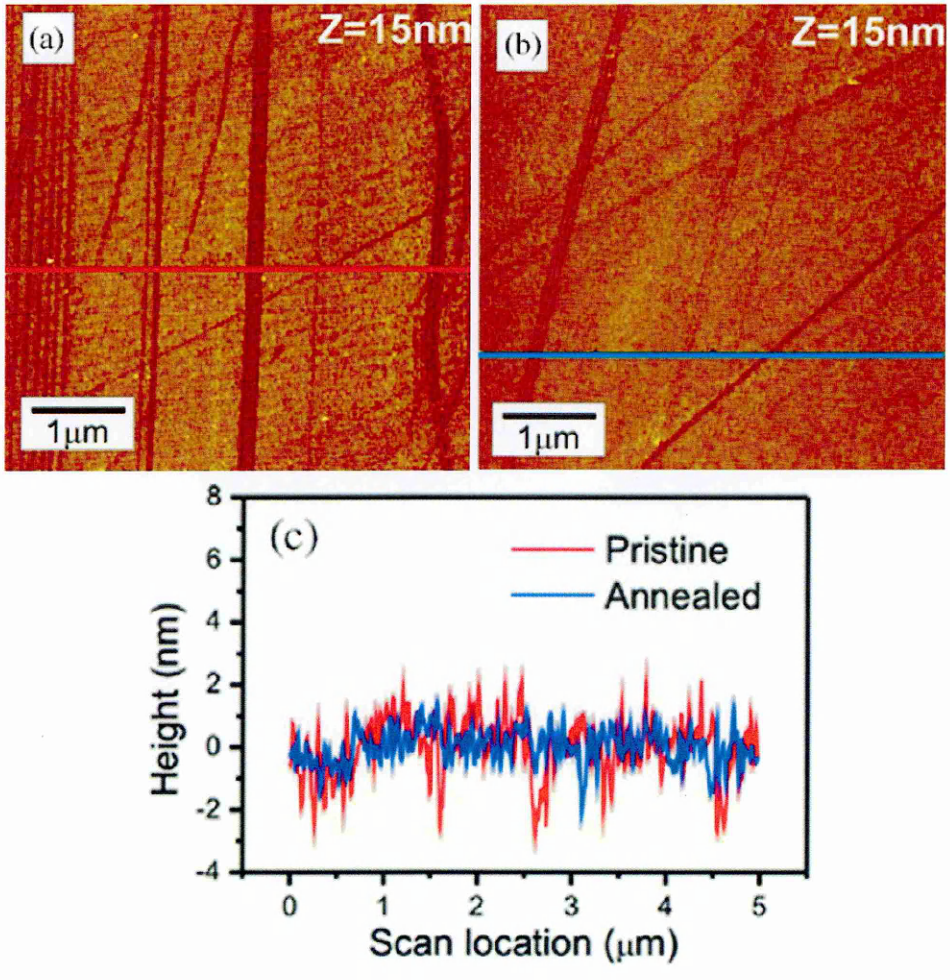

***Figure 4.4**: (a) and (b): shows AFM topographic images of an as-sputtered Fe/Ti bilayer film and that H_2 annealed film at 370 °C for 3 min; (c) comparison of the line scan profiles taken from red and blue lines in the images contrasting the surface roughness before and after annealing*

Different from traditional thermal CVD, the annealed sample is smoother than the pristine one. This indicates that the sputtered nanoclusters in the Fe and Ti film migrate, mix and ripen, resulting in a "solid solution", which is made of uniformly, dense and fine Fe/Ti nanocatalysts rather than isolated large nanoparticles formed by traditional bottom-up heating [139]. This ensures that the CNTs catalytically grow via a solid surface reaction with C_2H_2 [110]. The high density of nanocatalysts and the high CNT yield result in their vertical alignment, possibly aided by Van der Waals interactions of adjacent CNTs with each other. Another possible mechanism of rapid CNT growth is ascribed to the formation of a ternary solid solution of highly active Ti-Fe-O particles due to catalyst exposure in air for a longer time period and without a H_2 pre-reduction process [153]. Details of the rapid low-temperature growth mechanism of CNTs are less clear.

4.4 Conclusion

Vertically aligned CNT forests have been grown at 370 °C by a one-step PT-CVD method. The growth rate is as high as 1.3 μm/min, at least 8 times faster than most other thermal CVD methods. The CNTs are composed of a few layer crystalline graphene sheets with a 5–6 nm diameter hollow interior with some structural defects ascribed to the low growth temperature. Raman scattering provides supporting evidence that the as-grown CNTs are can have quality that is comparable or better than some of the reported CNTs grown at higher temperatures by traditional CVD methods. AFM topography studies confirm the fast top-down heating mode of the PT-CVD leads to the formation of a Fe/Ti uniform solid solution, which greatly improves the CNT growth. The PT-CVD growth method of CNTs at low temperatures offers the potential for exploiting the integration of high-quality CNTs into CMOS devices.

CHAPTER 5

Growth of graphene using thermal CVD and its field effect properties on different dielectrics

In this chapter, investigations into another sp^2 carbon material – graphene – using CVD techniques are being reported. Efforts are made into tuning a growth process for graphene using metal catalysts in a standard thermal CVD system. The charge transport properties of the as-grown graphene were investigated at room temperature using a field effect transistor fabricated on a standard silicon dioxide dielectric with Si support (which can act as a back-gate). Subsequently, a graphene based FET incorporating poly-4-vinyl-phenol (PVP), a well known organic insulating layer, as an alternative to conventional oxide gate dielectric materials was investigated in this section.

5.1 Introduction

One area of great interest in the field of organic electronics is the organic transistor (oFET or oTFT) design and performance [154-155]. In terms of charge mobility in oFET, the introduction of good crystalline organic semiconductors [154] like pentacene and rubene has led to improvements in performance. Other new preparation techniques for gate dielectric materials, for example altering the properties of Poly(4-vinylphenol) [156] by cross-linking Poly(4-vinylphenol) through esterification reactions with commercially available bifunctional anhydrides, acyl chlorides, and carboxylic acids also helped in the performance of oTFT. Some measured mobilities (Pentacene, FCuPc, 5,5′-bis-(7-dodecyl-9H-fluoren-2-yl)-2,2′-bithiophene (DDFTTF) as the organic semiconductors) of as high as 3 cm^2/Vs has been reported [156]. Given the attractive charge mobility of graphene, it presents an opportunity as an alternative material worthy of exploration in this field.

As single layer graphene does not possess a bandgap, both electron and hole conduction are readily possible and the electrical characteristics of graphene are often described in terms of a V-shaped characteristic of current (conductivity) with gate voltage. The presence of adsorbed species, which act as doping and/or scattering centres, may result in a rigid shift and rounding of the characteristic at low carrier densities [59]. Indeed there is currently considerable research being undertaken into how the associated processing and patterning of graphene devices may adversely affect the electrical properties. However, the room temperature mobility of graphene, even after processing, is higher than that found in organic electronic materials and opens up the possibility of large area organic electronics.

From a technological point of view, being able to produce the active layer in a roll-to-roll process is highly attractive and as such reports on graphene that produced using chemical vapour deposition (CVD) on metal foils and roll-to-roll processing is a significant step in this regard [71, 106]. Already a 30 inch graphene layer with high optical transmission and low sheet resistance has been demonstrated using a roll to roll CVD growth based method [71]. With these technological goals in mind, the chapter reports the electrical characteristics of CVD single layer graphene grown on high purity copper foil and then transferred onto poly-4-vinyl-phenol (PVP), one of the more commonly investigated gate dielectrics in organic FETs because it exhibits good insulation with low leakage density and is suitable for low cost all-solution-processing and print fabrication process [157-158].

Instead of relying on the complicated and expensive e-beam lithograph, fabrication of a large channel length/width (L ~50 μm, W ~1000 μm) FET structure is chosen to demonstrate the ease and potential for mass fabrication. Furthermore the bottom contact electrode topology is chosen for this investigation into the PVP gate dielectric FET performance as this topology has been intensively investigated in organic FET research. Detailed reviews on the research progress on bottom electrode contacts (and in

comparison to the conventional top contacts) for organic FETs have been reported elsewhere [154, 158-159] and the references therein. This work demonstrates that an all organic transistor with graphene as the active layer is possible and opens up a competitor technology in the field of large area electronics.

5.2 Experiments

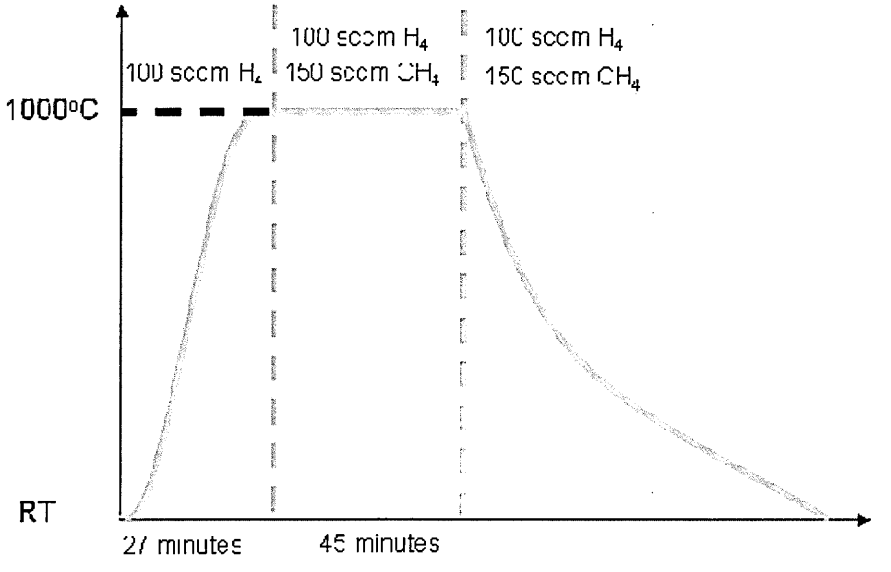

Figure 5.1: *Recipe for growth of graphene on Cu substrate*

Copper foils (> 99% purity, mechanically polished 25 μm or 50 μm thick) were cut into ~ 10 mm strips in length and cleaned in a standard three stage clean (acetone, 2-propanol and methanol). The foils were then placed in the centre of the quartz furnace (as mentioned in Chapter 3) and heated up to 1000°C under an atmosphere of H_2 (100 sccm flow rate) for 30 minutes. Methane (150 sccm) was then introduced for 45 minutes while the furnace remained at 1000°C and after a given time the system was cooled down to 300°C. Below 300°C the flow of methane was stopped and the sample was then cooled down to room temperature under He flow.

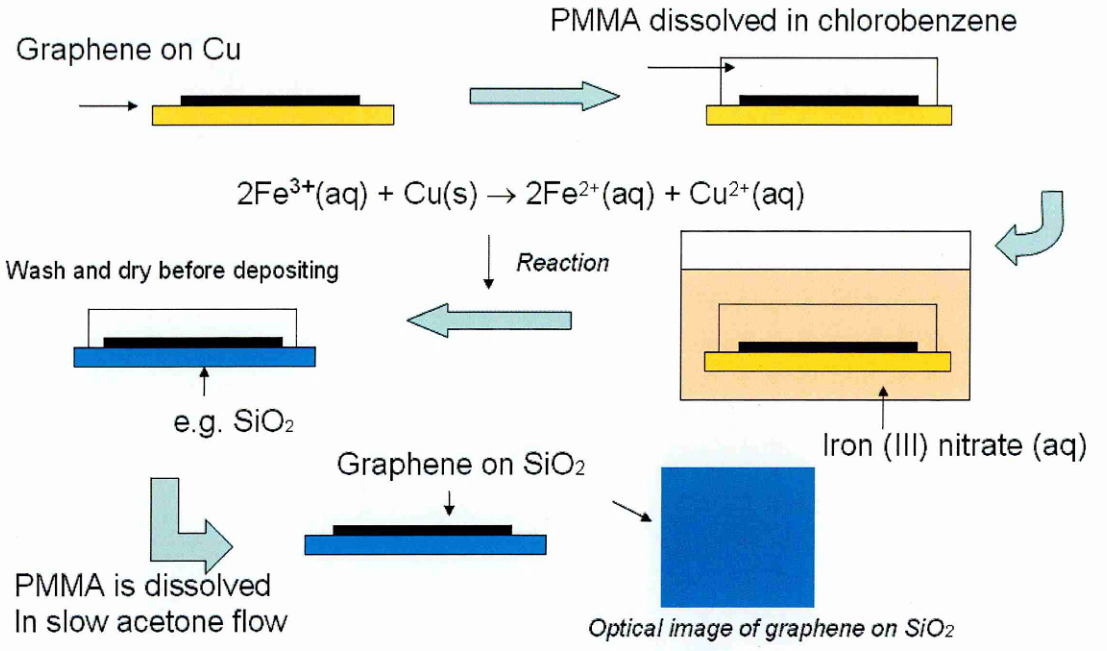

***Figure 5.2**: (Top) Process flow for transferring as grown graphene from the metal catalyst onto another substrate – in this case SiO_2 support for further processing and analysis. (Bottom) Graphene film floats on the water surface after the previous step of removing the metal substrate (indicated by the **circle** highlight). Note the arrows referred to water trapped underneath the glassware and reflections from surroundings.*

The graphene on Cu foil was subsequently transferred onto a SiO_2 (~300 nm thick) substrate using the PMMA transfer method as described elsewhere [10]. PMMA (Mw ~ 950K, 10% wt) dissolved in anisole or chlorobenzene, was spin-cast onto the

sample's surface and hardened by heating at 180°C for 2 minutes. The sample's Cu support was then removed using an iron nitrate solution. The graphene/PMMA was dried, cleaned and transferred onto a SiO_2 before dissolving the PMMA under a slow flow of acetone. Further annealing in He flow at 200°C was performed (30 min) and kept under vacuum till further use. The graphene was examined using optical microscope (Leica microscope) and Raman spectroscopy (Reinshaw microRaman at 514 nm).

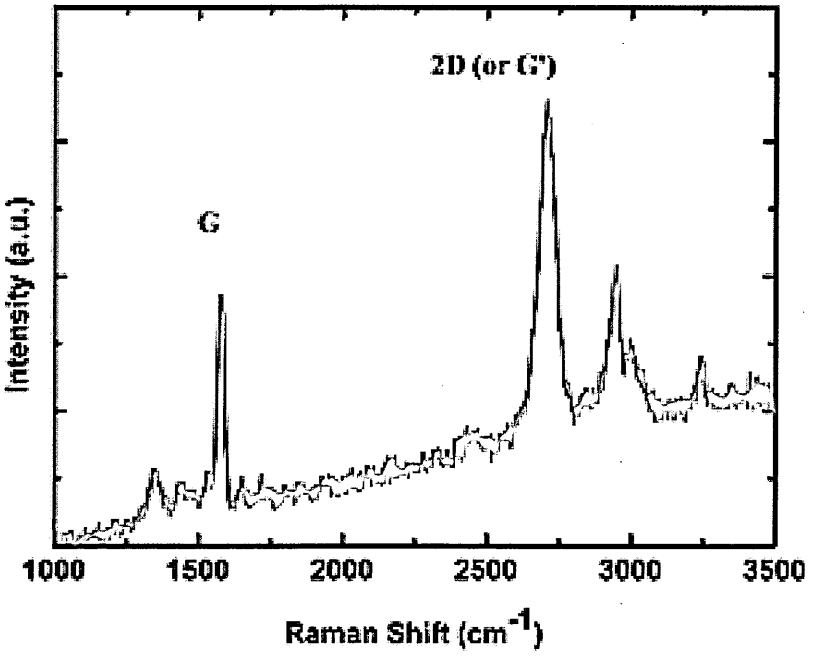

***Figure 5.3**: Raman spectrum of graphene with a layer of PMMA spun on it. Note that additional peaks after the Raman 2D and the higher background intensity compared to Raman spectra of graphene with PMMA removed (shown later).*

The Raman spectrum (Fig. 5.3) of a graphene layer with the PMMA on it has additional peaks beyond the Raman 2D peak as well as higher background fluorescence, thus this provides a convenient reference to check on the status of PMMA removal outcome.

For graphene based field effect transistor, the bottom contact Si back-gate graphene FET was produced by first evaporating Ag (100 nm thick) onto SiO_2 (300 nm thick) on silicon substrate as the source and drain electrodes (L ~50 μm, W ~ 1000 μm). Next, a

graphene film was transferred using the PMMA technique described previously. For the case of top contact topology, Ag was evaporated as the electrodes using a stainless steel shadow mask after graphene has been transferred onto the SiO_2. Electrical I-V measurements were performed using a combined Kiethley 2400 with 238 sourcemeter. The drain voltage was set at 500 mV while the gate voltage was being swept.

5.3 Results and discussion

Experimentally, the two different thickness of Cu did not produced observable difference in the Raman spectra when examined under the micro-Raman setup (Reinshaw micro-Raman). Two salient points were observed during the development of the CVD process that is in line with other reports [106, 160]. There is minimum time duration for CH_4 exposure to ensure complete coverage of graphene formation on Cu for low pressure based thermal CVD process, which 45 min in the thermal CVD system.

Furthermore during the cooling down phase, if CH_4 was switched off leaving only H_2 or He or a combination of two, there is no observable graphene formation as measured by Raman spectroscopy. This is different from Ni based graphene growth where absence of additional hydrocarbon source is important in the formation of graphene [103, 109]. This can be explained using the model proposed by Li and co-workers [108], where absorption and re-precipitation of carbon by Ni help led to the formation of graphene while graphene formation on Cu is a surface process, thus maintenance of a hydrocarbon gas flow is necessary.

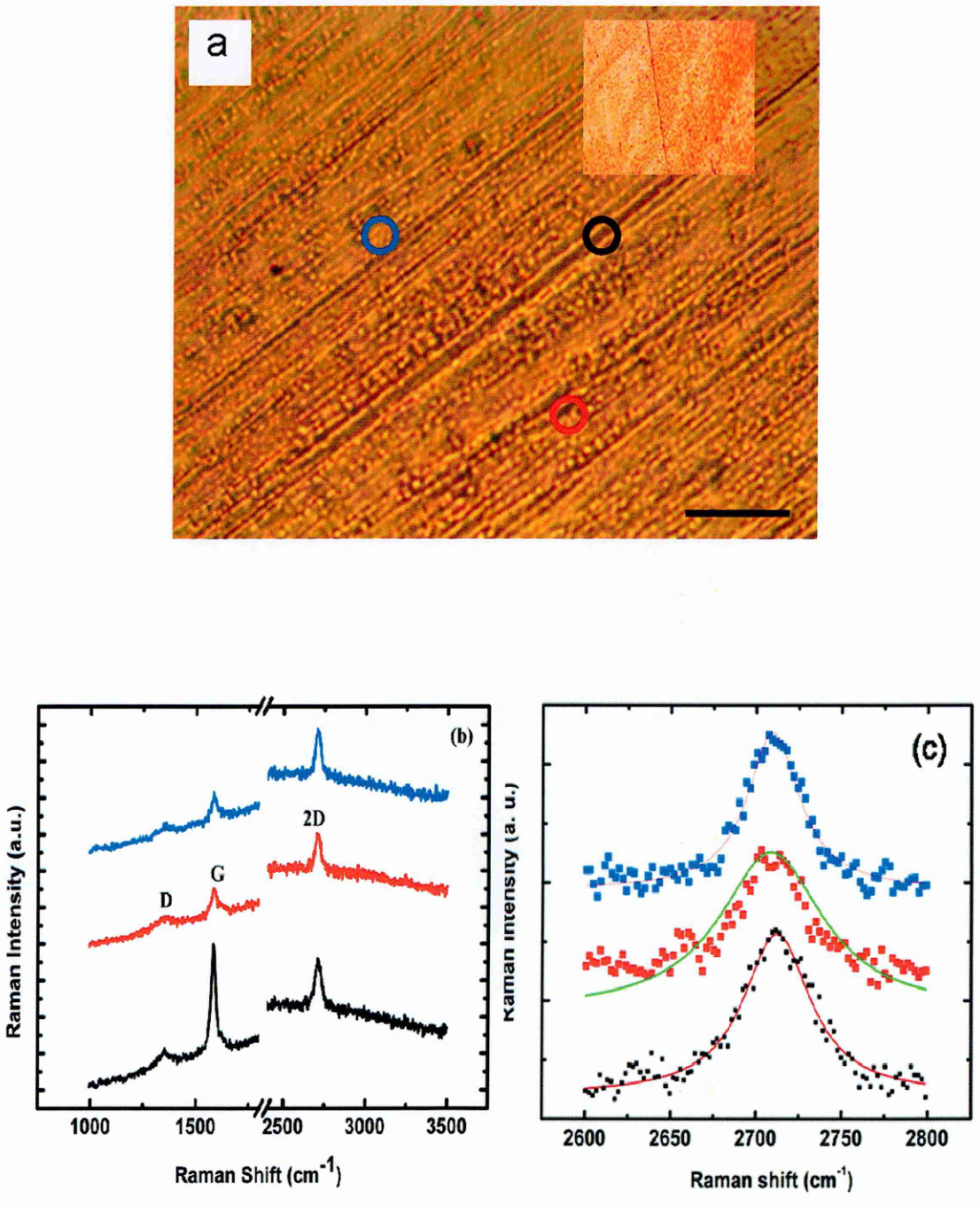

Figure 5.4: *(a) Optical image of graphene as grown on Cu, inset is image of Cu before processing. The foil is not optically flat and the different colour intensity is resultant of different illumination under microscope. The black bar is 50 μm. (b) Raman spectra of the G, D and 2D peaks at the three corresponding points on the optical image shown previously in figure 1a. (c) These Raman 2D peaks are examined in detail with their respective Lorentzian curve fittings. Blue circle ~ 2709 cm^{-1} FWHM ~ 37 cm^{-1}. Red circle ~ 2708 cm^{-1}, FWHM ~ 64 cm^{-1}. Black circle ~ 2712 cm^{-1} FWHM ~ 47 cm^{-1}.*

The optical image of the Cu foil before undergoing processing (Fig. 5.4(a), inset) displayed regular a structural pattern that indicated the effects of cold roll processing and polishing. After undergoing the graphene growth process, the surface of these Cu foils exhibited various dark streaks (Fig. 5.4(a)), the cause of which remains unclear. Raman spectroscopy was used to examine the as-grown graphene. Raman spectra (Fig. 5.4(b)) were taken from the three locations marked in Fig. 5.4a on the Cu foil showed the characteristic a single 2D peak at 2710 ± 1 cm^{-1}. The Raman spectra also showed a Raman D peak (~1367 cm^{-1}) and Raman G peak (1583 cm^{-1}), though these bands were accompanied by a large background signal at these Raman shifts. There was no observable correlation between the Raman spectra between the above mentioned dark patterns.

To examine the as-grown graphene using Raman spectroscopy against other published data, transferring of the film onto another substrate would be desirable. Furthermore, transferring the film onto other substrates would facilitate the ease of fabrication electronic devices like field effect transistors. Figure 5.5(a) shows the Raman spectra for the graphene on SiO_2 collected at the point indicated (inset), where both the Raman D (measured at 1348 cm^{-1}) and Raman G (1578 cm^{-1}) peaks can be seen. The 2D peak in Fig. 5.5(b) can be fitted to a single Lorentzian line shape centered at 2704 cm^{-1} and full width half maximum of 37 cm^{-1}, confirming the presence of single layer graphene after transfer [128]. Furthermore, given the relatively small Raman D peak observed on this sample, it seems that the transfer process did not result in severe damages or tearing of the graphene film.

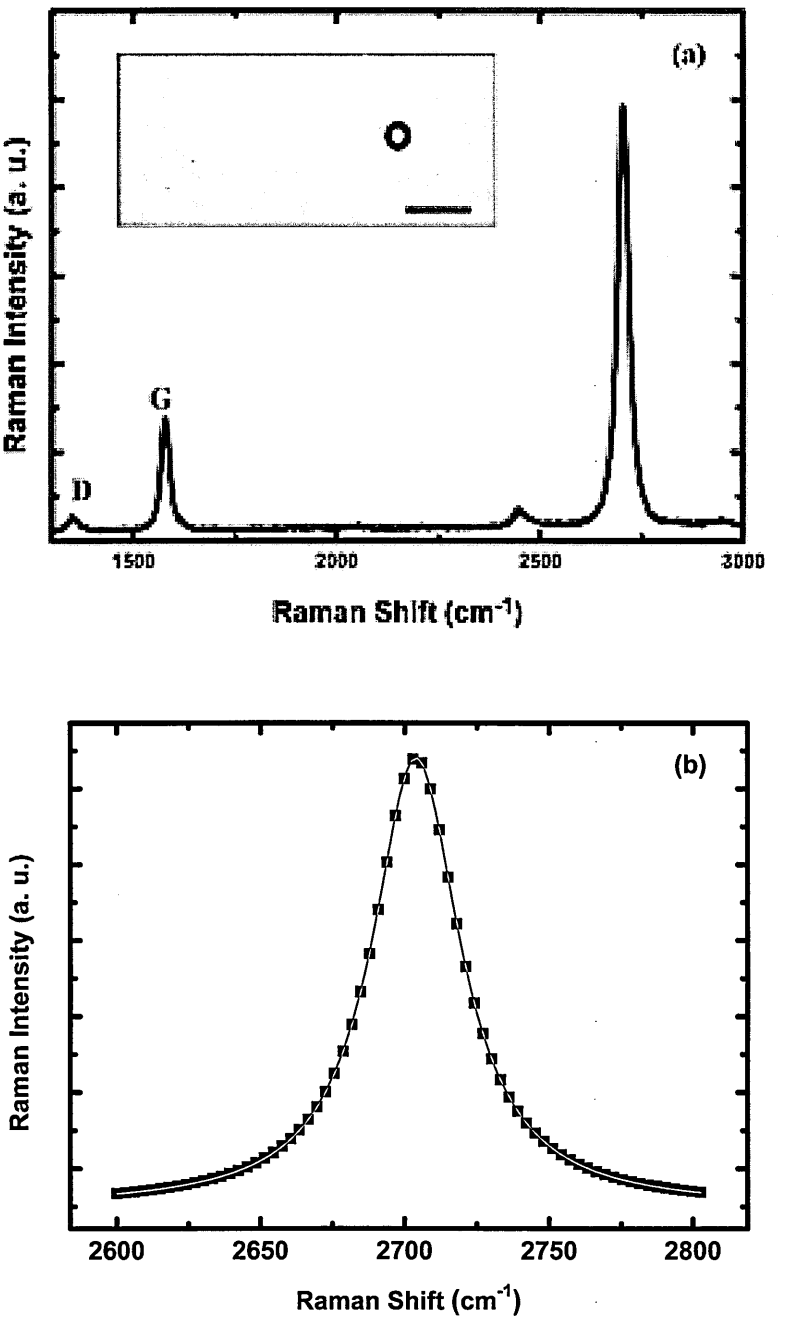

***Figure 5.5**: (a) Raman spectrum of a single layer graphene indicating D and G peaks. Inset is optical image of graphene on SiO_2 (scale bar 50 μm). (b) Corresponding Raman spectrum of the same graphene with a single Lorentzian curve fit on its raw data at the Raman 2D peak.*

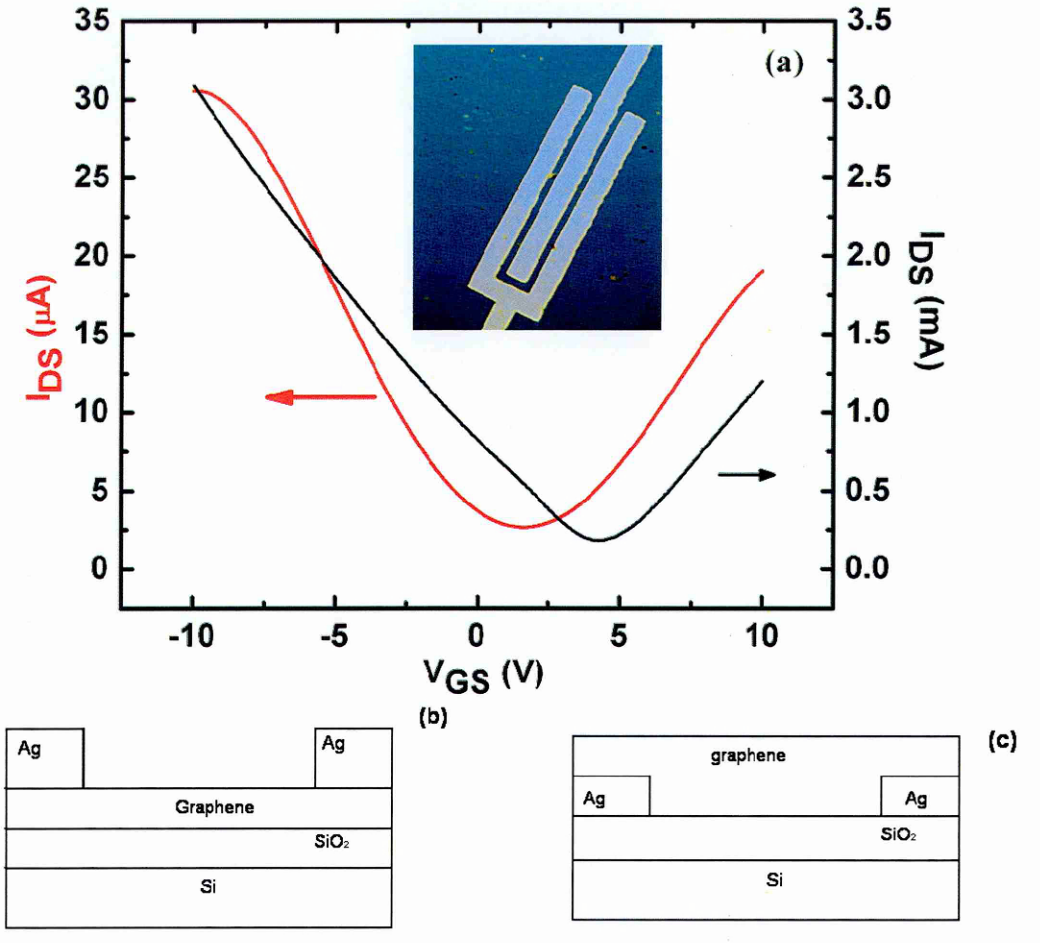

***Figure 5.6**: (a) Drain current versus gate sweeping voltage of silicon back gate graphene FET using 300 nm SiO_2 as gate dielectric for (b) top contact with the corresponding transfer characteristics in **black**, and (c) bottom contact with the corresponding transfer characteristics in red, FET schematics. Inset in (a) shows a top contact FET device with L ~50 μm, W ~ 1000 μm using 300 nm SiO_2. All FET are back gate by design with V_{DS} = 0.5 V.*

To establish a benchmark charge transport properties for our graphene both top and bottom contact topology were employed for the graphene FETs using SiO_2 as gate dielectric (Figure 5.6(b) and (c)). Comparing the results (Figure 5.6a) for both top and bottom contacts SiO_2 gate dielectric graphene FETs, there is a marked difference in the drain current I_{DS} for the two devices. Using the standard equation for mobility

$$\mu = \frac{L}{W}\frac{1}{C}\frac{\partial I_{DS}}{\partial V_{GS}}\frac{1}{V_{DS}} \qquad [5.1]$$

where gate capacitance C of SiO_2 ~ 11.5 nF/cm^2, L (~ 50 μm) and W (~ 1000 μm) are dimensions of the device, we determine the mobility of the devices. In the case of the top contact FET, the calculated typical electron mobility ~ 1172 cm^2/Vs for electrons while the calculated hole mobility ~ 1876 cm^2/Vs, is somewhat smaller than the best results reported using SiC graphitzation [161] and exfoliated HOPG [56]. Incidentally, these reported devices were fabricated using top contact electrode topology with a smaller channel length.

One major difference between the two contact topologies is in the current injection efficiencies. In bottom contact organic FET, poorer charge injection than top contact FET is often observed and has been attributed to the higher contact resistance in bottom contacts as well as difficulty in preparing highly ordered organic films on irregular surfaces [154, 158-159]. While graphene itself is an ordered structure, irregularity (e.g. surface roughness of underlying support) in graphene can have an impact on device performance [52]. Thus it is possible that similar factors may be at play for a graphene FET as well. From the above performance of the above mentioned FET, it can be inferred that the present thermal CVD process can produce graphene with performance that is reasonably comparable to other reported material performance in literature with this electrode topology.

For transistor with PVP as the gate dielectric, a back gate electrode geometry was employed in which the PVP solution was first prepared by dissolving PVP in propylene glycol monomethyl ether acetate (PGMEA), after which polymelamine-co-formaldehyde (PMF) was added as a crosslinking agent to the solution. Evaporated Ag (100 nm thick) on Corning glass, acting as the back gate electrode was first fabricated before spin-coating the PVP solution followed by a thermal curing for three minutes at 120°C. The PVP film was then UV photo-cured for three minutes for further hardening. The thickness of the PVP film was measured by AFM (Veeco Dimension) to be 1 μm thick. Ag was again evaporated onto the cured PVP film as source and drain

electrodes (i.e. bottom contact electrode topology) using the same shadow mask. Finally, graphene was transferred over to complete the back-gate FET device fabrication using the same PMMA method. It was not possible to perform Raman measurements on graphene transferred on to PVP as this structure is transparent.

Electrical I-V measurements were again performed using the combined Kiethley 2400 with 238 source meter. The drain voltage was set at 0.1 V while the gate voltage was swept forward and backward within a maximum of ± 80 V. In general the I_D -V_G characteristics were recorded under room temperature in ambient atmosphere or inert atmosphere as indicated.

Figure 5.7a and 5.7b shows drain current versus back gate voltage for the graphene on PVP transistor in ambient and after annealing at 80°C for 10 minutes in a N_2 atmosphere respectively. There was no observable neutrality point (or Dirac point) in the range of gate voltages employed strongly suggesting that the graphene layer may have some residual impurities that are doping the layer p-type. Through the measurement process, the applied gate voltage did not exceed ± 80 V as the gate leakage become significant (> 10 nA range). The gate capacitance of PVP was determined independently using capacitance measurements on a separately prepared PVP film based capacitor structure with Ag electrodes using a Keithley CV meter to be ~ 3 nF/cm^2.

The hysteresis in the I_D-V_G characteristic in Fig. 5.7a was removed by heating to 80°C in a N_2 atmosphere glove box with a measured moisture content of 1 ppm or less. There is an improvement in the conductivity and the hysteresis has disappeared, however there is still no evidence of ambipolar transport after heating. This annealing temperature was carefully adjusted to ensure it does not exceed 80°C as it was found the gate capacitance changed drastically if heated above 90°C. The carrier mobility could be found from the variation of the drain current with gate voltage (average slope

2.24 x 10^{-7} A/V) for a given drain voltage (V_D = 0.1 V) from the previous equation (5.1).

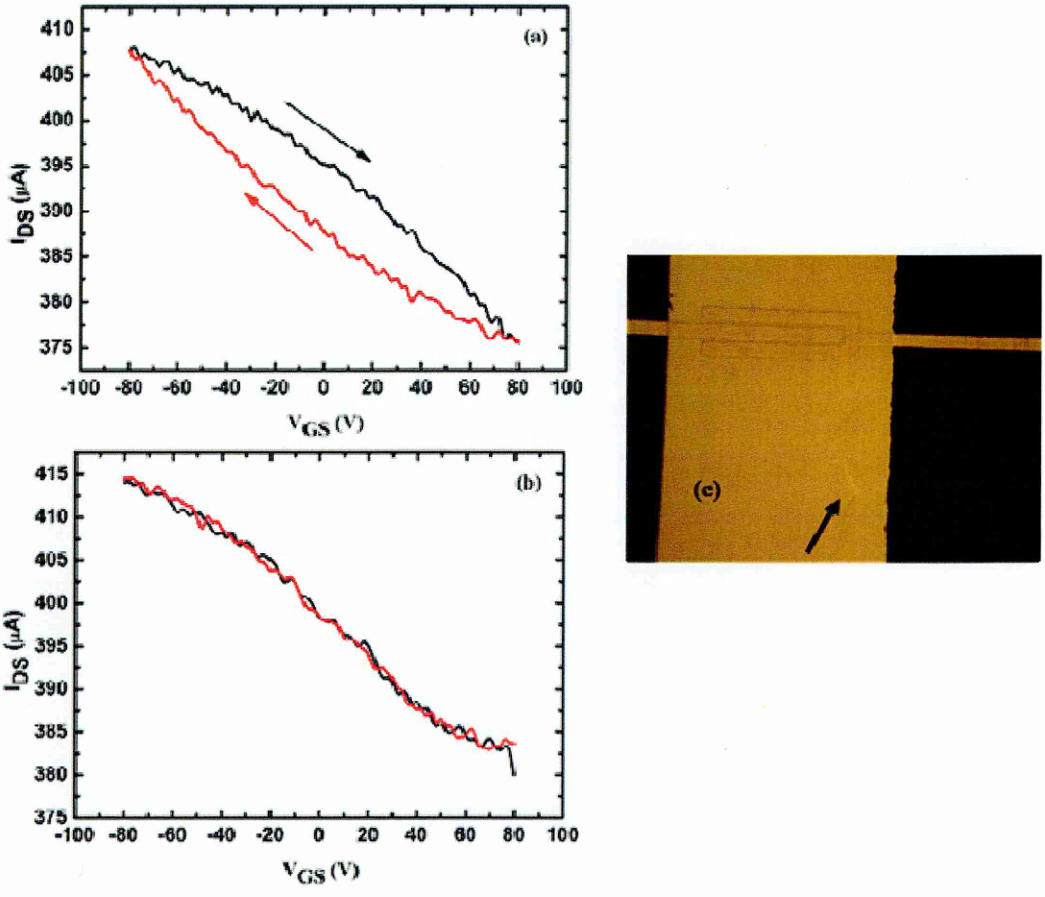

Figure 5.7: *(a) Drain current versus gate sweeping voltage of back-gate, bottom contact graphene FET using PVP polymer (1 μm thickness) as gate dielectric on a Corning glass substrate. Measurement was done in air ambient at room temperature and (b) measured in an inert ambient (N_2) chamber after heating the device for 10 min at 80°C under N_2 atmosphere. All drain source voltage is biased at V_{DS} = 0.1 V. Note the more pronounced hysteresis when the device is measured under ambient in comparison to that measured under N_2 ambient; (c) shows the microscopic image (under artificial lightings) of the device. The arrow indicates a tear in graphene.*

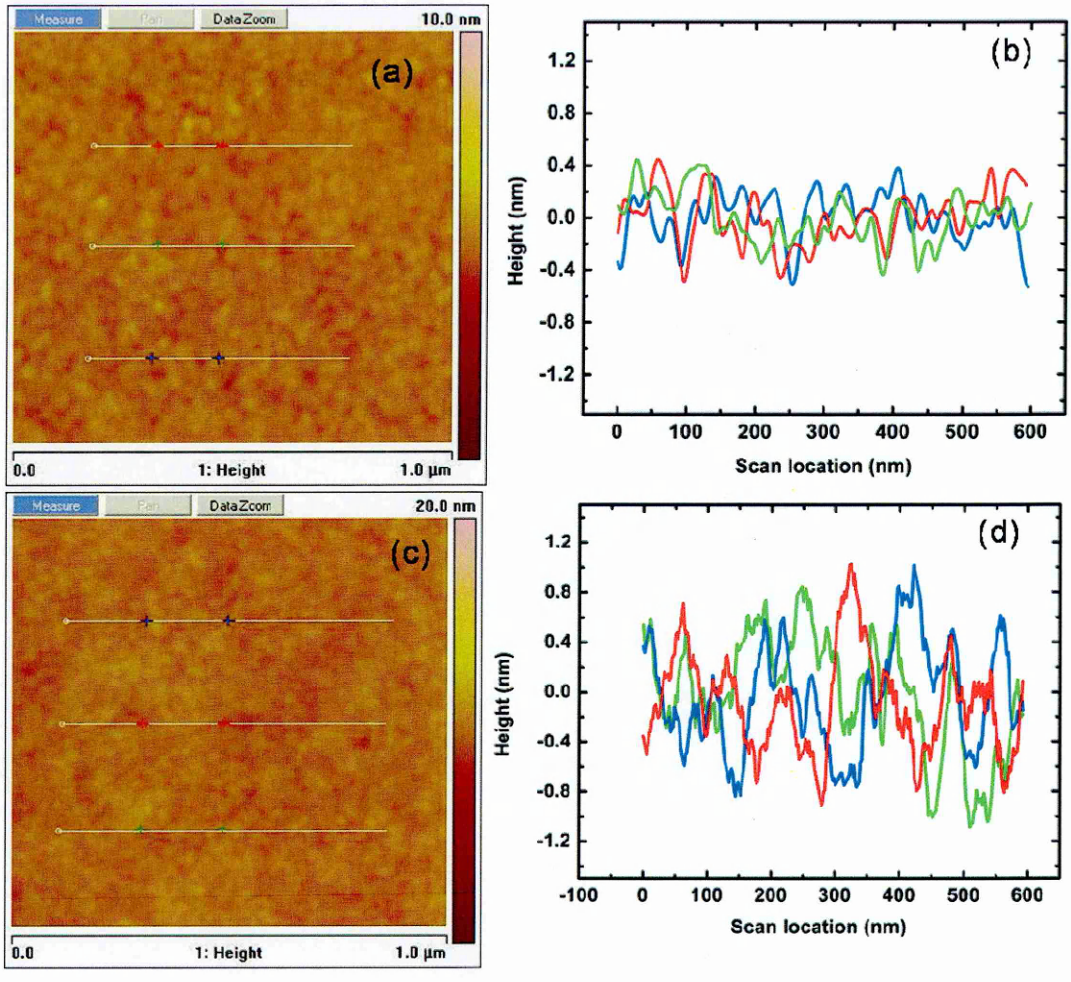

Figure 5.8: *(a) shows the AFM image (b) corresponding line scan profiles at the chosen locations on pristine SiO_2 surface. (c) shows the AFM image (d) corresponding line scan profiles at the chosen locations on PVP surface.*

Using the W ~ 1000 µm and channel length L ~ 50 µm. From the previously measured value of C_G = 3 nF/cm^2 we find that the average (average across the entire V_{GS} range) hole mobility is ~ 37 cm^2/Vs for the sample after heating. It is also observed that heating does not significantly alter the charge transport performance. It is possible that the presence of silanol groups, which are part of molecular structure in the PVP polymer, could affect the graphene's intrinsic mobility (as compared to the earlier average charge transport mobility using top-contact electrode FET with SiO_2 gate dielectric) and be responsible for the absence of ambipolar conduction. It is known that in carbon nanotube field effect transistors the absence of ambipolar conduction was attributed to the effects of silanol groups [162]. Another factor that should be

considered is the difference in surface roughness between the two gate dielectrics. Surface corrugation has been reported to have an impact on graphene's charge mobility [52]. AFM measurements (shown in Figure 5.8) of our PVP film has rms roughness ~ 3.9 nm, which is rougher than measured SiO_2 surface roughness ~ 2.6 nm rms (wafer supplied by Si-Mat).

5.4 Conclusion

In summary field effect in CVD grown graphene using Cu foil for growth and subsequently transferred to a back gate bottom contact transistor arrangement using poly-4-vinyl-phenol as an alternative to oxide based insulators was investigated. In this study, conscious choice was made to choose a simple, inexpensive fabrication route that is completely compatible to current en-mass fabrication of organic devices, to demonstrate field-effect mobility. An average hole mobility of 37 cm^2/Vs demonstrates the possibility of a graphene based all carbon based transistor for large area electronics.

CHAPTER 6

A p-type unipolar graphene device controlled via a DLC/Si heterojunction gate

As seen in the previous chapter, the use of graphene as a charge transport layer for field effect (FET) devices was widely investigated given graphene's intrinsically high mobility. This work continues the investigation of graphene in the device application through the fabrication and electrical performance of a novel three terminal graphene based device that displayed characteristics similar to a typical p-type graphene FET. This device's architecture is based on transferring graphene onto a DLC/p-Si heterostructure with p-Si as the back contact and DLC as the dielectric in contact with graphene. The resulting DLC/p-Si heterostructure provides a mechanism that can electrically moderate the I-V transfer characteristics, resulting in a p-type only conduction in graphene that also displayed electrical current saturation in the experimental I_{ds}-V_{gs} transfer characteristics of the device. The dopant-free p-type behaviour of the device gives rise to a pseudo graphene FET that shows unipolar characteristics.

6.1 Introduction

As reported in Chapter 2, earlier under the graphene review section, investigations into the use of graphene as frequency multiplier [65] and graphene field effect transistor (GFET) for logic gate functions have already been reported in the scientific literature [66]. While these devices are able to take advantage of ambipolar transport characteristic of graphene, it has been argued that two parameters: (a) unipolar charge transport, and (b) saturable current output characteristics in graphene based electronic

devices would help to promote the application of graphene towards more complicated circuit design and logic functions [163].

The realization of unipolar transport in graphene has previously been demonstrated through the molecular doping via the adsorption of gaseous species such as gaseous nitrogen or oxygen that causes a shift in the Dirac point, thus resulting in n-type or p-type transport in FETs [130]. Increase in hydrogen chemisorption can give rise to new phases of graphene with defined bandgap and unique optoelectronic properties [164]. Use of chemicals like diazonium and poly(ethylene imine) [165] are alternatives to doping and promotion of either n-type or p-type transport in FET. In Chapter 5, the use of a polymeric gate dielectric also demonstrated another route to achieve p-type only charge transport in graphene FET. Besides these techniques, the choice of metals for electrical contacts can also affect the performance of FET. Studies on metal-graphene interactions have indicated that metals can influence the position of Dirac point [166]. Furthermore, active metals such as Co and Ni can also cause saturation in FET's transfer characteristics [167].

This chapter reports a novel graphene based three terminal pseudo FET. The crucial difference between a standard Si back-gate FET and in the fabricated device reported in this chapter is that the modulation of charge transport is through the graphene channel via a diamond-like carbon (DLC or aC:H) – Si heterostructure. DLC consists of a high fraction of disordered sp^3 hybridized carbon with varying quantity of sp^2 carbon [168]. Early reports on DLC have focused on using DLC as electronic material for applications ranging from field emission [169] to FETs [170]. There was also the phenomena that heterojunction formed between Au/DLC/Si has also been observed to lead to a diode like behaviour [171].

Previously, Wu et al. demonstrated a top gated FET design where DLC has been used as a substrate support [64]. In the work described here, the DLC support layer is used as a dielectric for a FET design instead. The device architecture is achieved through the

transfer of graphene onto a DLC film deposited onto a p-Si wafer. The p-Si is used as the back gate for the resulting 3-terminal graphene device (pseudo-GFET) which displays transfer characteristics that are essentially p-type in nature. Saturation (or distortion as described by Nouchi and co-workers [167]) of the I_{ds}-V_{gs} transfer characteristics is achieved through the bias control of the Au/DLC/p-Si diode formed through the deposition of DLC on Si.

6.2 Experiments

DLC was grown using a plasma enhanced CVD (PECVD) process with the commercial tool (Surrey NanoSystem) using a previously reported process with the substrate placed on the RF electrode[172]. In brief, a pre-cleaned p-doped silicon wafer was placed on the power electrode and C_2H_2 diluted with H_2 (by 1:2 volume ratio), was flown into the chamber as the hydrocarbon source (pressure of 150 mTorr). A 50 W RF plasma was applied for the growth of the DLC thin film. The thickness of the DLC as measured from an Alphastep profilometer was observed to be 160 nm. Raman spectroscopy carried out using a Renishaw micro-Raman system with an Ar^+ laser (excitation wavelength of 514.5 nm) was used to characterize the as-grown DLC.

Graphene was prepared through thermal chemical vapour deposition (CVD) with Cu as the metal substrate/catalyst as previously described in Chapter 5. In brief, graphene is grown at 1273 K on Cu using C_2H_2 as the carbon source, and subsequently transferred onto a DLC/p-Si substrate prepared using the technique mentioned previously. The transfer of graphene was carried out either through the use of the PMMA technique [104] or by directly 'fishing' it onto the DLC/p-Si substrate upon dissolving the underlying metal substrate (without any polymer mechanical backing) used for growth. The as-grown graphene was also transferred onto a Si wafer with a 300 nm thick SiO_2 layer for subsequent Raman spectroscopic analysis.

For pseudo-FET device fabrication, the steps are as follows: 1) DLC is deposited onto a p-Si wafer as before, 2) free standing graphene is transferred onto this DLC/p-Si surface as before, and finally Au with a thickness of ~ 100 nm was evaporated as the source/drain metal contacts/electrodes with a channel length of L ~ 50 μm (and W ~ 1000 μm) on top of graphene/DLC/p-Si wafer. As stated previously, the p-doped silicon was used as the back contact of the pseudo-FET device. All electrical measurements were performed in ambient temperature and normal laboratory environment using a Keithley 4200 SCS.

6.3 Results and discussion

The Raman spectrum of graphene transferred onto a SiO_2/Si substrate is shown in Figure 6.1a. The spectrum indicates the normally observed G peak due to the in-plane vibration of C=C bonds in the hexagonal sp^2 system and a weak D peak [128]. The observation of a D peak which indicates the presence of defective hexagonal sp^2 regions in graphene is most likely due to the formation of grains which leads to a disruption of the graphene structure of the film. The Raman spectrum of DLC deposited onto Si substrate is also shown in Figure 6.1b. As is commonly observed in DLC films, this Raman spectrum consists of two broad D and G peaks due to the disordered and amorphous nature of the material [168]. Previously, works on correlating the visible Raman spectra of carbon materials with an increasing (decreasing) of sp^3 (sp^2) content were compiled [168, 173]. It is important to note that this 'amorphization' trajectory (constructed from these Raman spectra data) indicating the trend of changing from sp^2 to sp^3 is not necessary unique, but it does provide an approximate view on the properties of the DLC [168].

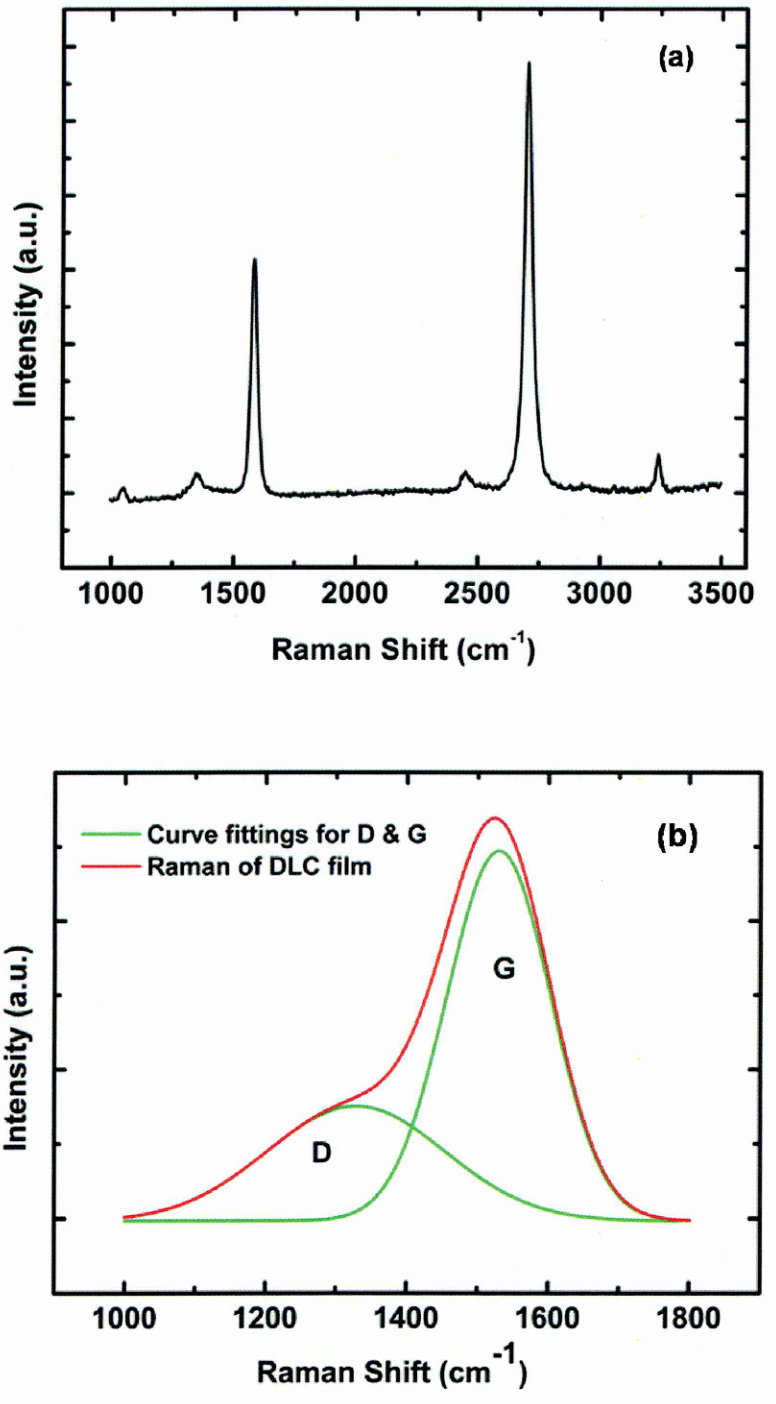

***Figure 6.1**: (a) Raman spectrum of graphene transferred onto SiO_2/Si substrate, indicating the presence of single layer. (b) Raman spectrum of DLC grown on Si substrate, with two Guassian curve fittings indicating the convoluted D and G peaks which are typical of amorphous carbon films.*

Accordingly, the combination of low ratio of I_D/I_G (~ 0.3) and the position of the Raman G (~ 1527 cm^{-1}) indicate that the sp^3 content is between 30 % to 60 % range.

This meant the as-grown film is not graphitic or nano-graphitic, but within the aC:H families [168]. The as-grown DLC is found to be 'quite hard' – an informal test by scratching the surface with a diamond scriber, indicating the H content in the DLC is not exceedingly high, else the DLC will be a soft polymer-like film.

The measurements of the transfer characteristics of FET devices based on a bottom gated, top-contact device architecture is shown in Figure 6.2a. Measurements were carried out under different drain biasing using with the source grounded. The resultant curves showed a similar profile for source drain voltages up to 100mV DC. Several important observations can be made from the results presented in Figure 6.2a (with the corresponding schematic of the device in figure 6.2d). These include that the device does not display a clear Dirac point in the transfer characteristics. If any such point was to exist, it should be at voltages higher than 40 V (the maximum voltage studied). Due to the absence of a Dirac point, the n-type also appears to be suppressed with the characteristics due to whole transportation being prevalent even under positive gate biasing. Furthermore, the transfer characteristics display some form of saturation-like behavior. The behavior observed is analogous to a p-type Si-MOSFET inverter logic, where high V_{gs} (V_{gs} is positive) produces a lower value of Ids compared to a low V_{gs} (V_{gs} is negative) which results in a higher I_{ds} output.

Studies on metal-graphene interactions indicated the graphene can be doped by the metals such as Co [166], Ti [163] when used in place of Au as the source/drain contacts. This leads to saturation in drain current I_{ds} (especially pronounced when $V_{gs} < 0V$) in the transfer characteristics of a short channel GFET. These studies propose that the electrical current distortion and saturation observations result when these metals interact with oxygen, and subsequently form a metal-oxide interface with the underlying graphene. Since our device using only Au as metal contacts, this mechanism can possibly be discounted.

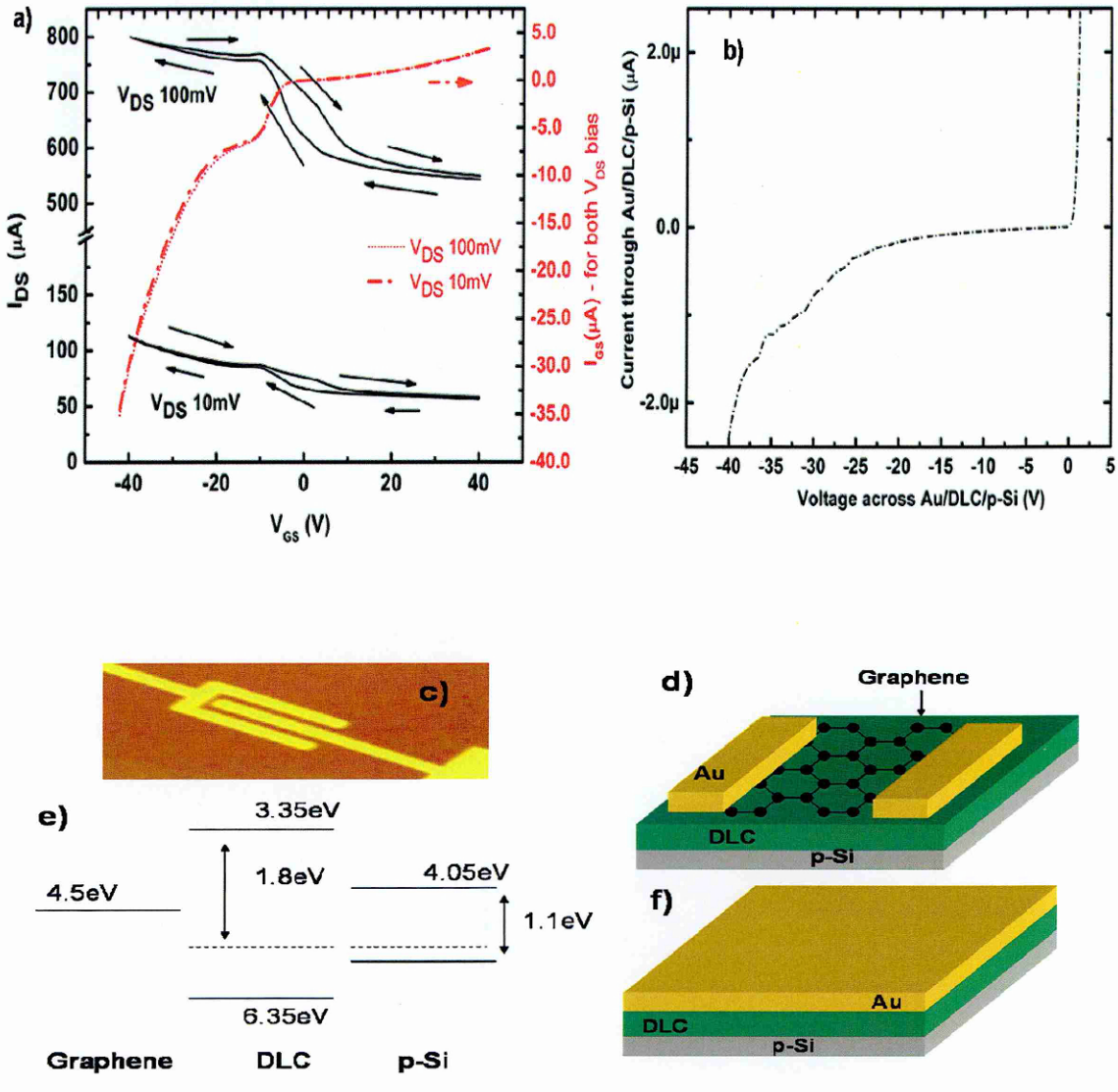

***Figure 6.2**: (a) Transfer characteristic (I_{ds} – V_{gs}), at two different V_{ds} bias, of the fabricated GFET device. Figure b) shows the I-V characteristics of a Au/DLC/p-Si diode heterostructure with the corresponding device schematic in figure 2f., c) is the microscopic image of a top-contact Au on graphene/DLC/p-Si FET structure (under artificial lighting) with the corresponding device schematic shown in d), and e) shows the flat band diagram of the back-gate DLC/p-Si heterojunction [171]. Note the difference in the turn-on voltages between a Au/DLC/p-Si structure versus the back-gate DLC/p-Si heterojunction in GFET. FET's L ~ 50 μm and W ~ 1000 μm.*

In order to understand these anomalous characteristics, *I-V* characterization of the DLC film was carried out based on a sandwich structure on a p-type Si substrate with evaporated Au as the top contact. The use of Au as a top contact is believed to lead to an ohmic contact while the use of p-Si is expected to lead to the formation of a heterojunction [171] (see figure 6.2f). During the forward biasing of the device (DLC

negative w.r.t. p-Si), holes are injected from p-Si into DLC while during reverse biasing trapped electrons are liberated from DLC (and injected into Au) leading to increased electron-hole pairs and subsequent avalanche breakdown which is observed experimentally to be reversible. Looking at the gate leakage current of the GFET and comparing this against the *I-V* characteristics of the Au/DLC/p-Si diode device offers some interesting salient points. When $V_{gs} < 0V$, the gate current I_{gs} displayed a characteristic similar to that of the Au/DLC/p-Si breakdown behavior that was observed in figure 6.2b. Correspondingly, a large upward jump in the I_{ds} values is also observed (compared to that when $V_{gs} > 0V$). This behavior may be explained as follows: during negative gate biasing, the graphene channel allows the transportation of holes. However, once the p-Si gate has been sufficiently biased a fraction of holes that is transported in graphene are now injected into the DLC, resulting in the initiation of breakdown of the Au/DLC/p-Si diode and henceforth the observed behavior of the GFET's I_{ds}-V_{gs} when $V_{gs} < 0V$. There is a noted difference in magnitudes of the currents between an Au/DLC/p-Si structure versus GFET when $V_{gs} < 0V$. From studies on organic FET, it has been reported that graphene is a better charge injections than metal contacts [174-175]. Thus a similar mechanism may be at work here, causing a discrepancy between the different current magnitudes in the two devices.

When the gate voltage is biased positively ($V_{gs} > 0V$), unlike the Au/DLC/p-Si structure, the corresponding turn-on voltage in the GFET is noticeably at a much higher value. This implied there is no large inject of electrons into the DLC from p-Si in the GFET device. This expected lack of injections of electrons into the DLC from p-Si corresponded to the rather flat I_{ds} behavior as shown in figure 6.2a. Thus this implies that DLC dielectric seems to be inhibiting the 'normal' modulation of channel current (I_{ds}) in graphene under an applied sweeping V_{gs} if there is no injection (or extraction) of charges due to the back-gate DLC/p-Si heterojunction structure. Furthermore, there is also presence of a significant hysterisis was also observed in the transfer characteristics of the GFET. Previous work on graphene FETs on a SiO_2 gate dielectric has indicated

that charge trapping at the graphene/SiO_2 interface as the possible cause for such a hysterisis [176]. As DLC is known to have large traps and defects [177], a similar mechanism can be thought of to result in the hysteresis observed in this work. Besides causing hysterisis, it has been observed that the performances of ON-OFF ratio and electron transport for a graphene in a field effect device are also influenced by the presence of traps and defects in dielectrics [178], which accordingly the ON-OFF ratio can fall under two when trap charges increase towards the 10^{13}~10^{14} cm^{-2} range. Thus, our device's poor ON-OFF ratio may be due to the presence of such trap states in the DLC dielectric used.

In addition to the discussed I_{ds} – V_{gs} transfer characteristics of graphene due to the presence of the DLC/p-Si heterojunction and DLC dielectric itself, the possibility of p-doping of graphene due to the DLC should also be considered. The formation of CO bonds in graphene has previously reported to lead to p-type only conductivity in graphene [179]. The presence of C and O in the DLC film, which was prepared by depositing a layer of DLC on quartz using the above mentioned PECVD process, was observed in the infrared (IR) measurements (using Nicolet FTIR) as shown in figure 6.3a. Furthermore, a blue shift in the Raman 2D peak of graphene on a DLC substrate in comparison to the Raman 2D peak of graphene on SiO_2 surface also indicates the p-type doping of graphene by the underlying DLC. Thus, a combination of these two factors may also lead to a distinct lack of n-type conduction in our graphene device.

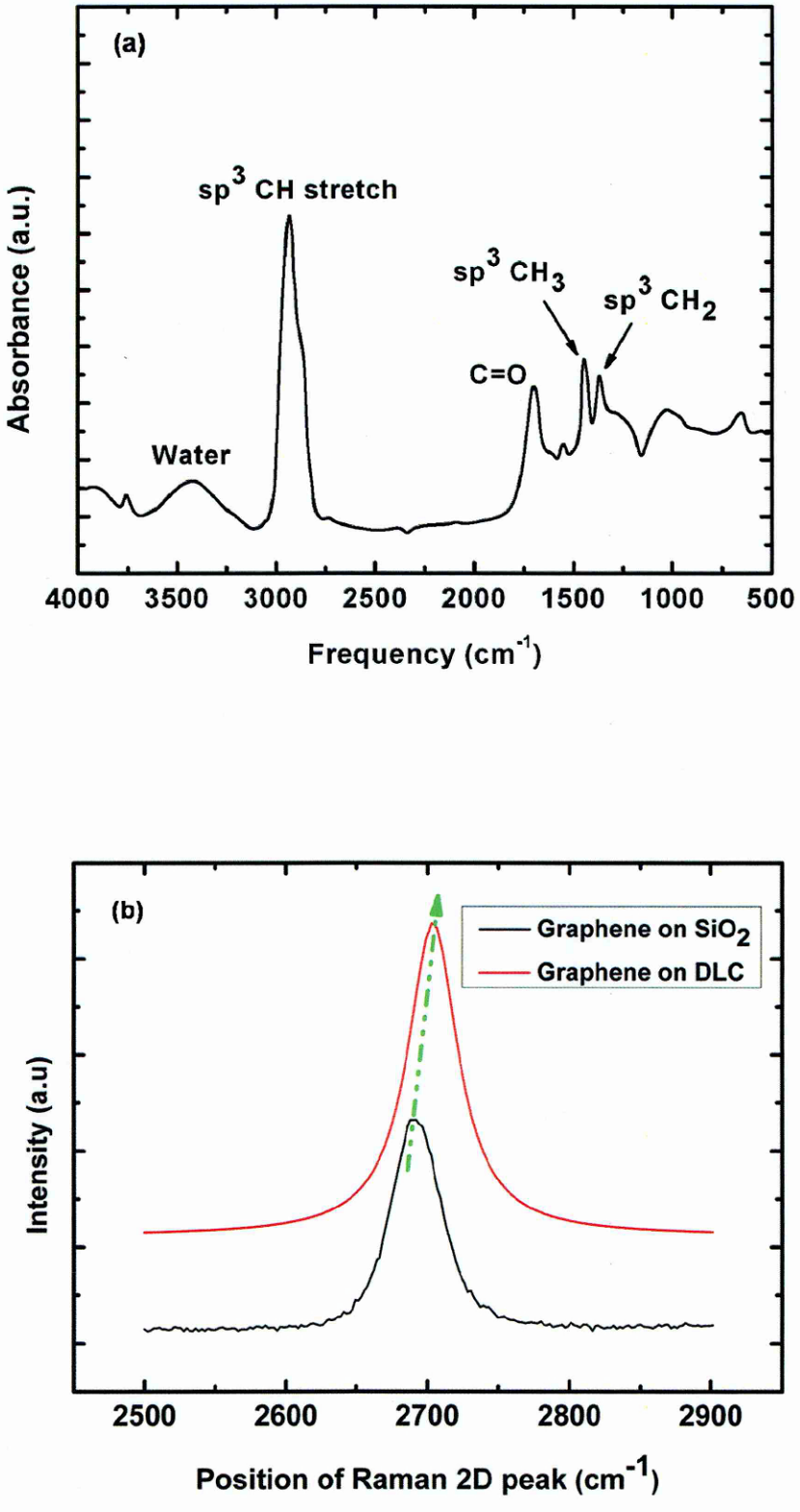

***Figure 6.3**: (a) IR measurement of DLC on quartz, indicating the presence of various CH and CO bonds in the amorphous film. (b) Blue shift in Raman 2D peak when graphene is transferred on DLC as compared to when graphene is transferred onto a SiO_2 surface.*

Finally the mobility of the device is determined using the previously mentioned equation [5.1] in Chapter 5. For the given voltage bias of 100mV, within the range of V_{GS} = ±10V, the mobility was found to be ~ 32 cm^2/Vs which indicated a much reduced value compared to that commonly observed for SiO_2 gate dielectric based graphene FET [56]. However, this value is comparable to that observed in previous chapter's study on graphene FET with organic dielectric. This may also be attributed to the presence of traps and defects in DLC which can greatly affect the mobility in graphene [178].

6.4 Conclusion

In conclusion, this section reported the fabrication and electrical performance of a 3 terminal graphene based device that displayed characteristics similar to a p-type graphene FET. While past investigations of distortion and saturation in I_{ds}-V_{gs} characteristics of graphene FET indicated that metal-graphene interaction may be the underlying mechanism, our device operation is based on the design transferring graphene onto a DLC/p-Si heterostructure with Si as the back contact and DLC as the dielectric in contact to graphene. The insulating nature of undoped DLC prevented electrical short circuit formation between the top Au/graphene with the Si back contact. Thus this provided a mechanism for the DLC/p-Si heterojunction to remotely moderate the Ids-Vgs characteristics electrically, resulting in a p-type only conduction in graphene that is also saturable.

CHAPTER 7

Photo-thermal growth of graphene on Ni

Following the work on the previous chapters on using conventional thermal CVD for graphene growth, it is natural to explore the possibility of using the previously mentioned PT-CVD to develop a graphene growth process. It was found that the non-thermal equilibrium nature of PT-CVD process resulted in a much shorter duration in both heating up and cooling down, thus allowing the reduction of the overall growth time for graphene compared to standard thermal chemical vapour deposition (T-CVD) but without reduction in the quality of the deposited graphene film.

Furthermore, in comparison to that in the conventional T-CVD process, graphene formation under PT-CVD is much less sensitive to cooling rate. Growth on Ni also allows for the alleviation of hydrogen blister damage that is commonly encountered during growth on Cu substrates. To characterize the film's electrical and optical properties, we further report the use of pristine PT-CVD grown graphene as the transparent electrode material in an organic photovoltaic device (OPV) with poly(3-hexyl)thiophene (P3HT) / phenyl-C61-butyric acid methyl ester (PCBM) as the active layer where the power conversion efficiency of the OPV cell is found to be comparable to that reported using pristine graphene prepared by conventional CVD.

7.1 Introduction

Recently, graphene has been utilized for a wide variety of applications, including as the transparent electrodes for organic solar cells [180] and fuel cells [181], amongst others. While the popular fabrication technique is to produce single layer graphene by mechanical exfoliation, this method is not amenable to large scale production of a large area film. Chemical routes, such as those based on Hummers's oxidation method [182],

have also been explored as a method for large scale graphene production, however the quality of the resultant film is lower compared to that found in using exfoliation process due to the presence of residual oxygen moieties on the surface. Graphene synthesis by sublimation of single crystal 4H-SiC [92] is another popular alternative which has been demonstrated to produce high quality single layered graphene. However, the cost of this process is very high due to the use of single crystalline SiC and the size is limited. By contrast chemical vapour deposition (CVD) has emerged as the leading growth method that is inherently scalable for large area film production. A second key advantage of using CVD based methods is the ability to dissolve the underlying metal for transferring graphene to an arbitrary substrate[104]. To date Ni [104] and Cu [106] are two common choices used in non-UHV CVD growth of graphene.

Previously in Chapter 4, demonstration of carbon nanotube synthesis by the photo-thermal chemical vapour deposition (PT-CVD) method was reported. The experience in using rapid thermal processing in Si fabrication has shown that unlike conventional resistive heating, the use of a rapid optical heating under vacuum meant the growth process is in non-thermal equilibrium with a large thermal gradient between the sample and surrounding process chamber [183]. Since this surface radiant energy deposition can be affected by a variety of factors like wavelength dependent absorption of the thermal energy, reflections of thermal energy from the enclosing vacuum chamber among others, the mechanism is still not well understood [183].

Despite this, it is felt that this growth technology may possibly offer several technological advantages over conventional CVD especially in graphene growth. While most reported graphene CVD growth uses a hot-wall system, there is an advantage of using cold-wall CVD instead as deposition on side-walls leading to sample contamination can be minimized [183]. Furthermore, it was observed that photo-induced rapid thermal processing reduces the overall process time due to a very much

shorter duration for both heating up and cooling down, and that the graphene formation under PT-CVD seems much less affected by the much faster cooling rate. As pointed in Chapter 2, this is important for metal catalysts that have relatively high carbon solubility.

In this present work, PT-CVD is used to demonstrate grow graphene growth on a polycrystalline Ni substrate using acetylene as the hydrocarbon source with much faster turnaround process time than a standard thermal CVD. Ni has been used in this work since it allows for the alleviation of hydrogen blister damage that is commonly encountered during growth on non-oxygen free Cu substrates.

7.2 Solar cell basics

As part of the investigations reported in this section, an organic solar cell (OPV) was fabricated with the graphene acting as a transparent conductive electrode. Here a review on the basic operations of an organic solar cell as well as the salient parameters used for the characterization of such a device is discussed. At present, several different types OPV architectures are actively being investigated [184-185]. For the current work, the fabricated OPV is based on the bulk heterojunction OPV design as shown in the following diagram.

Figure 7.1 shows a qualitative explanation of the principle OPV by breaking into four distinct steps:

1. When a photon incident onto the organic donor material, an exciton (electron-hole pair) is created as the electron is excited from the highest occupied molecular orbital (HOMO) into the lowest unoccupied molecular orbital (LUMO).

2. The exciton diffuses into the interface of the two organic materials - donor and acceptor layer.
3. The exciton is dissociated at the interface.
4. The separated electric charges diffuse to the OPV's electrodes, thereby generating energy for external work done.

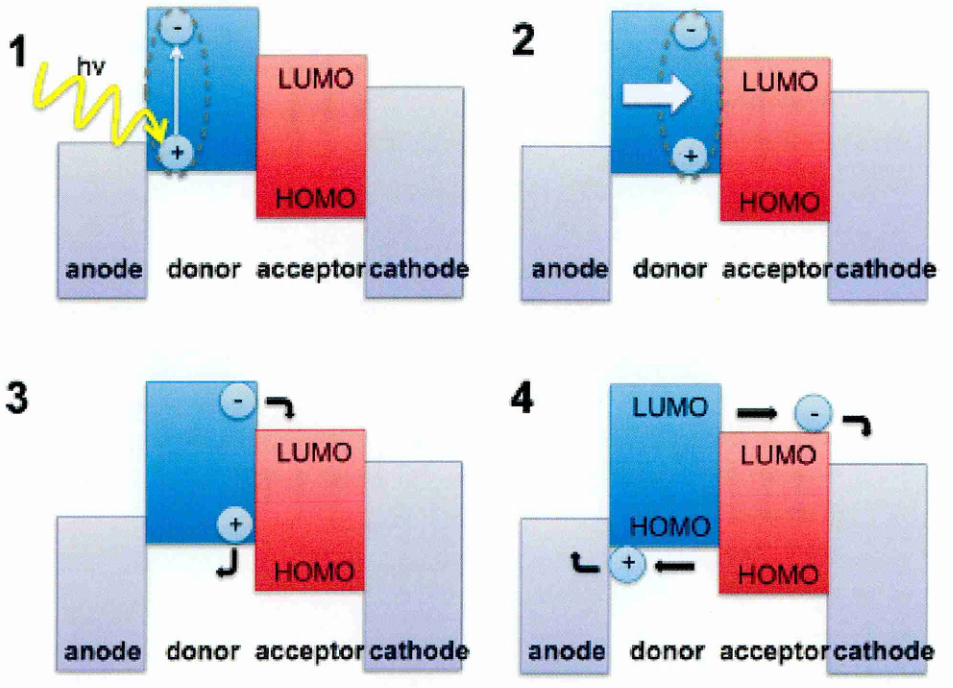

***Figure 7.1**: Basic principle of OPV [186].*

In practice, the bulk heterojunction OPV would have a typical schematic as follows, where it is clearly seen that the donor and acceptor layers are actually blended into a single layer (as shown in Figure 7.2). To characterise the performance of such a solar cell, the cell's IV characteristics is taken with and without light illumination. Ideally, a solar cell operates like a diode in parallel with a current source. In the absence of sun light, the IV curve resembles that of a diode. Under solar illumination, the absorption of light generates a current. Figure 7.3 shows a typical IV characteristic under the various conditions and the electrical model of the OPV cell:

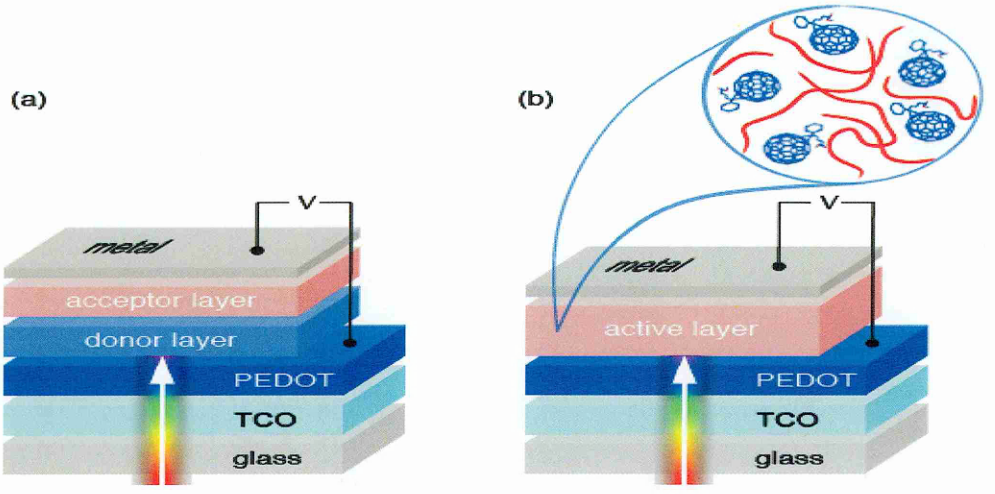

***Figure 7.2**: Schematic of a (a) bilayer with planar heterojunction OPV and that (b) bulk heterojunction OPV in which the active layer is blended into a single layer [187].*

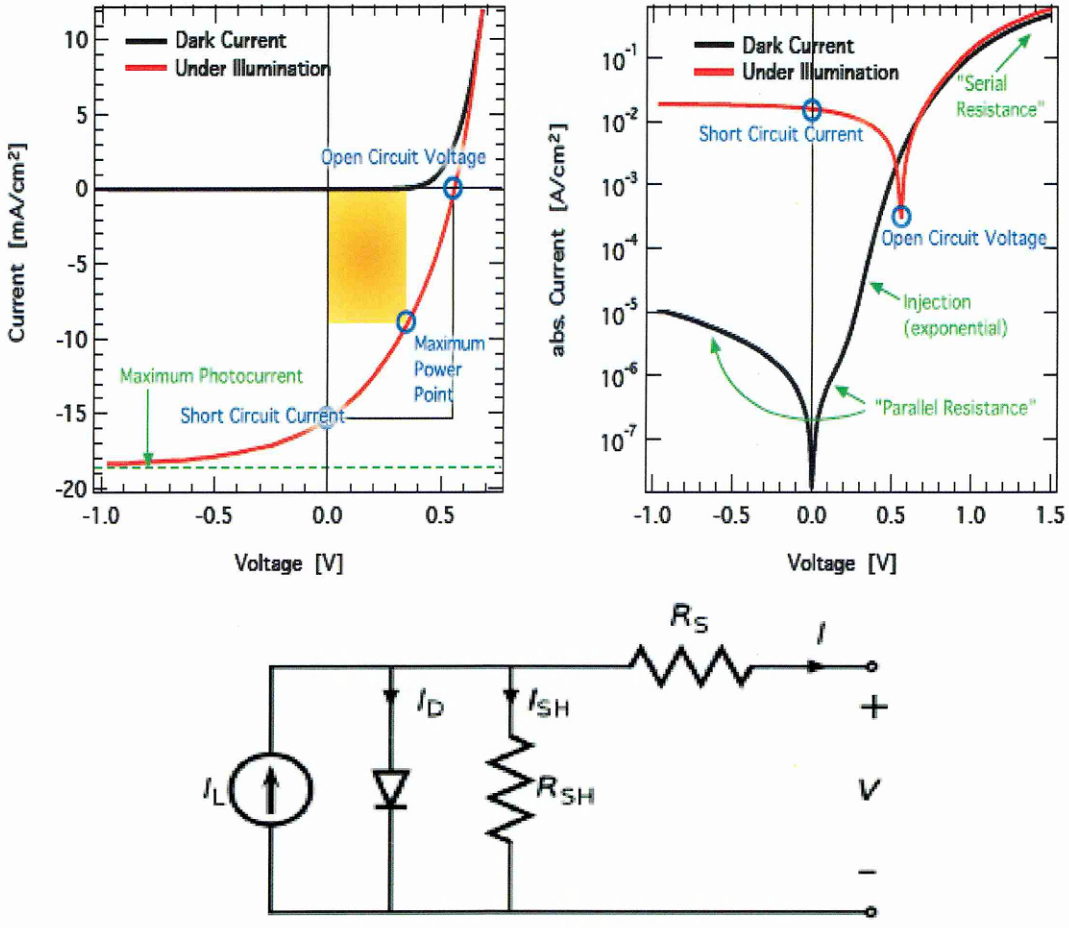

***Figure 7.3**: (Top) IV characteristic of OPV under dark and solar illumination. Both graphs showed the same data set but were plotted with linear (left) and semi-log (right) scales respectively [187]. (Bottom) shows the equivalent circuit model of an OPV cell [188]. Note that the parameters of the model can be fitted into the IV characteristic of the OPV by assuming a modified Shockley equation.*

By measuring the incident solar radiation, the power conversion efficiency (PCE) is calculated as follows:

$$PCE, \eta = \frac{FF \times j_{sc} \times V_{oc}}{P_L} \qquad [7.1]$$

where j_{sc} is the short circuit current, V_{oc} is the open circuit voltage and P_L is the incident light illumination. These are defined as shown in the Figure 7.3. The fill factor, FF, is defined as the ratio of maximum measured power to maximum theoretical power, in effect this factor measures the 'squareness' of the *I-V* characteristic under illumination.

7.3 Experiments

The main tool for this work is the PT-CVD system (Surrey Nanosystem SNS NanoGrowth 1000) as described in Chapter 3. Ni foil (25 μm thick) was first cleaned by acetone, IPA and methanol and placed on the substrate holder. At a base pressure of better than 10^{-2} Torr, a mixture of Ar /H_2 (total of 100sccm) was introduced. The IR lamp is switched on simultaneously for duration of 5 min to anneal the Ni foil to reduce any oxide on the surface. Maintaining the temperature at 700°C, the Ar/H_2 mixture was switched off and C_2H_2 (2 sccm) was introduced for 5 sec. It is observed that increasing the duration of C_2H_2 tend to result in multi-layer graphene growth dominating the surface of Ni. This is consistent with earlier mentioned fact that Ni has high carbon solubility. After the growth period, both the IR lamp and the C_2H_2 flow were switched off and Ar/H_2 mix was re-introduced in order to cool the sample down to room temperature at a rate of approximately ~ 100°C/min. The effect of dilution of C_2H_2 with H_2 was also carried out but no observable difference in the film quality or surface coverage was detected by subsequent Raman spectroscopy.

The as-grown graphene sample on Ni foil was examined first both optically and using Raman spectroscopy (Renishaw microRaman, 514 nm Ar^+ laser). Afterwards, the graphene layer was transferred onto SiO_2 (300 nm)/Si substrate using either the PMMA based transfer technique mentioned in Chapter 5 or through direct lift off from a Ni etchant solution (Alfa Aesar commercial Ni etchant). Further Raman spectroscopic analyses were carried out on the graphene upon transferred to SiO_2. Graphene was also transferred onto a TEM holey grid (Agar) for examination using a Hitachi HD2300 Scanning Transmission electron microscope (STEM). Optical transmission properties of the film were investigated using a Cary 5000 UV-Vis spectrometer and electrical characterization was performed using a Kiethley 4200 semiconductor characterization system.

Finally, the graphene film prepared by PT-CVD was used as the transparent electrode in an organic photovoltaic (OPV) device. The OPV device is fabricated using the previously reported process [189].

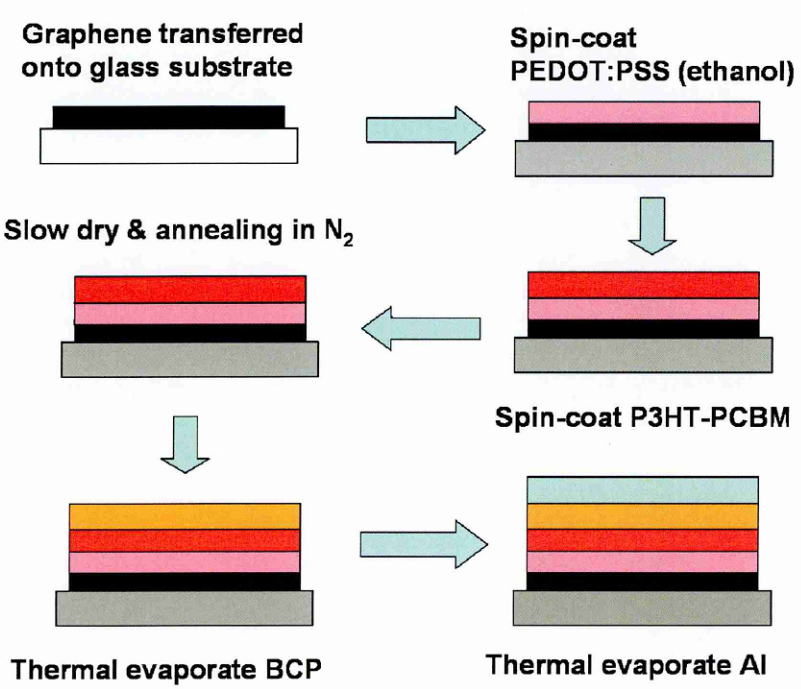

Figure 7.4: *Flowchart of overall OPV fabrication steps*

First graphene is transferred onto a glass substrate, followed by using the 'spin and drop' technique to coat the graphene's surface with a PEDOT:PSS at 500 rpm for 40 sec. After this, the active layer of P3HT:PCBM (in dichlorobenzene) is spin-coated onto at 750 rpm for 1 min. This is then left to dry for 1 hour and subsequently annealed at 110°C for 15 min. BCP (2 nm thick) and Al (70 nm thick) were then thermally evaporated sequentially to form a hole blocking layer and as the electrode respectively. All the fabrications were performed in a N_2 glove-box to minimise exposure to ambient. The OPV device was characterized with a solar simulator operating under AM 1.5G illuminations. Solar simulator was calibrated with a Newport reference cell. A Kiethley 2400 sourcemeter was used for as the electronic load for measurements.

7.3 Results and discussion

As discussed in Chapter 2, there are two main proposed growth mechanism for the formation of graphene on metal catalysts: 1) carbon dissolution-precipitation, and 2) direct deposition of graphene using catalysts with negligible carbon solubility. While the lack of in-situ experimental tools prevent direct observations and verification of the growth mechanism in PT-CVD, it is possible to consider the following simple model to assist in providing insights to the plausible mechanism for graphene formation.

Considering that Ni is used for the study in this section, it would be important to consider the solubility of carbon in Ni at the desired processing temperature and time. Using the solution for Fick's second law of diffusion [190] as follow:

$$\frac{C_x - C_i}{C_{surf} - C_i} = (1 - erf(\frac{x}{2\sqrt{Dt}})) \qquad [7.2]$$

where D is diffusion coefficient of carbon in Ni, x is depth of diffusion into Ni, t is time, C_i is initial carbon concentration in Ni, C_x is carbon concentration at depth x, C_{surf} is the arriving carbon on the surface of Ni and erf() is the Gaussian error function:

$$erf(z) = \frac{2}{\sqrt{\pi}} \int_0^z e^{-(y^* y)} dy \qquad [7.3]$$

Values of diffusion coefficients of carbon in Ni are obtained from [191]. The following assumptions are also made, 1) there is no initial carbon concentration in Ni, and 2) a constant concentration of carbon is present at the surface of Ni due to decomposition of the carbon feedstock. The assumption of no initial carbon concentration in Ni is merely for mathematical convenient, thus any resultant carbon profile in subsequent analysis would only imply an underestimation of carbon concentration in Ni. As for the second assumption, this is fulfilled by the use of acetylene instead of CH_4 to provide the constant of source of carbon since pyrolysis of acetylene can take place between 700K to 1200K [192], within the range of PT-CVD processing temperature. Furthermore, it is also known that Ni(111) on a polycrystalline Ni surface can assist in breaking C-C bond, which has a lower energy barrier than C-H bond [193-194]. Saturation of the Ni is not expected during the growth process due to the small C_2H_2 flow rate (2 sccm) with short time duration (5 sec), and the relatively thick Ni foil (25 μm). In additional, graphene formation was not experimentally observed when the Ni sample underwent the same PT-CVD growth process without the presence of any carbon feedstock. This indicates the absence of graphene formation via carbon segregration process from the initial carbon concentration inside the Ni sample, which has previously been reported as an alterative method for growing graphene [195].

Using this simple model (Figure 7.5), at 700°C after 5 sec, the concentration of C is within 80% of the carbon concentration at the surface. Thus carbon can be absorbed into the Ni during this elevated temperature, and together with the initial carbon concentration inside Ni before undergoing the growth process, can subsequently

precipitate to the surface of Ni, forming graphene upon cooling. Thus this indicates that graphene formation via the carbon dissolution-segregaton-precipitation route is more likely than direct deposition of graphene. Attempts to use direct deposition of graphene instead of the carbon dissolution-segregaton-precipitation route through the use of a low carbon soluble catalyst like Cu under the PT-CVD process (~ 700°C) has so far failed to produce graphene. To the author's knowledge, demonstration of this direction deposition route at low temperature (≤ 600°C) for Ni is restricted to UHV-CVD processes [196].

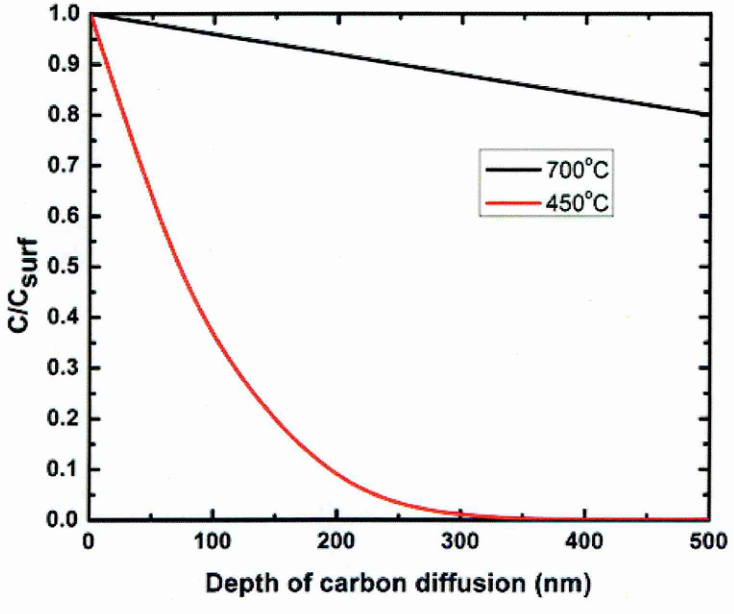

Figure 7.5: *Diffusion profile of carbon in Ni at different temperature. Carbon concentration is calculated as a fraction of* C_{surf}.

Figure 7.6a and 7.6b show the optical image (Leica microscope) of graphene on the Ni foil upon PT-CVD growth and its corresponding Raman spectra (respectively). Dark boundaries are observed on the surface of the Ni foil that were previously absent in the pristine Ni foil as received from the supplier (inset of Figure 7.6a). The straight lines running across the pristine Ni foil is believed to be due to the cold-rolling process used for the production of the metallic foil. It is observed 'boundaries' in the foil after the

growth process. While the origins of these await further investigations, these boundaries may potentially lead to a discontinuous graphene film.

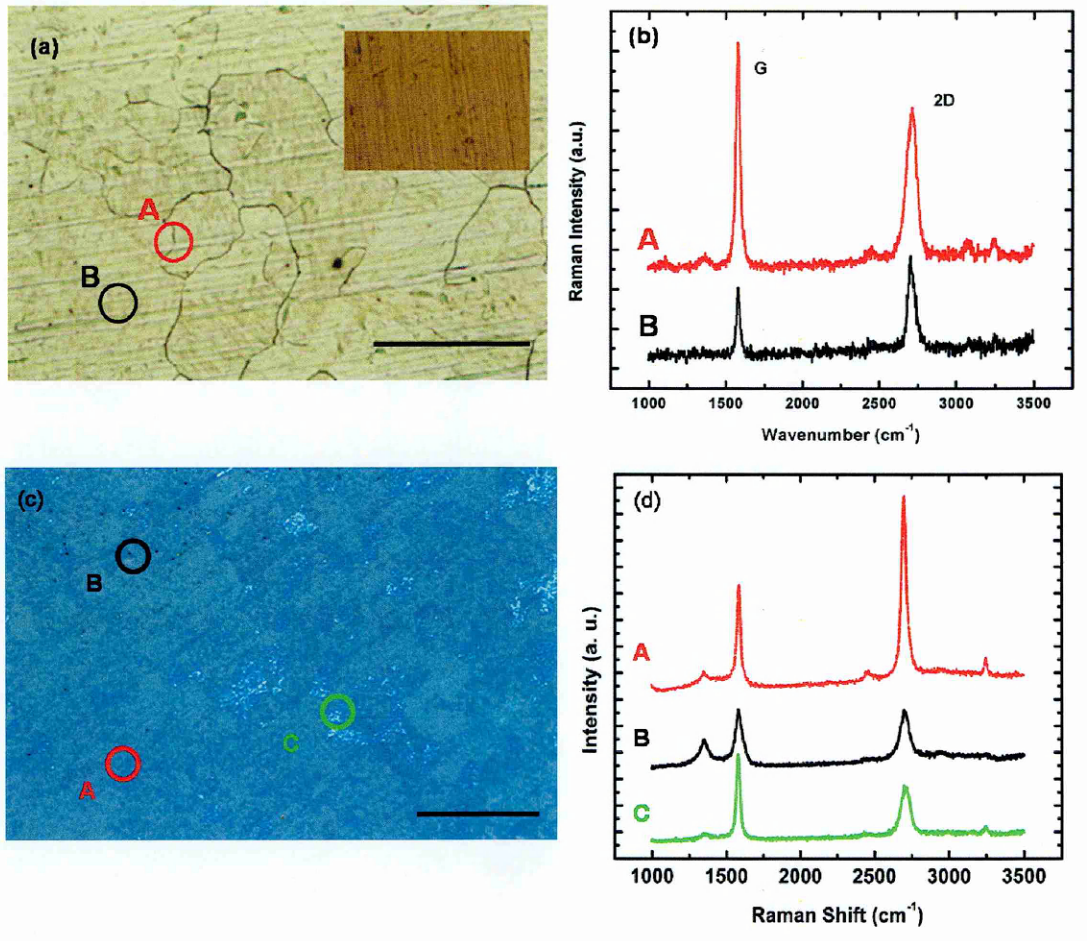

***Figure 7.6**: (a) Optical image of the graphene as grown on Ni foil. Inset is the Ni foil before undergoing the growth process. The film surface seems to exhibit 'boundaries' that maybe related to the grain size of the underlying Ni foil. (b) Raman spectra at the corresponding points of the optical image in (a). Points A and B on figure left (a) correspond to the Raman spectra of A and B in figure right (b) respectively Note the wider FWHM in the Raman 2D peak measured on the darker pattern on the sample which may be indicative of a few layer graphene. (c)Optical image of the graphene after transferred on a 300 nm SiO_2 wafer, (d) Raman spectra at the corresponding points on the graphene. Points A, B and C on figure (c) correspond to the Raman spectra of A, B and C in figure (d) respectively. The Raman spectra indicated that the film has few layer graphene on certain places, thus the film may not be completely single layer. Furthermore, some places have a higher Raman D peak indicating defects in the graphitic structure. It is not clear if the defects are inherent in the growth process or the result of damages caused during the graphene transfer from Ni to SiO_2. Bar scale 100 micron.*

One possible cause may be due to different thermal expansions between graphene and Ni during the growth process [103-104]. Graphite is known to have a different thermal expansion profile [197] from that of Ni [198]. It is noted with interest that in Chapter 5, a similar exhibition of 'dark streak-lines' were observed on Cu foil after undergoing the graphene growth process, but no 'boundaries' were observed on the Cu foils.

The Raman spectrum at the boundary line as indicated in the optical image (Fig 7.6 (b)) shows a higher I(G)/I(2D) ratio, indicating the possibility of few layer graphene [199]. Furthermore, the FWHM of the 2D peak is wider (some of these sites' FWHM approximated to ~ 90 cm^{-1}) compared to a region away from the boundary. This further indicate a possibility of a higher graphene layer count at the boundaries than at sites away from the boundaries as is often observed in CVD growth of graphene using Ni as catalyst [103].

Dark boundaries are observed on the surface of the Ni foil that were previously absent in the pristine Ni foil as received from the supplier (inset of figure 7.6a). The straight lines running across the pristine Ni foil is believed to be due to the cold-rolling process used for the production of the metallic foil. It is observed 'boundaries' in the foil after the growth process. While the origins of these await further investigations, these boundaries may potentially lead to a discontinuous graphene film upon cooling after the growth process [103-104]. The Raman spectrum at the boundary line as indicated in the optical image (Fig 7.6 (b)) shows a higher I(G)/I(2D) ratio, indicating the possibility of few layer graphene [199]. Furthermore, the FWHM of the 2D peak is wider (some of these sites' FWHM approximated to ~ 90 cm^{-1}) compared to a region away from the boundary. This further indicate a possibility of a higher graphene layer count at the boundaries than at sites away from the boundaries as is often observed in CVD growth of graphene using Ni as catalyst [103].

The as-grown graphene was transferred onto SiO_2 (300 nm thickness)/Si for further examination. Optical image of the film and Raman spectra at selected sites on the film

are shown in Figure 7.6c and 7.6d. A FWHM of 38 cm^{-1} (by fitting with a single Lorentzian) for the 2D peak (2695 cm^{-1}) of the Raman spectrum indicates the presence of single layered graphene [128], while some sites on the film also indicated a higher defect (more pronounced D) peak which may be due to the exposure to acid etchants used to remove the underlying metal catalyst [200]. While there remains a possibility that the graphene may be damaged during the transfer process, the observation of a low I(D)/I(G) ratio of graphene on Ni foil compared to the D peak of the same graphene film upon transferring to SiO_2/Si provides some support for the hypothesis of acid induced damage. However, in comparing our film to graphene films formed by chemical routes, the Raman the I(D)/I(G) is still lower [201] and is comparable to graphene grown by the more commonly reported hot wall CVD method [103-104].

The position of the Raman 2D peak is also higher compared to exfoliated graphene from HOPG (~ 2640 cm^{-1}) but is still consistent with other reported CVD grown graphene [104, 106]. One reason for the difference in the thermal expansion between graphene and Ni during the cooling stage causes a strain in the graphene lattice, resulting in a shift in Raman 2D's peak position [202]. There have been other reports that cite the doping of graphene by HNO_3 (a component in our commercial Ni etchant solution) [71] and the substrate effect [203] as additional causes contributing to this shift.

It is also observed that the graphene film also exhibits Raman spectra characteristic of a few layered graphene at other sites, indicating that the film is not a single layer at all sites. It is also observed that in some of these sites, the Raman 2D peak exhibits a single Lorentzian peak but with a wider FWHM (up to ~ 70 cm^{-1}). It has been argued that CVD grown few-layers graphene may exhibit characteristics similar to turbostratic graphene resulting from the absence of long term order in the c axis as compared to HOPG's ordered AB stacking [113, 125, 204]. To further investigate this observation, selected area electron diffraction (SAED) patterns of the graphene film on a TEM holey

carbon grid were obtained (Figure 7.7). This confirms the earlier observations that the PT-CVD grown film has the hexagonal symmetry that is characteristic of graphitic material as there is in general, a lack of ring-like diffraction patterns which are associated with random stacking in either amorphous polycrystalline or thick graphitic carbons.

The existence of faint secondary diffraction spots (as indicated by the arrow) may be attributed to mis-orientation between adjacent layers providing further support to the turbostratic nature of the PT-CVD grown few layered graphene [104]. However, the possibility that this may also be a result of the electron beam damage during electron microscopic analysis cannot be dismissed, as the electron beam incidence is not perpendicular to the sample. The implication of a non-AB stacking bilayer and few layer graphene may indicate that the electronic properties are actually similar to single layer graphene.

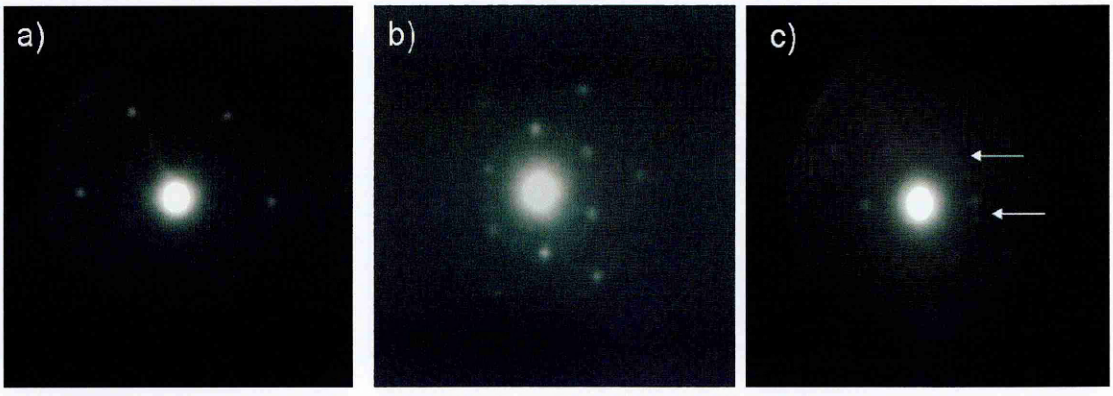

***Figure 7.7**: The electron diffraction patterns (SAED) measured at three random points of a graphene film on a TEM holey carbon grid, showed the hexagonal symmetry that is characteristic of graphitic materials. Note the secondary diffraction spots (arrows in image c) may have been resulted from mis-orientation of adjacent graphene layers indicating that the CVD growth few layer graphene may be turbostratic.*

It has been previously noted that using hot wall CVD for graphene growth, the cooling rate was deemed to be critical in controlling the number of graphene layers formed on the Ni surface. The PT-CVD system exhibits a nominal cooling rate of ~100°C/min under the flow of H_2 and Ar. While this cooling rate is an order of magnitude faster

than the more commonly reported rate of ~ 10°C/min for standard thermal CVD [103], there is no observe of large Raman D peak which have been previously attributed as a manifestation of rapid cooling (> 20°C/min) that did not allow sufficient time for carbon to diffuse to the surface and achieve better crystallinity in time [103]. It is noted that since the growth process reported in this section is essentially in non-thermal equilibrium (i.e. thermal energy is rapidly applied and withdraw without the entire system reaching thermal equilibrium) unlike standard thermal CVD, a direct comparison between the two different processes may not be completely accurate.

To further characterize and illustrate the potentials of the graphene film's electrical and optical properties, fabrication of an organic solar cell (OPVs) using the pristine (non-chemically modified) graphene was also performed. Previous works [180, 205] have indicated that the hydrophobic nature of pristine graphene and its inherently higher sheet resistance [4] can hinder the performance of graphene based OPV cells unless additional method like chemical modification of graphene with PBASE [180], $AgCl_3$ [205] and HCL/HNO_3 compounds [200] are used. These chemicals were reported to have improved both the conductivity of graphene and reducing the hydrophobicity. Since the aim was to establish if the PT-CVD grown pristine graphene can have comparable performance to graphene grown using standard thermal CVD, no process optimizations were taken to maximize the OPV's performance.

Investigation of the optical transmission of the graphene film was measured by transferring the as-grown film onto a glass substrate using the PMMA technique as before and then examined using UV-VIS absorption/transmission studies. It is observed that the optical transmission of the graphene film is above 90% within the range 300 to 800 nm which is a significant improvement over ITO (Figure 7.8a) [69]. The sheet resistance of the graphene film was also measured to be ~ 790 Ω/sq (Kulicke and Soffa four point measurement system). This falls within the range of the previously reported sheet resistance values [69, 106].

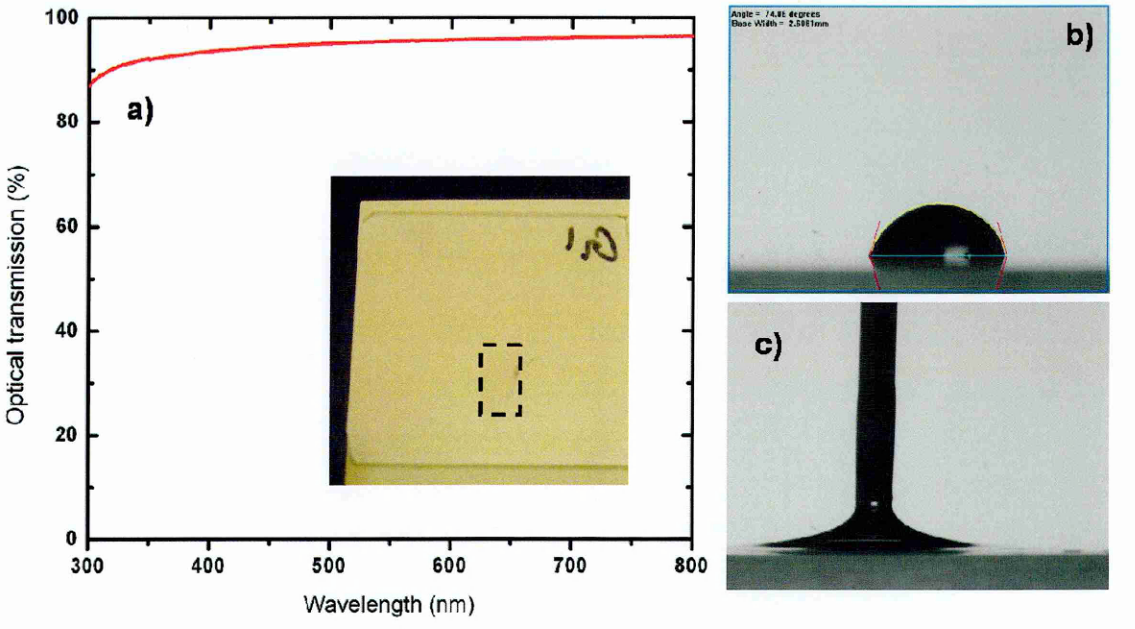

***Figure 7.8**: a) Optical transmission measurement of graphene on glass substrate using UV-VIS setup; b) shows the hydrophobic nature of graphene surface (transferred onto a glass substrate) with water versus c) the good wetting of ethanol. Inset in a) shows the optical image of graphene on glass substrate, lying on a yellow notepad. The area of graphene is ~ 6 mm x 5 mm, as highlighted by the dotted boundary.*

Investigations into using CVD grown graphene as OPV's transparent electrode have been reported earlier using both bulk hetero-junction and bilayer OPV structures [26]. In both cases, PEDOT:PSS has been utilized as a hole transport/planarising layer [206]. As mentioned, one common issue is that graphene surface tends to be hydrophobic thus spin-coating of PEDOT-PSS on the surface faces considerable difficulty. One method to minimize this issue is by utilizing an ethanol/PEDOT:PSS (1:3) solution for the spin coating process instead of just spin-coating with the original water based PEDOT:PSS solution. This is illustrated by Figure 7.8b and c. Clearly, ethanol wets graphene better than water, reinforcing the hydrophobic nature of graphene. In relationship to the OPV device, PEDOT:PSS has two roles: 1) acting as a hole transport layer in general, and 2) PEDOT:PSS also act as a reasonable planarising material for graphene.

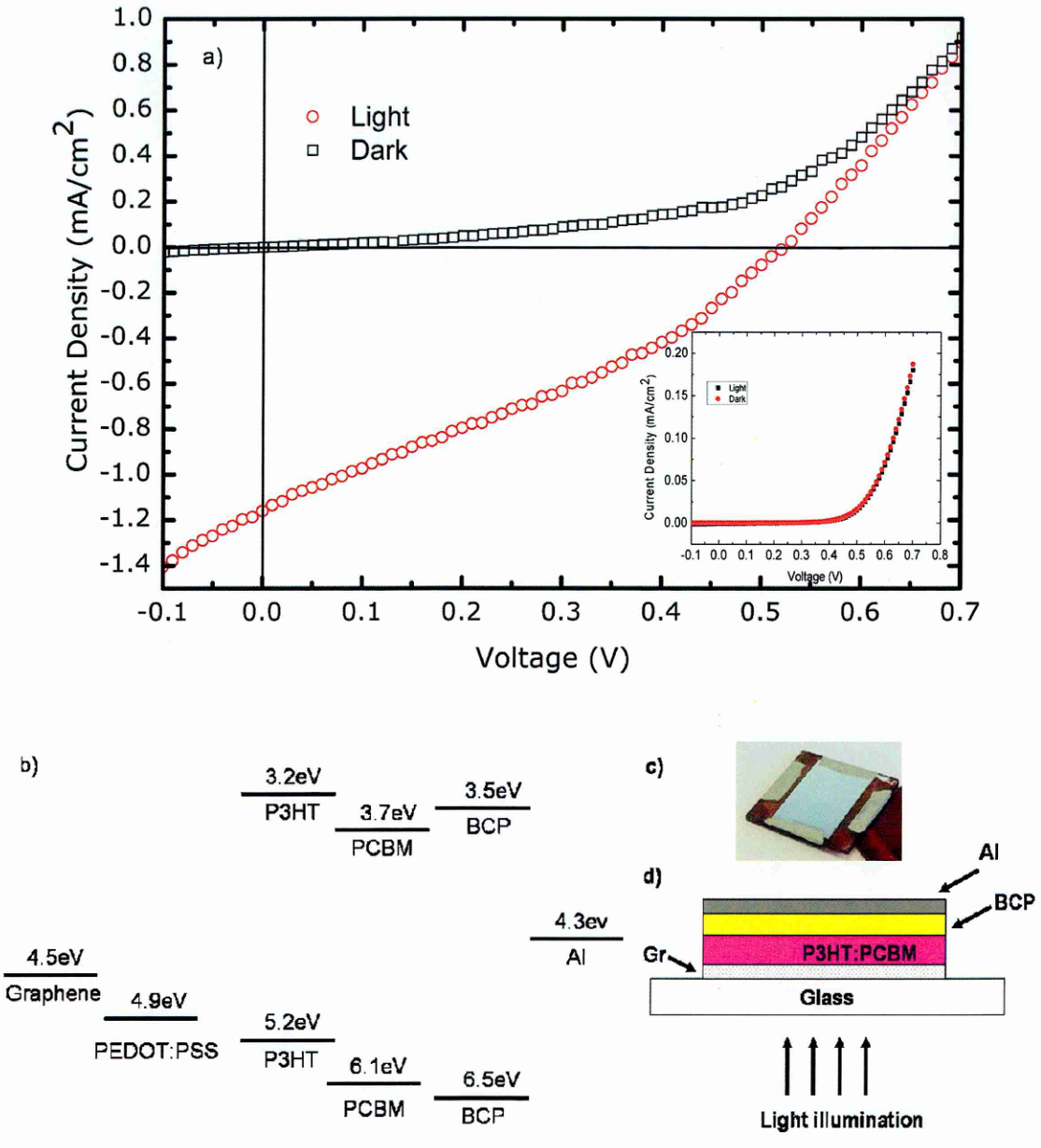

***Figure 7.9**: (a) The J-V characteristics of OPV cell fabricated using graphene as transparent electrode (graphene/PEDOT:PSS/P3HT:PCBM/BCP/Al) under dark and light AM 1.5G conditions. (Inset) shows the J-V characteristics of a 'reference' OPV cell of PEDOT:PSS/P3HT:PCBM/BCP/Al. b) The proposed flat band diagram for the device incorporating graphene as an electrode. c) shows a photograph of the OPV graphene device with d) the corresponding schematic of the device.*

Figure 7.9 shows the *J-V* characteristics of the graphene electrode based OPV, with the inset showing the PEDOT:PSS reference. The performance parameters are summarized in Table 7.1. The graphene electrode based device shows 0.2% efficiency, which is comparable to other reported result that uses CVD grown pristine graphene on a similar

OPV device structure[180]. It has been previously reported that PEDOT:PSS has been experimented as an transparent electrode in solar cell[206]. To ensure that the photovoltaic effect observed in the graphene OPV cell is not due to PEDOT:PSS layer acting as the transparent electrode in place of graphene, another OPV cell structure is also fabricated: PEDOT:PSS/P3HT:PCBM/BCP/Al on glass substrates. As seen in Figure 7.9 inset, there is no observable difference in the *J-V* characteristics under both dark and light illumination, thus indicating the role of graphene as the transparent electrode for the OPV. This also implies that it is unlikely the spin-coated PEDOT:PSS used in this study improve the conductivity of graphene electrode. As seen later in the section, the poor conductivity of graphene is deemed to be a factor in OPV's low efficiency.

Table 7.1: *Comparison of performance between graphene based OPV against a control device without graphene. The area of the OPV is 0.032 cm^2. Compared to a device consisting of PEDOT and Al electrodes only, the device containing graphene electrode shows an improved performance.*

	Voc	Jsc (mA/cm^2)	FF (%)	η (%)
Glass/Graphene/PEDOT:PSS/P3HT:PCBM/BCP/Al	0.52	1.16	31.5	0.2
Glass/PEDOT:PSS/P3HT:PCBM/BCP/Al	0.26	0.001	26.0	0.0

In comparison, using our previously reported standard ITO based P3HT:PCBM bulk heterojunction solar cell design [189] of 2.5% efficient with open circuit voltage mainly governed by the donor acceptor energy levels ~ 0.6V, and short circuit current densities in excess of 6 $mAcm^{-2}$. From Table 7.1, it can be seen that the short circuit current density is low for the device with the graphene electrode in comparison to the ITO based OPVs, leading to poorer efficiency.

Beside the earlier mentioned issues regarding using graphene as electrodes for OPVs, we can further postulate that the low conversion efficiency can be attributed to a number of other reasons. The work function of graphene (4.5 eV) [207] is lower compared with ITO (4.8 eV) [189], thereby affecting the built in electric field of the

diode, resulting in lower charge collection as well as a slightly lower open circuit voltage. From the J-V curves (figure 7.9a) it can be seen that the shunt resistance of the device is finite (slope at J_{sc}). One factor is that graphene has a relatively poor sheet resistance as compared to ITO, thus this lowers the fill factor which in-turns reduce the device efficiency further. Another possible factor may be a sub-optimal planarising by the PEDOT:PSS layer on graphene, leaving abundant leakage paths for charges during OPV's operation.

7.4 Conclusion

In conclusion, the growth of graphene on Ni using a photo-thermal CVD system (PT-CVD) has been demonstrated. By using PT-CVD system, the overall growth time has been greatly reduced compared to the standard thermal CVD growth technique while still maintaining a comparable quality. This is demonstrated in similar performance in resistance and optical transmission as compared to those reported in literature. Furthermore, investigations into applying the PT-CVD grown graphene film as a transparent electrode for OPV had found comparable performance to other reported pristine graphene based devices. Through this work, it is demonstrated an alternative CVD technology can make mass production of graphene more attractive.

CHAPTER 8

Conclusion and future work

Carbon allotropes consisting of sp^2 hybridization has certainly displayed some of the most fascinating material properties to date. The intrinsically fast charge transport nature of CNT and graphene provided new opportunity for the next generation of high speed nanoelectronics. Other properties like a large surface area to volume ratio meant that both graphene and CNT has the potential to be designed as highly sensitive gas sensors capable of a single molecule detection [130]. While the progress and achievements made over the past decade are great, much remains to be explored. One of the limitations that prevent greater exploitation of graphene and CNT has been the ease of producing these materials in great abundance as well as manipulation and process integration with current technologies to ensure a seamless transition to the next generation of devices. In particular, the needs for a low temperature, fast growth of these nanomaterials remain a significant challenge despite the tremendous progress reported in the literature. This report document the efforts to address the issue of growth of these carbon allotropes using CVD growth tools, especially in the exploration of the potentials in using the photo-thermal CVD (PT-CVD) tool for graphene and CNT growth.

The first work to be performed was through the use of PT-CVD and a bimetallic catalyst of Fe/Ti, it was shown that growth of CNT can reach a rate of approximately 1.3 μm/min at temperatures as low as 370°C. Despite the low temperature of the growth, the CNT quality as examined using Raman spectroscopy and TEM indicated that they are comparable to CNT growth carried out a higher processing temperature. Thus this provided an avenue for the integration of CNT into standard CMOS process using a direct growth process given compatibility in the processing temperature.

Before the attempt to use the PT-CVD system for exploring a graphene growth process, it was felt that it would be necessary to establish the possibility of growing graphene using a standard thermal CVD process available in the present facility to gain an understanding to the nuances of a graphene growth process. After demonstrating a graphene growth process using copper catalysts, the films were characterized. In terms of applications of the graphene film, different FET structures were explored. The first area of work surrounds the studies on polymeric gate dielectric as alternative to the common SiO_2 in an attempt to explore graphene FET in the area of organic FET due to its superior mobility in comparison to current organic semiconductor materials. There is a noted difference in the performance of graphene FET by merely switching the gate dielectric from SiO_2 to PVP. This is because graphene is highly sensitive to charge impurity and surface roughness at the graphene/dielectric interface. Thus any graphene FET design has considered all these factors to optimize the performance.

The next area of work surrounds a novel device structure based on the combination of graphene on DLC layer using Si as a back-gate for electrical modulation. This 3 terminal pseudo-FET exhibited saturable behaviour in the transfer characteristic (I_{DS}-V_{GS} curve) despite the fact that graphene is known to be a zero bandgap semiconductor material. The mechanism causing this may be attributed to the heterojunction DLC-Si structure supporting the graphene layer. The DLC-Si structure provided a mechanism to inject into or extract charges from the graphene layer as we swept the gate voltage of this pseudo-FET device.

Finally, it was demonstrated that the PT-CVD process was able to be adopted for graphene growth. Due to the non thermal equilibrium of the PT-CVD process, we can perform the graphene growth with three distinctive features: fast annealing, short duration of hydrocarbon feedstock and fast cooling time that does not have observable negative impact on graphene growth when compared to a standard thermal CVD growth process. As part of the investigation into the optical and electronic properties of

the graphene grown via this method, a demonstration of the graphene's quality is through the application of these graphene as transparent electrodes for organic solar cell (OPV) purpose. Previously, standard thermal CVD grown graphene was used in bulk heterojunction OPV with P3HT/PCBM as the active layer. It was found that the graphene electrode based OPV's performance is comparable with those reported in the literature.

8.1 Future work

Beyond the works documented in this report on the growth of graphene and CNT under various conditions as well as explore into their applications, there are areas that one could engage in the future. In the area of CNT interconnect conductors, while demonstration on the growth of MWCNT at CMOS compatible processing temperature was achieved, the area of low temperature growth of SWCNT remains a challenge. It has been argued that ballistic transport in SWCNT would be more readily achievable compared to MWCNT [208], thus implying even better conductivity. Works on low temperature SWCNT growth using PECVD process shows promising results with reported growth temperature ~ 450 ^{o}C [209]. The key is to use a combination of suitable catalysts with the introduction of water vapour into the process that will enhance the selectivity of SWCNT growth over MWCNT and other carbon materials.

In the area of CVD graphene growth, this work presents the investigations which indicated that growth at 700 ^{o}C had been realised. To further graphene's integration with present microelectronic technologies, efforts should be directed at lower temperature growth. From published literature mentioned in previous chapters and the experience in the area of low temperature CNT growth showed that certain combinations of a suitable carbon feedstock with low pyrolysis, plasma energy and rapid non-equilibrium thermal heating can create a suitable condition for low

temperature growth. Thus an area to focus on is the introduction of a DC/RF energy into the photo-thermal CVD process may help to promote graphene growth at low temperature.

Finally in the area of CNT and graphene electrodes, an area of interest is in the interfacial charge injection process between graphene/CNT with other materials. Organic materials are especially of interest given that one major area of applications for graphene and CNT electrodes are in the area of organic electronics as mentioned in this thesis. While there have been some reported studies [174, 210], many remains to be investigated on the impact of these carbon based electrodes.

References

[1] H. Dai, A. Javey, E. Pop, D. Mann and Y. Lu, "Electrical Transport Properties and Field-Effect Transistors of Carbon Nanotubes," *Nano,* vol. 1, pp. 1-13, 2006.

[2] A. K. Geim, "Graphene: Status and Prospects," *Science,* vol. 324, pp. 1530-1534, June 19, 2009.

[3] ITRS, "http://www.itrs.net/Links/2008ITRS/Home2008.htm " 2008.

[4] F. Bonaccorso, Z. Sun, T. Hasan and A. C. Ferrari, "Graphene photonics and optoelectronics," *Nature Photonics,* vol. 4, pp. 611-622, Sep 2010.

[5] Z. Spitalsky, D. Tasis, K. Papagelis and C. Galiotis, "Carbon nanotube-polymer composites: Chemistry, processing, mechanical and electrical properties," *Progress in Polymer Science,* vol. 35, pp. 357-401, 2010.

[6] G. K. Dimitrakakis, E. Tylianakis and G. E. Froudakis, "Pillared Graphene: A New 3-D Network Nanostructure for Enhanced Hydrogen Storage," *Nano Letters,* vol. 8, pp. 3166-3170, 2008.

[7] F. Ohashi, "Fabrication of Carbon nanotube Devices using Thermal Chemical Vapour Deposition," Doctor of Philosophy, Faculty of Engineering and Physical Sciences, University of Surrey, Guildford, 2009.

[8] R. Saito, G. Dresselhaus and M. S. Dresselhaus, *Physical Properties of Carbon Nanotubes*. London: Imperial College Press, 1998.

[9] S. Iijima, "Helical Microtubules of Graphitic Carbon," *Nature,* vol. 354, pp. 56-58, Nov 7 1991.

[10] P. W. May, "Diamond thin films: a 21st-century material," *Philosophical Transactions of the Royal Society of London Series a-Mathematical Physical and Engineering Sciences,* vol. 358, pp. 473-495, Jan 15 2000.

[11] S. Reich and C. Thomsen, "Raman spectroscopy of graphite," *Philosophical Transactions of the Royal Society a-Mathematical Physical and Engineering Sciences,* vol. 362, pp. 2271-2288, Nov 15 2004.

[12] A. Jorio, R. Saito, G. Dresselhaus and M. S. Dresselhaus, "Determination of nanotubes properties by Raman spectroscopy," *Philosophical Transactions of the Royal Society a-Mathematical Physical and Engineering Sciences,* vol. 362, pp. 2311-2336, Nov 15 2004.

[13] R. Sengupta, M. Bhattacharya, S. Bandyopadhyay and A. K. Bhowmick, "A review on the mechanical and electrical properties of graphite and modified graphite reinforced polymer composites," *Progress in Polymer Science,* vol. 36, pp. 638-670, 2011.

[14] J. U. Lee, P. P. Gipp and C. M. Heller, "Carbon nanotube p-n junction diodes," *Applied Physics Letters,* vol. 85, pp. 145-147, Jul 5 2004.

[15] M. S. Fuhrer, J. Nygard, L. Shih, M. Forero, Y. G. Yoon, M. S. C. Mazzoni, H. J. Choi, J. Ihm, S. G. Louie, A. Zettl, and P. L. McEuen, "Crossed nanotube junctions," *Science,* vol. 288, pp. 494-497, Apr 21 2000.

[16] M. S. Fuhrer, B. M. Kim, T. Durkop and T. Brintlinger, "High-mobility nanotube transistor memory," *Nano Letters,* vol. 2, pp. 755-759, Jul 2002.

[17] H. W. C. Postma, T. Teepen, Z. Yao, M. Grifoni and C. Dekker, "Carbon nanotube single-electron transistors at room temperature," *Science,* vol. 293, pp. 76-79, Jul 6 2001.

[18] R. Saito, M. Fujita, G. Dresselhaus and M. S. Dresselhaus, "Electronic-Structure of Graphene Tubules Based on C-60," *Physical Review B,* vol. 46, pp. 1804-1811, Jul 15 1992.

[19] J. W. G. Wildoer, L. C. Venema, A. G. Rinzler, R. E. Smalley and C. Dekker, "Electronic structure of atomically resolved carbon nanotubes," *Nature,* vol. 391, pp. 59-62, Jan 1 1998.

[20] H. Cui, D. Palmer, O. Zhou and B. R. Stoner, *Amorphous and Nanostructured Carbon,* 1999.

[21] W. C. Ren and H. M. Cheng, "Herringbone-type carbon nanofibers with a small diameter and large hollow core synthesized by the catalytic decomposition of methane," *Carbon,* vol. 41, pp. 1657-1660, 2003.

[22] K. P. De Jong and J. W. Geus, "Carbon nanofibers: Catalytic synthesis and applications," *Catalysis Reviews-Science and Engineering,* vol. 42, pp. 481-510, 2000.

[23] T. Guo, P. Nikolaev, A. G. Rinzler, D. Tomanek, D. T. Colbert, and R. E. Smalley, "Self-Assembly of Tubular Fullerenes," *Journal of Physical Chemistry,* vol. 99, pp. 10694-10697, Jul 6 1995.

[24] M. H. Rummeli, E. Borowiak-Palen, T. Gemming, T. Pichler, M. Knupfer, M. Kalbac, L. Dunsch, O. Jost, S. R. P. Silva, W. Pompe, and B. Buchner, "Novel catalysts, room temperature, and the importance of oxygen for the synthesis of single-walled carbon nanotubes," *Nano Letters,* vol. 5, pp. 1209-1215, Jul 2005.

[25] M. Meyyappan, L. Delzeit, A. Cassell and D. Hash, "Carbon nanotube growth by PECVD: a review," *Plasma Sources Science & Technology,* vol. 12, pp. 205-216, May 2003.

[26] P. Avouris, J. Appenzeller, R. Martel and S. J. Wind, "Carbon nanotube electronics," *Proceedings of the Ieee,* vol. 91, pp. 1772-1784, Nov 2003.

[27] J. Kong, C. Zhou, A. Morpurgo, H. T. Soh, C. F. Quate, C. Marcus, and H. Dai, "Synthesis, integration, and electrical properties of individual single-walled carbon nanotubes," *Applied Physics a-Materials Science & Processing,* vol. 69, pp. 305-308, Sep 1999.

[28] N. R. Franklin and H. J. Dai, "An enhanced CVD approach to extensive nanotube networks with directionality," *Advanced Materials,* vol. 12, pp. 890-894, Jun 16 2000.

[29] J. B. K. Law, C. K. Koo and J. T. L. Thong, "Horizontally directed growth of carbon nanotubes utilizing self-generated electric field from plasma induced surface charging," *Applied Physics Letters,* vol. 91, Dec 10 2007.

[30] J. F. AuBuchon, L. H. Chen, A. I. Gapin and S. H. Jin, "Electric-field-guided growth of carbon nanotubes during DC plasma-enhanced CVD," *Chemical Vapor Deposition,* vol. 12, pp. 370-374, Jun 2006.

[31] K. Kasuya, K. Nagato, Y. Jin, H. Morii, T. Ooi, and M. Nakao, "Rapid and localized synthesis of single-walled carbon nanotubes on flat surface by laser-assisted chemical vapor deposition," *Japanese Journal of Applied Physics Part 2-Letters & Express Letters,* vol. 46, pp. L333-L335, Apr 2007.

[32] R. T. K. Baker and P. S. Harris, *Formation of filamentuous carbon* vol. 14. New york: Marcel Dekker, 1978.

[33] S. B. Sinnott, R. Andrews, D. Qian, A. M. Rao, Z. Mao, E. C. Dickey, and F. Derbyshire, "Model of carbon nanotube growth through chemical vapor deposition," *Chemical Physics Letters,* vol. 315, pp. 25-30, Dec 17 1999.

[34] R. S. Wagner and W. C. Ellis, "Vapor-Liquid-Solid Mechanism of Single Crystal Growth," *Applied Physics Letters,* vol. 4, pp. 89-91, 1964.

[35] G. G. Tibbetts, "Carbon-Fibers Produced by Pyrolysis of Natural-Gas in Stainless-Steel Tubes," *Applied Physics Letters,* vol. 42, pp. 666-668, 1983.

[36] S. Helveg, C. Lopez-Cartes, J. Sehested, P. L. Hansen, B. S. Clausen, J. R. Rostrup-Nielsen, F. Abild-Pedersen, and J. K. Norskov, "Atomic-scale imaging of carbon nanofibre growth," *Nature,* vol. 427, pp. 426-429, Jan 29 2004.

[37] V. Stolojan, Y. Tison, G. Y. Chen and R. Silva, "Controlled growth-reversal of catalytic carbon nanotubes under electron-beam irradiation," *Nano Letters,* vol. 6, pp. 1837-1841, Sep 13 2006.

[38] H. J. Dai, A. G. Rinzler, P. Nikolaev, A. Thess, D. T. Colbert, and R. E. Smalley, "Single-wall nanotubes produced by metal-catalyzed disproportionation of carbon monoxide," *Chemical Physics Letters,* vol. 260, pp. 471-475, Sep 27 1996.

[39] Y. Li, W. Kim, Y. Zhang, M. Rolandi, D. Wang, and H. Dai, "Growth of Single-Walled Carbon Nanotubes from Discrete Catalytic Nanoparticles of Various Sizes," *The Journal of Physical Chemistry B,* vol. 105, pp. 11424-11431, Nov 2001.

[40] A. Moisala, A. G. Nasibulin and E. I. Kauppinen, "The role of metal nanoparticles in the catalytic production of single-walled carbon nanotubes - a review," *Journal of Physics-Condensed Matter,* vol. 15, pp. S3011-S3035, Oct 29 2003.

[41] R. Sen, A. Govindaraj and C. N. R. Rao, "Carbon nanotubes by the metallocene route," *Chemical Physics Letters,* vol. 267, pp. 276-280, Mar 21 1997.

[42] H. C. Choi, S. Kundaria, D. W. Wang, A. Javey, Q. Wang, M. Rolandi, and H. J. Dai, "Efficient formation of iron nanoparticle catalysts on silicon oxide by hydroxylamine for carbon nanotube synthesis and electronics," *Nano Letters,* vol. 3, pp. 157-161, Feb 2003.

[43] A. C. Dupuis, "The catalyst in the CCVD of carbon nanotubes - a review," *Progress in Materials Science,* vol. 50, pp. 929-961, Nov 2005.

[44] Y. Homma, Y. Kobayashi, T. Ogino, D. Takagi, R. Ito, Y. J. Jung, and P. M. Ajayan, "Role of Transition Metal Catalysts in Single-Walled Carbon Nanotube Growth in

Chemical Vapor Deposition," *The Journal of Physical Chemistry B,* vol. 107, pp. 12161-12164, 2003/11/01 2003.

[45] R. L. Vander Wal, T. M. Ticich and V. E. Curtis, "Substrate–support interactions in metal-catalyzed carbon nanofiber growth," *Carbon,* vol. 39, pp. 2277-2289, 2001.

[46] P. R. Wallace, "The Band Theory of Graphite," *Physical Review,* vol. 71, pp. 622-634, 1947.

[47] J. W. Mcclure, "Theory of Diamagnetism and Electron-Spin Resonance of Graphite Ribbons," *Bulletin of the American Physical Society,* vol. 26, pp. 484-484, 1981.

[48] K. S. Novoselov, D. Jiang, F. Schedin, T. J. Booth, V. V. Khotkevich, S. V. Morozov, and A. K. Geim, "Two-dimensional atomic crystals," *Proceedings of the National Academy of Sciences of the United States of America,* vol. 102, pp. 10451-10453, July 26, 2005.

[49] K. S. Novoselov, A. K. Geim, S. V. Morozov, D. Jiang, Y. Zhang, S. V. Dubonos, G. IV, and A. A. Firsov, "Electric field effect in atomically thin carbon films," *Science,* vol. 306, pp. 666-669, Oct 22 2004.

[50] Y. Zhang, Y.-W. Tan, H. L. Stormer and P. Kim, "Experimental observation of the quantum Hall effect and Berry's phase in graphene," *Nature,* vol. 438, pp. 201-204, 2005.

[51] F. Schwierz, "Graphene transistors," *Nat Nano,* vol. 5, pp. 487-496, 2010.

[52] J. H. Chen, C. Jang, M. Ishigami, S. Xiao, W. G. Cullen, M. S. Fuhrer, and E. D. Williams, "Diffusive charge transport in graphene on SiO_2," *Solid State Communications,* vol. 149, pp. 1080-1086, Jul 2009.

[53] D. B. Farmer, H.-Y. Chiu, Y.-M. Lin, K. A. Jenkins, F. Xia, and P. Avouris, "Utilization of a Buffered Dielectric to Achieve High Field-Effect Carrier Mobility in Graphene Transistors," *Nano Letters,* vol. 9, pp. 4474-4478, 2009/12/09 2009.

[54] S. Kim, J. Nah, I. Jo, D. Shahrjerdi, L. Colombo, Z. Yao, E. Tutuc, and S. K. Banerjee, "Realization of a high mobility dual-gated graphene field-effect transistor with Al_2O_3 dielectric," *Applied Physics Letters,* vol. 94, p. 062107, 2009.

[55] J. H. Chen, C. Jang, S. Adam, M. S. Fuhrer, E. D. Williams, and M. Ishigami, "Charged-impurity scattering in graphene," *Nature Physics,* vol. 4, pp. 377-381, May 2008.

[56] A. K. Geim and K. S. Novoselov, "The rise of graphene," *Nat Mater,* vol. 6, pp. 183-191, 2007.

[57] Y. W. Tan, Y. Zhang, K. Bolotin, Y. Zhao, S. Adam, E. H. Hwang, S. Das Sarma, H. L. Stormer, and P. Kim, "Measurement of Scattering Rate and Minimum Conductivity in Graphene," *Physical Review Letters,* vol. 99, p. 246803, 2007.

[58] V. V. Cheianov and V. I. Fal'ko, "Friedel Oscillations, Impurity Scattering, and Temperature Dependence of Resistivity in Graphene," *Physical Review Letters,* vol. 97, p. 226801, 2006.

[59] S. Adam, E. H. Hwang, V. M. Galitski and S. Das Sarma, "A self-consistent theory for graphene transport," *Proceedings of the National Academy of Sciences of the United States of America,* vol. 104, pp. 18392-18397, Nov 20 2007.

[60] M. Hentschel and F. Guinea, "Orthogonality catastrophe and Kondo effect in graphene," *Physical Review B,* vol. 76, p. 115407, 2007.

[61] A. Fasolino, J. H. Los and M. I. Katsnelson, "Intrinsic ripples in graphene," *Nat Mater,* vol. 6, pp. 858-861, 2007.

[62] T. Stauber, N. M. R. Peres and F. Guinea, "Electronic transport in graphene: A semiclassical approach including midgap states," *Physical Review B,* vol. 76, p. 205423, 2007.

[63] S. Fratini and F. Guinea, "Substrate-limited electron dynamics in graphene," *Physical Review B,* vol. 77, p. 195415, 2008.

[64] Y. M. Lin, Y. Q. Wu, A. A. Bol, K. A. Jenkins, F. N. Xia, D. B. Farmer, Y. Zhu, and P. Avouris, "High-frequency, scaled graphene transistors on diamond-like carbon," *Nature,* vol. 472, pp. 74-78, Apr 7 2011.

[65] H. Wang, D. Nezich, J. Kong and T. Palacios, "Graphene Frequency Multipliers," *Ieee Electron Device Letters,* vol. 30, pp. 547-549, May 2009.

[66] N. Harada, K. Yagi, S. Sato and N. Yokoyama, "A polarity-controllable graphene inverter," *Applied Physics Letters,* vol. 96, Jan 4 2010.

[67] R. Sordan, F. Traversi and V. Russo, "Logic gates with a single graphene transistor," *Applied Physics Letters,* vol. 94, pp. 073305-3, 2009.

[68] A. B. Kuzmenko, E. van Heumen, F. Carbone and D. van der Marel, "Universal Optical Conductance of Graphite," *Physical Review Letters,* vol. 100, p. 117401, 2008.

[69] X. S. Li, Y. W. Zhu, W. W. Cai, M. Borysiak, B. Y. Han, D. Chen, R. D. Piner, L. Colombo, and R. S. Ruoff, "Transfer of Large-Area Graphene Films for High-Performance Transparent Conductive Electrodes," *Nano Letters,* vol. 9, pp. 4359-4363, Dec 2009.

[70] E. Stolyarova, D. Stolyarov, K. Bolotin, S. Ryu, L. Liu, K. T. Rim, M. Klima, M. Hybertsen, I. Pogorelsky, I. Pavlishin, K. Kusche, J. Hone, P. Kim, H. L. Stormer, V. Yakimenko, and G. Flynn, "Observation of Graphene Bubbles and Effective Mass Transport under Graphene Films," *Nano Letters,* vol. 9, pp. 332-337, Dec 2008.

[71] S. Bae, H. Kim, Y. Lee, X. F. Xu, J. S. Park, Y. Zheng, J. Balakrishnan, T. Lei, H. R. Kim, Y. I. Song, Y. J. Kim, K. S. Kim, B. Ozyilmaz, J. H. Ahn, B. H. Hong, and S. Iijima, "Roll-to-roll production of 30-inch graphene films for transparent electrodes," *Nature Nanotechnology,* vol. 5, pp. 574-578, Aug 2010.

[72] F. Schwierz, "Graphene transistors," *Nature Nanotechnology,* vol. 5, pp. 487-496, Jul 2010.

[73] Y. Taur and T. Ning, *Fundamentals of Modern VLSI Devices*: Cambridge University Press, 1998.

[74] D. J. Frank, Y. Taur and H. S. P. Wong, "Generalized scale length for two-dimensional effects in MOSFET's," *Ieee Electron Device Letters,* vol. 19, pp. 385-387, Oct 1998.

[75] S. K. Banerjee, L. F. Register, E. Tutuc, D. Basu, S. Kim, D. Reddy, and A. H. MacDonald, "Graphene for CMOS and Beyond CMOS Applications," *Proceedings of the Ieee,* vol. 98, pp. 2032-2046, Dec 2010.

[76] M. I. Katsnelson, K. S. Novoselov and A. K. Geim, "Chiral tunnelling and the Klein paradox in graphene," *Nature Physics,* vol. 2, pp. 620-625, 2006.

[77] M. C. Lemme, T. J. Echtermeyer, M. Baus and H. Kurz, "A graphene field-effect device," *Ieee Electron Device Letters,* vol. 28, pp. 282-284, Apr 2007.

[78] F. N. Xia, D. B. Farmer, Y. M. Lin and P. Avouris, "Graphene Field-Effect Transistors with High On/Off Current Ratio and Large Transport Band Gap at Room Temperature," *Nano Letters,* vol. 10, pp. 715-718, Feb 2010.

[79] J. B. Oostinga, H. B. Heersche, X. Liu, A. F. Morpurgo and L. M. K. Vandersypen, "Gate-induced insulating state in bilayer graphene devices," *Nat Mater,* vol. 7, pp. 151-157, 2008.

[80] M. Y. Han, B. Özyilmaz, Y. Zhang and P. Kim, "Energy Band-Gap Engineering of Graphene Nanoribbons," *Physical Review Letters,* vol. 98, p. 206805, 2007.

[81] Y. M. Lin, K. Jenkins, D. Farmer, A. Valdes-Garcia, P. Avouris, C. Y. Sung, H. Y. Chiu, and B. Ek, "Development of Graphene FETs for High Frequency Electronics," *2009 Ieee International Electron Devices Meeting,* pp. 216-219, 2009.

[82] K. Kim, J. Y. Choi, T. Kim, S. H. Cho and H. J. Chung, "A role for graphene in silicon-based semiconductor devices," *Nature,* vol. 479, pp. 338-344, Nov 17 2011.

[83] F. Schwierz, "Electronics: Industry-compatible graphene transistors," *Nature,* vol. 472, pp. 41-42, 2011.

[84] Y. Q. Wu, Y. M. Lin, K. A. Jenkins, J. A. Ott, C. Dimitrakopoulos, D. B. Farmer, F. Xia, A. Grill, D. A. Antoniadis, and P. Avouris, "RF Performance of Short Channel Graphene Field-Effect Transistor," *2010 International Electron Devices Meeting - Technical Digest,* 2010.

[85] X. Liang, Z. Fu and S. Y. Chou, "Graphene transistors fabricated via transfer-printing in device active-areas on large wafer," *Nano Letters,* vol. 7, pp. 3840-3844, Dec 2007.

[86] D. S. Li, W. Windl and N. P. Padture, "Toward Site-Specific Stamping of Graphene," *Advanced Materials,* vol. 21, p. 1243, Mar 26 2009.

[87] X. G. Liang, A. S. P. Chang, Y. G. Zhang, B. D. Harteneck, H. Choo, D. L. Olynick, and S. Cabrini, "Electrostatic Force Assisted Exfoliation of Prepatterned Few-Layer Graphenes into Device Sites," *Nano Letters,* vol. 9, pp. 919-919, Feb 2009.

[88] W. S. Hummers and R. E. Offeman, "Preparation of Graphitic Oxide," *Journal of the American Chemical Society,* vol. 80, pp. 1339-1339, 1958.

[89] S. Park and R. S. Ruoff, "Chemical methods for the production of graphenes," *Nature Nanotechnology,* vol. 4, pp. 217-224, Apr 2009.

[90] S. Stankovich, D. A. Dikin, R. D. Piner, K. A. Kohlhaas, A. Kleinhammes, Y. Jia, Y. Wu, S. T. Nguyen, and R. S. Ruoff, "Synthesis of graphene-based nanosheets via

chemical reduction of exfoliated graphite oxide," *Carbon,* vol. 45, pp. 1558-1565, Jun 2007.

[91] P. Sutter, "Epitaxial Graphene - How silicon leaves the scene," *Nature Materials,* vol. 8, pp. 171-172, Mar 2009.

[92] C. Berger, Z. M. Song, T. B. Li, X. B. Li, A. Y. Ogbazghi, R. Feng, Z. T. Dai, A. N. Marchenkov, E. H. Conrad, P. N. First, and W. A. de Heer, "Ultrathin epitaxial graphite: 2D electron gas properties and a route toward graphene-based nanoelectronics," *Journal of Physical Chemistry B,* vol. 108, pp. 19912-19916, Dec 30 2004.

[93] J. Hass, W. A. de Heer and E. H. Conrad, "The growth and morphology of epitaxial multilayer graphene," *Journal of Physics-Condensed Matter,* vol. 20, Aug 13 2008.

[94] A. T. N'Diaye, S. Bleikamp, P. J. Feibelman and T. Michely, "Two-Dimensional Ir Cluster Lattice on a Graphene Moire on Ir(111)," *Physical Review Letters,* vol. 101, Nov 21 2008.

[95] P. W. Sutter, J. I. Flege and E. A. Sutter, "Epitaxial graphene on ruthenium," *Nature Materials,* vol. 7, pp. 406-411, May 2008.

[96] D. E. Starr, E. M. Pazhetnov, A. I. Stadnichenko, S. K. Shaikhutdinov and A. I. Boronin, "Carbon films grown on Pt(111) as supports for model gold catalysts," *Surface Science,* vol. 600, pp. 2688-2695, Jul 1 2006.

[97] R. Rosei, M. Decrescenzi, F. Sette, C. Quaresima, A. Savoia, and P. Perfetti, "Structure of Graphitic Carbon on Ni(111) - a Surface Extended-Energy-Loss Fine-Structure Study," *Physical Review B,* vol. 28, pp. 1161-1164, 1983.

[98] T. Aizawa, R. Souda, S. Otani, Y. Ishizawa and C. Oshima, "Anomalous Bond of Monolayer Graphite on Transition-Metal Carbide Surfaces," *Physical Review Letters,* vol. 64, pp. 768-771, Feb 12 1990.

[99] B. C. Banerjee, P. L. Walker and T. J. Hirt, "Pyrolytic Carbon Formation from Carbon Suboxide," *Nature,* vol. 192, 1961.

[100] M. Eizenberg and J. M. Blakely, "Carbon Monolayer Phase Condensation on Ni(111)," *Surface Science,* vol. 82, pp. 228-236, 1979.

[101] L. C. Isett and J. M. Blakely, "Segregation Isosteres for Carbon at (100) Surface of Nickel," *Surface Science,* vol. 58, pp. 397-414, 1976.

[102] E. Loginova, N. C. Bartelt, P. J. Feibelman and K. F. McCarty, "Evidence for graphene growth by C cluster attachment," *New Journal of Physics,* vol. 10, Sep 25 2008.

[103] Q. K. Yu, J. Lian, S. Siriponglert, H. Li, Y. P. Chen, and S. S. Pei, "Graphene segregated on Ni surfaces and transferred to insulators," *Applied Physics Letters,* vol. 93, Sep 15 2008.

[104] A. Reina, X. T. Jia, J. Ho, D. Nezich, H. B. Son, V. Bulovic, M. S. Dresselhaus, and J. Kong, "Large Area, Few-Layer Graphene Films on Arbitrary Substrates by Chemical Vapor Deposition," *Nano Letters,* vol. 9, pp. 30-35, Jan 2009.

[105] L. G. De Arco, Y. Zhang, A. Kumar and C. W. Zhou, "Synthesis, Transfer, and Devices of Single- and Few-Layer Graphene by Chemical Vapor Deposition," *Ieee Transactions on Nanotechnology,* vol. 8, pp. 135-138, Mar 2009.

[106] X. S. Li, W. W. Cai, J. H. An, S. Kim, J. Nah, D. X. Yang, R. Piner, A. Velamakanni, I. Jung, E. Tutuc, S. K. Banerjee, L. Colombo, and R. S. Ruoff, "Large-Area Synthesis of High-Quality and Uniform Graphene Films on Copper Foils," *Science,* vol. 324, pp. 1312-1314, Jun 5 2009.

[107] H. I. Rasool, E. B. Song, M. J. Allen, J. K. Wassei, R. B. Kaner, K. L. Wang, B. H. Weiller, and J. K. Gimzewski, "Continuity of Graphene on Polycrystalline Copper," *Nano Letters,* vol. 11, pp. 251-256, Jan 2011.

[108] X. S. Li, W. W. Cai, L. Colombo and R. S. Ruoff, "Evolution of Graphene Growth on Ni and Cu by Carbon Isotope Labeling," *Nano Letters,* vol. 9, pp. 4268-4272, Dec 2009.

[109] A. Reina, S. Thiele, X. T. Jia, S. Bhaviripudi, M. S. Dresselhaus, J. A. Schaefer, and J. Kong, "Growth of Large-Area Single- and Bi-Layer Graphene by Controlled Carbon Precipitation on Polycrystalline Ni Surfaces," *Nano Research,* vol. 2, pp. 509-516, Jun 2009.

[110] G. Y. Chen, B. Jensen, V. Stolojan and S. R. P. Silva, "Growth of carbon nanotubes at temperatures compatible with integrated circuit technologies," *Carbon,* vol. 49, pp. 280-285, Jan 2011.

[111] G. Y. Chen, C. H. P. Poa, S. J. Henley, V. Stolojan, S. R. P. Silva, and S. Haq, "Deployment of titanium thermal barrier for low-temperature carbon nanotube growth," *Applied Physics Letters,* vol. 87, Dec 19 2005.

[112] B. Schrader, *Infrared and Raman Spectroscopy: Methods and Applications*: Wiley VCH, 1995.

[113] L. M. Malard, M. S. Dresselhaus, M. A. Pimenta and G. Dresselhaus, "Raman spectroscopy in graphene," *Physics Reports-Review Section of Physics Letters,* vol. 473, pp. 51-87, Apr 2009.

[114] M. S. Dresselhaus, G. Dresselhaus, R. Saito and A. Jorio, "Raman spectroscopy of carbon nanotubes," *Physics Reports-Review Section of Physics Letters,* vol. 409, pp. 47-99, Mar 2005.

[115] A. Jorio, M. A. Pimenta, A. G. S. Filho, R. Saito, G. Dresselhaus, and M. S. Dresselhaus, "Characterizing carbon nanotube samples with resonance Raman scattering," *New Journal of Physics,* vol. 5, p. 139, 2003.

[116] A. Jorio, C. Fantini, M. S. S. Dantas, M. A. Pimenta, A. G. Souza, G. G. Samsonidze, V. W. Brar, G. Dresselhaus, M. S. Dresselhaus, A. K. Swan, M. S. Unlu, B. B. Goldberg, and R. Saito, "Linewidth of the Raman features of individual single-wall carbon nanotubes," *Physical Review B,* vol. 66, Sep 15 2002.

[117] F. Tuinstra and J. L. Koenig, "Raman Spectrum of Graphite," *Journal of Chemical Physics,* vol. 53, pp. 1126-1130, 1970.

[118] Y. J. Lee, "The second order Raman spectroscopy in carbon crystallinity," *Journal of Nuclear Materials,* vol. 325, pp. 174-179, Feb 15 2004.

[119] J. Schwan, V. Batori, S. Ulrich, H. Ehrhardt and S. R. P. Silva, "Nitrogen doping of amorphous carbon thin films," *Journal of Applied Physics,* vol. 84, pp. 2071-2081, Aug 15 1998.

[120] J. Maultzsch, S. Reich, C. Thomsen, S. Webster, R. Czerw, D. L. Carroll, S. M. C. Vieira, P. R. Birkett, and C. A. Rego, "Raman characterization of boron-doped multiwalled carbon nanotubes," *Applied Physics Letters,* vol. 81, pp. 2647-2649, Sep 30 2002.

[121] E. F. Antunes, A. O. Lobo, E. J. Corat, V. J. Trava-Airoldi, A. A. Martin, and C. Verissimo, "Comparative study of first- and second-order Raman spectra of MWCNT at visible and infrared laser excitation," *Carbon,* vol. 44, pp. 2202-2211, Sep 2006.

[122] A. C. Ferrari, "Raman spectroscopy of graphene and graphite: Disorder, electron-phonon coupling, doping and nonadiabatic effects," *Solid State Communications,* vol. 143, pp. 47-57, Jul 2007.

[123] S. Roddaro, P. Pingue, V. Piazza, V. Pellegrini and F. Beltram, "The optical visibility of graphene: Interference colors of ultrathin graphite on SiO(2)," *Nano Letters,* vol. 7, pp. 2707-2710, Sep 2007.

[124] P. Blake, E. W. Hill, A. H. C. Neto, K. S. Novoselov, D. Jiang, R. Yang, T. J. Booth, and A. K. Geim, "Making graphene visible," *Applied Physics Letters,* vol. 91, Aug 6 2007.

[125] L. G. Cancado, K. Takai, T. Enoki, M. Endo, Y. A. Kim, H. Mizusaki, N. L. Speziali, A. Jorio, and M. A. Pimenta, "Measuring the degree of stacking order in graphite by Raman spectroscopy," *Carbon,* vol. 46, pp. 272-275, Feb 2008.

[126] L. G. Cançado, A. Reina, J. Kong and M. S. Dresselhaus, "Geometrical approach for the study of G' band in the Raman spectrum of monolayer graphene, bilayer graphene, and bulk graphite," *Physical Review B,* vol. 77, p. 245408, 2008.

[127] C. Casiraghi, A. Hartschuh, H. Qian, S. Piscanec, C. Georgi, A. Fasoli, K. S. Novoselov, D. M. Basko, and A. C. Ferrari, "Raman Spectroscopy of Graphene Edges," *Nano Letters,* vol. 9, pp. 1433-1441, Apr 2009.

[128] A. C. Ferrari, J. C. Meyer, V. Scardaci, C. Casiraghi, M. Lazzeri, F. Mauri, S. Piscanec, D. Jiang, K. S. Novoselov, S. Roth, and A. K. Geim, "Raman spectrum of graphene and graphene layers," *Physical Review Letters,* vol. 97, Nov 3 2006.

[129] R. J. Nemanich and S. A. Solin, "1st-Order and 2nd-Order Raman-Scattering from Finite-Size Crystals of Graphite," *Physical Review B,* vol. 20, pp. 392-401, 1979.

[130] F. Schedin, A. K. Geim, S. V. Morozov, K. S. Novoselov, E. W. Hill, P. Blake, and M. I. Katsnelson, "Detection of individual gas molecules adsorbed on graphene," *Nature Materials,* vol. 6, pp. 652-655, Sep 2007.

[131] C. Casiraghi, S. Pisana, K. S. Novoselov, A. K. Geim and A. C. Ferrari, "Raman fingerprint of charged impurities in graphene," *Applied Physics Letters,* vol. 91, Dec 3 2007.

[132] B. Krauss, T. Lohmann, D. H. Chae, M. Haluska, K. von Klitzing, and J. H. Smet, "Laser-induced disassembly of a graphene single crystal into a nanocrystalline network," *Physical Review B,* vol. 79, Apr 2009.

[133] M. S. D. Dresselhaus, G.; Avouris, P., *Carbon Nanotubes: Synthesis, Structure, Properties, and Applications*: Springer, 2001.

[134] D. Yokoyama, T. Iwasaki, T. Yoshida, H. Kawarada, S. Sato, T. Hyakushima, M. Nihei, and Y. Awano, "Low temperature grown carbon nanotube interconnects using inner shells by chemical mechanical polishing," *Applied Physics Letters,* vol. 91, Dec 24 2007.

[135] J. Li, Q. Ye, A. Cassell, H. T. Ng, R. Stevens, J. Han, and M. Meyyappan, "Bottom-up approach for carbon nanotube interconnects," *Applied Physics Letters,* vol. 82, pp. 2491-2493, Apr 14 2003.

[136] J. K. Vohs, J. J. Brege, J. E. Raymond, A. E. Brown, G. L. Williams, and B. D. Fahlman, "Low-temperature growth of carbon nanotubes from the catalytic decomposition of carbon tetrachloride," *Journal of the American Chemical Society,* vol. 126, pp. 9936-9937, Aug 18 2004.

[137] T. M. Minea, S. Point, A. Granier and M. Touzeau, "Room temperature synthesis of carbon nanofibers containing nitrogen by plasma-enhanced chemical vapor deposition," *Applied Physics Letters,* vol. 85, pp. 1244-1246, 2004.

[138] W. H. Chiang and R. M. Sankaran, "Synergistic Effects in Bimetallic Nanoparticles for Low Temperature Carbon Nanotube Growth," *Advanced Materials,* vol. 20, pp. 4857-4861, Dec 17 2008.

[139] M. Cantoro, S. Hofmann, S. Pisana, V. Scardaci, A. Parvez, C. Ducati, A. C. Ferrari, A. M. Blackburn, K. Y. Wang, and J. Robertson, "Catalytic chemical vapor deposition of single-wall carbon nanotubes at low temperatures," *Nano Letters,* vol. 6, pp. 1107-1112, Jun 2006.

[140] S. Hofmann, C. Ducati, J. Robertson and B. Kleinsorge, "Low-temperature growth of carbon nanotubes by plasma-enhanced chemical vapor deposition," *Applied Physics Letters,* vol. 83, pp. 135-137, Jul 7 2003.

[141] I. Levchenko, K. Ostrikov, M. Keidar and U. Cvelbar, "Modes of nanotube growth in plasmas and reasons for single-walled structure," *Journal of Physics D-Applied Physics,* vol. 41, Jul 7 2008.

[142] G. D. Nessim, M. Seita, K. P. O'Brien, A. J. Hart, R. K. Bonaparte, R. R. Mitchell, and C. V. Thompson, "Low Temperature Synthesis of Vertically Aligned Carbon Nanotubes with Electrical Contact to Metallic Substrates Enabled by Thermal Decomposition of the Carbon Feedstock," *Nano Letters,* vol. 9, pp. 3398-3405, Oct 2009.

[143] G. Y. Chen, V. Stolojan and S. R. P. Silva, "Top-Down Heating for Low Substrate Temperature Synthesis of Carbon Nanotubes," *Journal of Nanoscience and Nanotechnology,* vol. 10, pp. 3952-3958, Jun 2010.

[144] N. G. Shang, X. Jiang and W. I. Milne, "Tubular graphite cones with single-crystal nanotips and their antioxygenic properties," *Journal of the American Chemical Society,* vol. 129, pp. 8907-8911, Jul 18 2007.

[145] B. O. Boskovic, V. Stolojan, R. U. A. Khan, S. Haq and S. R. P. Silva, "Large-area synthesis of carbon nanofibres at room temperature," *Nature Materials,* vol. 1, pp. 165-168, Nov 2002.

[146] J. Ziebro, I. Lukasiewicz, E. Borowiak-Palen and B. Michalkiewicz, "Low temperature growth of carbon nanotubes from methane catalytic decomposition over nickel supported on a zeolite," *Nanotechnology,* vol. 21, Apr 9 2010.

[147] D. H. Kim, C. D. Kim, H. S. Jang and H. R. Lee, "Low temperature growth of carbon nanotubes in a magnetic field," *Materials Letters,* vol. 61, pp. 2075-2078, Apr 2007.

[148] M. S. Dresselhaus, G. Dresselhaus, A. Jorio, A. G. Souza and R. Saito, "Raman spectroscopy on isolated single wall carbon nanotubes," *Carbon,* vol. 40, pp. 2043-2061, 2002.

[149] K. Sato, R. Saito, Y. Oyama, J. Jiang, L. G. Cancado, M. A. Pimenta, A. Jorio, G. G. Samsonidze, G. Dresselhaus, and M. S. Dresselhaus, "D-band Raman intensity of graphitic materials as a function of laser energy and crystallite size," *Chemical Physics Letters,* vol. 427, pp. 117-121, Aug 18 2006.

[150] N. G. Shang, C. P. Li, W. K. Wong, C. S. Lee, I. Bello, and S. T. Lee, "Microstructure and field emission properties of coral-like carbon nanotubes," *Applied Physics Letters,* vol. 81, pp. 5024-5026, Dec 23 2002.

[151] W. Q. Deng, X. Xu and W. A. Goddard, "A two-stage mechanism of bimetallic catalyzed growth of single-walled carbon nanotubes," *Nano Letters,* vol. 4, pp. 2331-2335, Dec 2004.

[152] Y. Nakayama, L. J. Pan and G. Takeda, "Low-temperature growth of vertically aligned carbon nanotubes using binary catalysts," *Japanese Journal of Applied Physics Part 1-Regular Papers Brief Communications & Review Papers,* vol. 45, pp. 369-371, Jan 2006.

[153] S. Kishimoto, Y. Kojima, Y. Ohno, T. Sugai, H. Shinohara, and T. Mizutani, "Growth of mm-long carbon nanotubes by grid-inserted plasma-enhanced chemical vapor deposition," *Japanese Journal of Applied Physics Part 1-Regular Papers Short Notes & Review Papers,* vol. 44, pp. 1554-1557, Apr 2005.

[154] Z. Bao and J. Locklin, *Organic Field-Effect Transistors*: CRC press, 2007.

[155] C. D. Dimitrakopoulos and P. R. L. Malenfant, "Organic Thin Film Transistors for Large Area Electronics," *Advanced Materials,* vol. 14, pp. 99-117, 2002.

[156] M. E. Roberts, N. r. Queraltó, S. C. B. Mannsfeld, B. N. Reinecke, W. Knoll, and Z. Bao, "Cross-Linked Polymer Gate Dielectric Films for Low-Voltage Organic Transistors," *Chemistry of Materials,* vol. 21, pp. 2292-2299, 2009/06/09 2009.

[157] H. S. Byun, Y. M. Xu and C. K. Song, "Fabrication of high performance pentacene thin film transistors using poly(4-vinylphenol) as the gate insulator on polyethyleneterephthalate substrates," *Thin Solid Films,* vol. 493, pp. 278-281, Dec 22 2005.

[158] J. Kim, J. Jeong, H. D. Cho, C. Lee, S. O. Kim, S. K. Kwon, and Y. Hong, "All-solution-processed bottom-gate organic thin-film transistor with improved subthreshold behaviour using functionalized pentacene active layer," *Journal of Physics D-Applied Physics,* vol. 42, Jun 2009.

[159] A. R. Murphy and J. M. J. Frechet, "Organic semiconducting oligomers for use in thin film transistors," *Chemical Reviews,* vol. 107, pp. 1066-1096, Apr 2007.

[160] S. Bhaviripudi, X. Jia, M. S. Dresselhaus and J. Kong, "Role of Kinetic Factors in Chemical Vapor Deposition Synthesis of Uniform Large Area Graphene Using Copper Catalyst," *Nano Letters,* vol. 10, pp. 4128--4133, Sep 2 2010.

[161] J. Kedzierski, P. L. Hsu, P. Healey, P. W. Wyatt, C. L. Keast, M. Sprinkle, C. Berger, and W. A. de Heer, "Epitaxial graphene transistors on SIC substrates," *IEEE Transactions on Electron Devices,* vol. 55, pp. 2078-2085, Aug 2008.

[162] C. M. Aguirre, P. L. Levesque, M. Paillet, F. Lapointe, B. C. St-Antoine, P. Desjardins, and R. Martel, "The Role of the Oxygen/Water Redox Couple in Suppressing Electron Conduction in Field-Effect Transistors," *Advanced Materials,* vol. 21, pp. 3087-3091, Aug 14 2009.

[163] H. Li, Q. Zhang, C. Liu, S. Xu and P. Gao, "Ambipolar to Unipolar Conversion in Graphene Field-Effect Transistors," *ACS Nano,* vol. 5, pp. 3198-3203, 2011.

[164] D. Haberer, C. E. Giusca, Y. Wang, H. Sachdev, A. V. Fedorov, M. Farjam, S. A. Jafari, D. V. Vyalikh, D. Usachov, X. Liu, U. Treske, M. Grobosch, O. Vilkov, V. K. Adamchuk, S. Irle, S. R. P. Silva, M. Knupfer, B. Büchner, and A. Grüneis, "Evidence for a New Two-Dimensional C4H-Type Polymer Based on Hydrogenated Graphene," *Advanced Materials,* vol. 23, 2011.

[165] D. B. Farmer, R. Golizadeh-Mojarad, V. Perebeinos, Y. M. Lin, G. S. Tulevski, J. C. Tsang, and P. Avouris, "Chemical Doping and Electron-Hole Conduction Asymmetry in Graphene Devices," *Nano Letters,* vol. 9, pp. 388-392, Jan 2009.

[166] N. Park, B. K. Kim, J. O. Lee and J. J. Kim, "Influence of metal work function on the position of the Dirac point of graphene field-effect transistors," *Applied Physics Letters,* vol. 95, Dec 14 2009.

[167] R. Nouchi and K. Tanigaki, "Charge-density depinning at metal contacts of graphene field-effect transistors," *Appl. Phys. Lett.,* vol. 96, p. 253503, 2010.

[168] J. Robertson, "Diamond-like amorphous carbon," *Materials Science & Engineering R-Reports,* vol. 37, pp. 129-281, May 24 2002.

[169] G. A. J. Amaratunga and S. R. P. Silva, "Field emission from a-C:H and a-C:H:N," *Journal of Non-Crystalline Solids,* vol. 198, pp. 611-614, May 1996.

[170] A. Grill, "Electrical and optical properties of diamond-like carbon," *Thin Solid Films,* vol. 355, pp. 189-193, Nov 1999.

[171] G. A. J. Amaratunga, D. E. Segal and D. R. Mckenzie, "Amorphous Diamond-Si Semiconductor Heterojunctions," *Applied Physics Letters,* vol. 59, pp. 69-71, Jul 1 1991.

[172] R. U. A. Khan, A. P. Burden, S. R. P. Silva, J. M. Shannon and B. J. Sealy, "A study of the effects of nitrogen incorporation and annealing on the properties of hydrogenated amorphous carbon films," *Carbon,* vol. 37, pp. 777-780, 1999.

[173] A. C. Ferrari and J. Robertson, "Interpretation of Raman spectra of disordered and amorphous carbon," *Physical Review B,* vol. 61, pp. 14095-14107, May 15 2000.

[174] S. Lee, S. J. Kang, G. Jo, M. Choe, W. Park, J. Yoon, T. Kwon, Y. H. Kahng, D. Y. Kim, B. H. Lee, and T. Lee, "Enhanced characteristics of pentacene field-effect transistors

with graphene electrodes and substrate treatments," *Applied Physics Letters,* vol. 99, Aug 22 2011.

[175] C. A. Di, D. C. Wei, G. Yu, Y. Q. Liu, Y. L. Guo, and D. B. Zhu, "Patterned graphene as source/drain electrodes for bottom-contact organic field-effect transistors," *Advanced Materials,* vol. 20, pp. 3289-3293, Sep 3 2008.

[176] T. Lohmann, K. von Klitzing and J. H. Smet, "Four-Terminal Magneto-Transport in Graphene p-n Junctions Created by Spatially Selective Doping," *Nano Letters,* vol. 9, pp. 1973-1979, May 2009.

[177] M. Collins, R. C. Barklie, J. V. Anguita, J. D. Carey and S. R. P. Silva, "Characterisation of defects in thin films of hydrogenated amorphous carbon," *Diamond and Related Materials,* vol. 9, pp. 781-785, Apr-May 2000.

[178] J. Zhu, R. Jhaveri and J. C. S. Woo, "The effect of traps on the performance of graphene field-effect transistors," *Applied Physics Letters,* vol. 96, May 10 2010.

[179] Y. J. Kang, J. Kang and K. J. Chang, "Electronic structure of graphene and doping effect on SiO(2)," *Physical Review B,* vol. 78, Sep 2008.

[180] Y. Wang, X. H. Chen, Y. L. Zhong, F. R. Zhu and K. P. Loh, "Large area, continuous, few-layered graphene as anodes in organic photovoltaic devices," *Applied Physics Letters,* vol. 95, p. 063302, Aug 10 2009.

[181] N. G. Shang, P. Papakonstantinou, P. Wang, S. Ravi and P. Silva, "Platinum Integrated Graphene for Methanol Fuel Cells," *Journal of Physical Chemistry C,* vol. 114, pp. 15837-15841, Sep 23 2010.

[182] G. Eda, G. Fanchini and M. Chhowalla, "Large-area ultrathin films of reduced graphene oxide as a transparent and flexible electronic material," *Nature Nanotechnology,* vol. 3, pp. 270-274, May 2008.

[183] S. M. Sze and C. Y. Chang, *ULSI technology*: McGraw-Hill, 1996.

[184] M. K. Nazeeruddin, E. Baranoff and M. Gratzel, "Dye-sensitized solar cells: A brief overview," *Solar Energy,* vol. 85, pp. 1172-1178, Jun 2011.

[185] L. M. Chen, Z. R. Hong, G. Li and Y. Yang, "Recent Progress in Polymer Solar Cells: Manipulation of Polymer: Fullerene Morphology and the Formation of Efficient Inverted Polymer Solar Cells," *Advanced Materials,* vol. 21, pp. 1434-1449, Apr 2009.

[186] F. C. Krebs, *Polymeric Solar Cells: Materials, Design, Manufacture.* Lancaster, Pennsylvania: DEStech Publications, 2010.

[187] C. Deibel and V. Dyakonov, "Polymer-fullerene bulk heterojunction solar cells," *Reports on Progress in Physics,* vol. 73, Sep 2010.

[188] *National Instruments - Part ii - photovoltaic cell i-v characterization theory and labview analysis code - Development Zone.* Available: http://zone.ni.com/devzone/cda/tut/p/id/7230

[189] N. A. Nismy, A. A. D. T. Adikaari and S. R. P. Silva, "Functionalized multiwall carbon nanotubes incorporated polymer/fullerene hybrid photovoltaics," *Applied Physics Letters,* vol. 97, Jul 19 2010.

[190] H. Mehrer, *Diffusion in Solids*: Springer, 2007.

[191] H. Yokoyama, H. Numakura and M. Koiwa, "The solubility and diffusion of carbon in palladium," *Acta Materialia,* vol. 46, pp. 2823-2830, 1998.

[192] C. F. Cullis and N. H. Franklin, "The Pyrolysis of Acetylene at Temperatures from 500 to 1000C," *Proceedings of the Royal Society of London. Series A, Mathematical and Physical Sciences,* vol. 280, pp. 139-152, 1964.

[193] O. Nakagoe, N. Takagi and Y. Matsumoto, "Thermal decomposition of acetylene on Pt(111) studied by scanning tunneling microscopy," *Surface Science,* vol. 514, pp. 414-419, 2002.

[194] R. T. Vang, K. Honkala, S. Dahl, E. K. Vestergaard, J. Schnadt, E. Laegsgaard, B. S. Clausen, J. K. Norskov, and F. Besenbacher, "Controlling the catalytic bond-breaking selectivity of Ni surfaces by step blocking," *Nat Mater,* vol. 4, pp. 160-162, 2005.

[195] N. Liu, L. Fu, B. Y. Dai, K. Yan, X. Liu, R. Q. Zhao, Y. F. Zhang, and Z. F. Liu, "Universal Segregation Growth Approach to Wafer-Size Graphene from Non-Noble Metals," *Nano Letters,* vol. 11, pp. 297-303, Jan 2011.

[196] J. Lahiri, T. S. Miller, A. J. Ross, L. Adamska, I. I. Oleynik, and M. Batzill, "Graphene growth and stability at nickel surfaces," *New Journal of Physics,* vol. 13, Feb 3 2011.

[197] H. O. Pierson, *Handbook of Carbon, Graphite, Diamond and Fullerenes*: William Andrew 1994.

[198] T. G. Kollie, "Measurement of Thermal-Expansion Coefficient of Nickel from 300 to 1000 K and Determination of Power-Law Constants near Curie-Temperature," *Physical Review B,* vol. 16, pp. 4872-4881, 1977.

[199] A. Gupta, G. Chen, P. Joshi, S. Tadigadapa and P. C. Eklund, "Raman scattering from high-frequency phonons in supported n-graphene layer films," *Nano Letters,* vol. 6, pp. 2667-2673, Dec 13 2006.

[200] K. S. Kim, Y. Zhao, H. Jang, S. Y. Lee, J. M. Kim, K. S. Kim, J. H. Ahn, P. Kim, J. Y. Choi, and B. H. Hong, "Large-scale pattern growth of graphene films for stretchable transparent electrodes," *Nature,* vol. 457, pp. 706-710, Feb 5 2009.

[201] Y. Si and E. T. Samulski, "Synthesis of water soluble graphene," *Nano Letters,* vol. 8, pp. 1679-1682, Jun 2008.

[202] T. M. G. Mohiuddin, A. Lombardo, R. R. Nair, A. Bonetti, G. Savini, R. Jalil, N. Bonini, D. M. Basko, C. Galiotis, N. Marzari, K. S. Novoselov, A. K. Geim, and A. C. Ferrari, "Uniaxial strain in graphene by Raman spectroscopy: G peak splitting, Gruneisen parameters, and sample orientation," *Physical Review B,* vol. 79, May 2009.

[203] I. Calizo, W. Z. Bao, F. Miao, C. N. Lau and A. A. Balandin, "The effect of substrates on the Raman spectrum of graphene: Graphene-on-sapphire and graphene-on-glass," *Applied Physics Letters,* vol. 91, Nov 12 2007.

[204] C. Faugeras, A. Nerriere, M. Potemski, A. Mahmood, E. Dujardin, C. Berger, and W. A. de Heer, "Few-layer graphene on SiC, pyrolitic graphite, and graphene: A Raman scattering study," *Applied Physics Letters,* vol. 92, Jan 7 2008.

[205] H. Park, J. A. Rowehl, K. K. Kim, V. Bulovic and J. Kong, "Doped graphene electrodes for organic solar cells," *Nanotechnology,* vol. 21, Dec 17 2010.

[206] S. Gunes, H. Neugebauer and N. S. Sariciftci, "Conjugated polymer-based organic solar cells," *Chemical Reviews,* vol. 107, pp. 1324-1338, Apr 2007.

[207] C. Oshima and A. Nagashima, "Ultra-thin epitaxial films of graphite and hexagonal boron nitride on solid surfaces," *Journal of Physics-Condensed Matter,* vol. 9, pp. 1-20, Jan 6 1997.

[208] N. Srivastava and K. Banerjee, "Performance analysis of carbon nanotube interconnects for VLSI applications," presented at the Proceedings of the 2005 IEEE/ACM International conference on Computer-aided design, San Jose, CA, 2005.

[209] Y.-S. Min, E. J. Bae, B. S. Oh, D. Kang and W. Park, "Low-Temperature Growth of Single-Walled Carbon Nanotubes by Water Plasma Chemical Vapor Deposition," *Journal of the American Chemical Society,* vol. 127, pp. 12498-12499, 2005.

[210] F. Cicoira, N. Coppede, S. Iannotta and R. Martel, "Ambipolar copper phthalocyanine transistors with carbon nanotube array electrodes," *Applied Physics Letters,* vol. 98, pp. 183303-3, 2011.